Department of Petroleum Engineering

Microstructure and Nanoscale Rock Mechanical Properties of Coal: Applications to CO₂ Storage

Yihuai Zhang

This thesis is presented for the Degree of
Doctor of Philosophy
of
Curtin University

September 2017

DECLARATION

To the best of my knowledge and belief this thesis contains no material previously published by any other person except where due acknowledgment has been made. This thesis contains no material which has been accepted for the award of any other degree or diploma in any university.

Signature: 張彎懷 **(Yihuai Zhang)**

Date: 2017.08.31

ACKNOWLEDGMENT

ABSTRACT

CO_2 storage in deep unmineable coal seams and CO_2 enhanced coalbed methane (ECBM) recovery has received considerable interest in recent years. Therefore, improved understanding of the coal microstructure and the related mechanical and petrophysical properties has a wide range of benefits for field and environmental applications. However, due to the complex microstructure, the multi-porosity system, multi-scale heterogeneity, and coal matrix swelling effects, it remains a challenge to fully describe the coal microstructure, especially during water and CO_2 adsorption. Thus in this thesis, the coal microstructure was investigated to better understand the related nanoscale rock-mechanical properties, and morphological changes for different effective stresses and during water and CO_2 adsorption, including related porosity and permeability changes. Using in-situ reservoir condition X-ray micro-computed tomography imaging, it was observed for the first time how the micro cleat structure inside the coal matrix closed induced by supercritical CO_2 flooding in-situ, and associated fracturing of the mineral phase (embedded in the coal). This fracturing was induced by the internal swelling stress for which a new computational method was also proposed to predict and quantify the swelling stress in the coal matrix and the consequent fracturing of the mineral phase, including a quantification of the in-situ von Mises stresses generated by swelling. This study concluded that the coal microstructure affected the nanoscale rock mechanical properties, and such heterogeneous microstructure system could change during CO_2 flooding due to swelling effect.

PUBLICATIONS

Journal papers:

Papers related to this thesis:

Zhang, Y., Zhang, Z., Lebedev, M., Sarmadivaleh, M., Barifcani, A., Yu, H. and Iglauer, S., 2017. Micro-scale fracturing mechanisms in coal induced by adsorption of supercritical CO_2. *International Journal of Coal Geology*, 175, pp.40-50.

Zhang, Y., Lebedev, M., Sarmadivaleh, M., Barifcani, A. and Iglauer, S., 2016. Swelling-induced changes in coal microstructure due to supercritical CO_2 injection. *Geophysical Research Letters*, *43*(17), pp.9077-9083.

Zhang, Y., Xu, X., Lebedev, M., Sarmadivaleh, M., Barifcani, A. and Iglauer, S., 2016. Multi-scale x-ray computed tomography analysis of coal microstructure and permeability changes as a function of effective stress. *International Journal of Coal Geology*, *165*, pp.149-156.

Zhang, Y., Lebedev, M., Sarmadivaleh, M., Barifcani, A., Rahman, T. and Iglauer, S., 2016. Swelling effect on coal micro structure and associated permeability reduction. *Fuel*, *182*, pp.568-576.

Other journal papers:

Lebedev, M., **Zhang, Y.**, Sarmadivaleh, M., Barifcani, A., Al-Khdheeawi, E. and Iglauer, S., 2017. Carbon geosequestration in limestone: Pore-scale dissolution

and geomechanical weakening. *International Journal of Greenhouse Gas Control*, *66*, pp.106-119.

Lebedev, M., **Zhang, Y.**, Mikhaltsevitch, V., Iglauer, S. and Rahman, T., 2017 Residual trapping of supercritical CO_2: direct pore-scale observation using a low cost pressure cell for micro computer tomography. *Energy Procedia, 114*, pp.4967-4974.

Al-Yaseri, A.Z., Roshan, H., **Zhang, Y.**, Rahman, T., Lebedev, M., Barifcani, A. and Iglauer, S., 2017. Effect of Temperature on CO_2/Brine/Dolomite Wettability: Hydrophilic vs Hydrophobic Surfaces. *Energy & Fuels*, *31*(6), pp.6329-6333.

Roshan, H., Masoumi H., **Zhang, Y**., Al-Yaseri, A., Sarmadivaleh, M., Iglauer, S. and Lebedev, M., 2017. Micro-structural Effects on Mechanical Properties of Shaly-sandstone. *Journal of Geotechnical and Geoenvironmental Engineering* (in press).

Rahman, T., Lebedev, M., **Zhang, Y.**, Barifcani, A. and Iglauer, S., 2017 Influence of rock microstructure on its electrical properties: an analysis using x-ray microcomputed tomography. *Energy Procedia, 114*, pp.5023-5031.

Yu H., Rezaee R., Wang Z., Han T., **Zhang, Y**., Arif M. and Johnson L., 2017. A new method for TOC estimation in tight shale gas reservoirs. *International Journal of Coal Geology*, 179, pp.269-277.

Al-Khdheeai, E., Vialle, S., Barifcani, A., Sarmadivaleh, M., **Zhang, Y.** and Iglauer, S., 2017. Impact of salinity on CO_2 containment security in highly heterogeneous reservoirs. *Greenhouse Gases: Science and Technology* (in press)

Li, C., Dong, L., Xu, X., Hu, P., Tian, J., **Zhang, Y.** and Yang, L., 2017. Theoretical and experimental evaluation of effective stress induced sorption capacity change and its influence on coal permeability. *Journal of Geophysics and Engineering*, 14(3), p.654.

Conference papers:

Zhang, Y., Lebedev, M., Sarmadivaleh, M., Barifcani, and Iglauer, S., 2016, October. Change in Geomechanical Properties of Limestone Due to Supercritical CO_2 Injection. In *SPE Asia Pacific Oil & Gas Conference and Exhibition*. Society of Petroleum Engineers.

Zhang, Y., Zhang, Z., Sarmadivaleh, M., Lebedev, M., Barifcani, and Iglauer, S., 2017. Prediction of microscale rock mechanical performance from microCT images: heterogeneous coal as an example. In *51st US Rock Mechanics/Geomechanics Symposium*. American Rock Mechanics Association.

Zhang, Y., Sarmadivaleh, M., Lebedev, M., Barifcani, A., Rezaee, R., Testamantia, N. and Iglauer, S., 2016, March. Geo-Mechanical Weakening of Limestone Due to Supercritical CO_2 Injection. In *Offshore Technology Conference Asia*. Offshore Technology Conference.

Xu, X., Saeedi, A., **Zhang, Y.** and Liu, K., 2016, March. Laboratory Investigation on CO_2 Foam Flooding for Mature Fields in Western Australia. In *Offshore Technology Conference Asia*. Offshore Technology Conference.

Yu, H., Wang, Z., Rezaee, R., **Zhang, Y.**, Xiao, L., Luo, X., Wang, X. and Zhang, L., 2016, November. The Gaussian Process Regression for TOC Estimation Using Wireline Logs in Shale Gas Reservoirs. In *International Petroleum Technology Conference*. International Petroleum Technology Conference.

Yu, H., Wang, Z., Rezaee, R., Liu, X., **Zhang, Y.** and Imokhe, O., 2017, November. Fluid Type Identification in Carbonate Reservoir Using Advanced Statistical Analysis. In *SPE Oil and Gas India Conference and Exhibition*. Society of Petroleum Engineers.

Yu, H., Wang, Z., Rezaee, R., Su, Y., Tan, W., Yuan, Y., **Zhang, Y.**, Xiao, L. and Liu, X., 2017. Applications of Nuclear Magnetic Resonance (NMR) Logs in Shale Gas Reservoirs for Pore Size Distribution Evaluation. In *Unconventional Resources Technology Conference*. URTEC.

Presentations:

Zhang, Y., Lebedev, M., Zhang, Z., Sarmadivaleh, M., Barifcani, A.and Iglauer, S., 2017, April. Coal cleat closure during supercritical CO2 injection and associated permeability drop: from microscale observation to DEM predictions. In *253rd ACS National Meeting & Exposition*. ACS.

Zhang, Y., Sarmadivaleh, M., Barifcani, A., Lebedev, M. and Iglauer, S., 2016, May. Coal microstructure changes due to water absorption and CO_2 injection. In *APPEA Oil and Gas Conference & Exhibition 2016*. APPEA.

Zhang, Y., Sarmadivaleh, M., Barifcani, A., Lebedev, M. and Iglauer, S., 2016, June. Investigation the supercritical CO_2 injected in carbonated rocks with X-ray tomography analysis. In *Australian Earth Sciences Convention 2016*.

TABLE OF CONTENTS

LIST OF FIGURES

LIST OF TABLES

Chapter 1   Introduction and Literature review

1.1   Background

CO_2, as the major greenhouse gas in the atmosphere, is tightly correlated with global temperature (Jouzel et al., 2007; Lüthi et al., 2008). The rising global population and activities related to this rise, such as fossil fuels combustion, have caused the level of atmospheric carbon dioxide to climb at an alarming rate (Metz et al., 2005). Fossil fuels currently occupy around 80% of the world's energy consumption. The International Energy Agency predicts that energy use will continue to increase by more than 30% until 2035, where around 75% of energy consumption will still be fossil fuels regardless that renewable energy (e.g. solar, geothermal, and wind) is becoming increasingly popular. Such a situation will result in the challenge of dealing with greenhouse gas emissions (Finley 2013).

Carbon Capture and Storage (CCS) is thought to be the most effective solution for maintaining acceptable CO_2 levels in the atmosphere (Metz et al. 2005, Bachu et al. 2007, Bradshaw et al. 2007). The CO_2 can be captured from a power plant or directly from the atmosphere and then stored underground in different trapping sites, such as deep saline aquifers, abandoned oil/gas reservoirs, and coal seams. For safety (avoiding leakage), the CO_2 must always be injected into an area more than 800m deep where the temperature and pressure are higher than the CO_2's critical point (temperature 304.25K / 31.10^o / 87.98 ^{o}F; pressure 72.9 atm / 7.39 MPa / 1071 psi, Vargaftik 1975). The injected CO_2 thus undergoes a supercritical phase in the reservoir (Metz et al, 2005) (see Figure 1-1 for the CO_2 phase graph). The CO_2's vertical migration, owing to the buoyancy effect, has been thought as the significant

hazard (Li and Liu, 2016) that may potentially lead to fresh water contamination, human/animal health risks, and ecosystem collapse (Dai et al., 2014). Thus, the different trapping mechanisms need to be fully understood and applied.
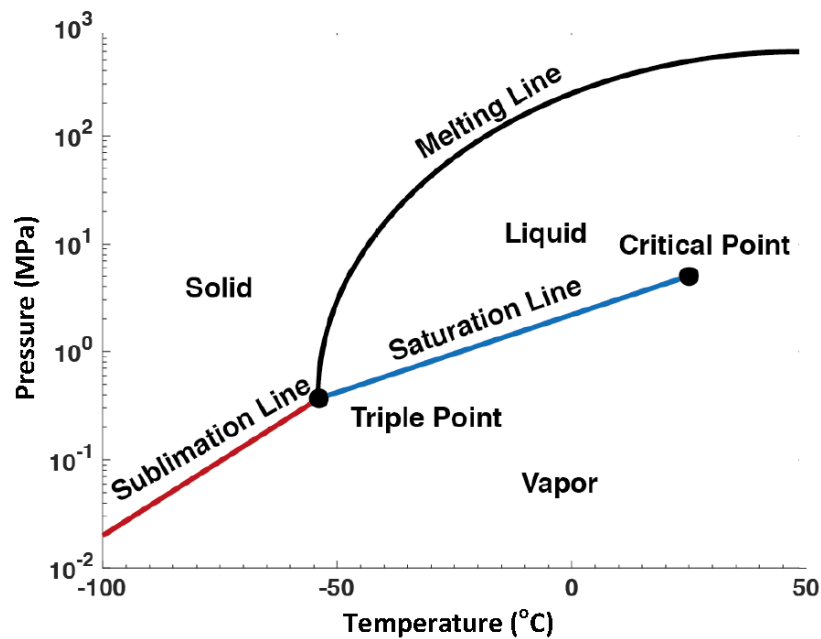
Figure 1-1 The CO_2 phase behavior map; dada from (Carroll et al., 1991)

The premier trapping mechanism is structural trapping where the CO_2 is directly stored inside the high porosity and permeability target zones with sealed caprock (Naylor et al. 2011, Pini et al. 2012; Iglauer et al.2015, Krevor et al. 2015). The second trapping mechanism is residual trapping because of the hysteresis of capillary pressure (Pentland et al. 2011,Iglauer 2017, Al-Yaseri. 2017a,b). The third trapping mechanism is solubility trapping, where the carbon dioxide is dissolved in the formation water; this is thought to be the most common trapping method in the deep brine saline aquifers (Gilfillan et al., 2009; Iglauer 2011). The fourth trapping mechanism is mineral trapping: the CO_2 is transferred to the carbonate mineral,

which may take a long time (over thousands of years) (Xu et al., 2003; Metz et al., 2005; Matter and Kelemen, 2009). These trapping mechanisms have been fully investigated and described in former studies and the storage time of such trapping mechanisms are shown in Figure 1-2. The CO_2 injected into the deep coal seam has a unique trapping mechanism known as adsorption trapping (Golding et al., 2011). However, this mechanism is still poorly understood and needs investigating.
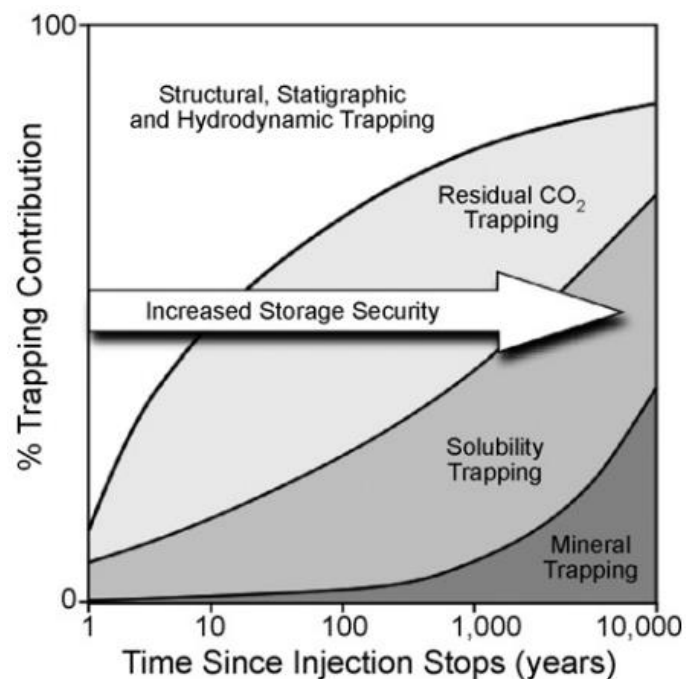
Figure 1-2 The four main trapping mechanisms with the storage time (Metz et al., 2005).

The carbon geosequestration into the coal seam is the "win-win" selection, not only for the CO_2 storage but also for the enhanced production of coal bed methane (ECBM) by stimulation or fracking, as the coal has adsorption preference for carbon dioxide relative to methane (White et al., 2005). The significant advantage for

adsorption trapping is the CO_2 is stored in the coal majorly as adsorbed molecules on the surface of the microstructure with more capacity, higher density, and shallower storage depth compared to normal sandstone and carbonate reservoirs. The former literature data estimated that the CO_2 storage capacity for worldwide coal seams could reach 964 Gt (Golding et al. 2011); comparing the global carbon emissions from fossil fuel use were 30 Gt in 2009 (Friedlingstein et al. 2010), such storage capacity can maintain 30 years human activity. However, the injection rate and coal seam permeability could be uncontrolled the swelling effect is reported by CO_2 adsorption (Mazumder and Wolf, 2008, Gu et al. 2017) and how such swelling effect affects the coal microstructure with reduced permeability needs to be fully understood. Further, coal is a heterogeneous material that has multiscale pore systems with complex microstructures, and need to be fully characterized as the fundamentals for the coal CO_2 geosequestration (Mathews et al. 2017, Mostaghimi et al. 2017, Zhao et al. 2016, Zhou et al. 2017). The microstructures with different properties can largely affect the physical, chemical, and mechanical properties of the coal in the bulk and field volume scale. Thus, the detailed characteristics of complex microstructures, such as the pore structures, pore connectivity, mineral types, and spatial distribution appear to be crucial, which could help in understanding the permeability, sorption capacity, gas migration, wettability and CBM/ECBM/CO_2 storage. Furthermore, the coal's heterogeneous morphology resulting in the mechanical properties are also heterogeneous on the micro/nanoscale. Such small-scale rock mechanical properties are extremely important for multiscale fractures mechanism and further precise modeling, where the mechanical performance can be predicted based on the material's structures and composition (Bobko et al. 2011,

Constantinides et al. 2006, Fischer-Cripps 2006, Lebedev et al. 2014, Vialle and Lebedev 2015).

Thus, in this thesis, the coal microstructure is investigated to better understand the related nanoscale rock-mechanical properties and morphological changes in different effective stresses and during water and CO_2 adsorption, including related porosity and permeability changes.

1.2   Enhanced coal bed methane and CO_2 storage in coal seam

1.2.1   The origins of coal bed methane

Two primary origins had been suggested that for coal bed methane—biogenic and thermogenic—where most of them are thermogenically derived and few are purely biogenic (see Figure 1-3, from Moore 2012). The biogenetic methane mainly comes from the bacteria and archaea; see Figure 1-4. It is believed that bacteria begin the process by fermentation and anaerobic oxidation. The acetate and ketones (that are fermented to H-CO_2 compounds) as the consequence of polyaromatics and carboxylic. Further, combine with the different methods such as aliphatic to carbon dioxide and anaerobically oxidize the aromatic. Finally, the methane is composed by acetoclastic or CO_2-reduction methanogenesis (Green et al., 2008).
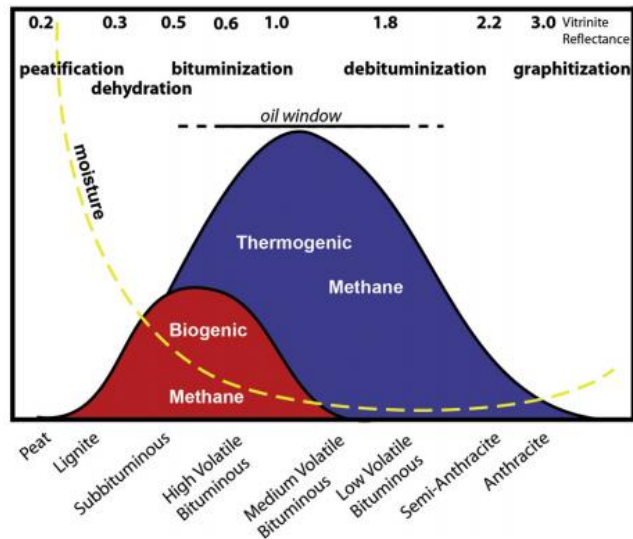
Figure 1-3 The biogenic and thermogenic gas generation in relation to rank, moisture, vitrinite reflectance and coalification stages (Moore 2012).
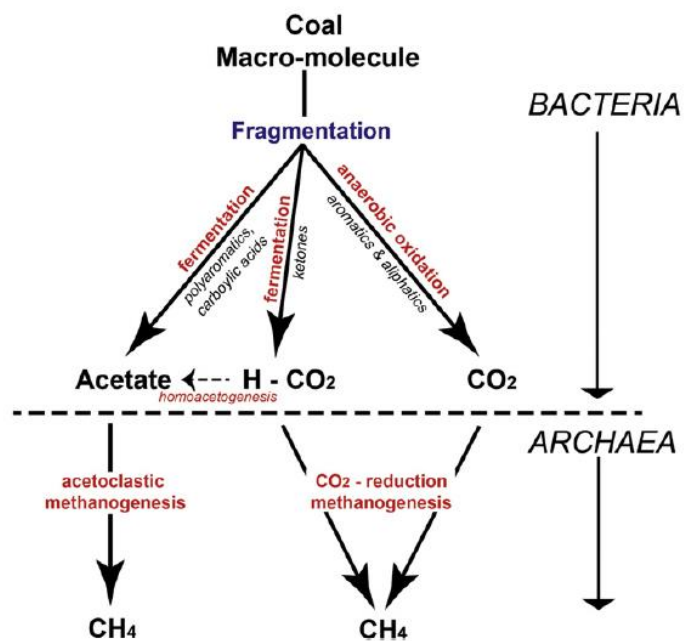
Figure 1-4 The pathway of secondary biogenic methane production in coal (Strąpoć et al., 2008)

The thermogenic origin is from a lengthy combination process consisting of high temperature and pressure. Such thermogenic gas generation varied for the different rank of coals, which is highly correlated to organic matter and basin sedimentary history (Whiticar et al., 1986). Zhang et al., (2008) claimed that the produced CH_4 increased drastically as the vitrinite reflectance increased. Thus, it is believed that the high-rank coals store more methane, as the low-rank coal lacks moisture and the thermogenic process produces more gas than the biogenic processes (Moore 2012).

1.2.2   ECBM reservoir screening criteria

The coal seam selection process is extremely important for ECBM and CO_2 geosequestration. Moore (2012) suggested some screening criteria for proper reservoirs:

1) The coal reservoir should be vertically isolated with other coal seam layers and laterally continuous. This could help to achieve a better sweep efficiency when the carbon dioxide goes through.

2) Simple coal seam structures help to make drilling and well maintenance easier. Further, the sealing seam layer without open joints and faults is preferred.

3) The coal permeability is important for the sweep efficiency and production rate. It suggests the moderate cleat permeability of approximately 1-5 mD is required.

4) The optimal coal seam depth: the shallow coal related to low reservoir pressure and temperature with less coal bed methane and CO_2 stored capacity; however, the deep coals seams may meet the low permeability problems.

5) Coal geometry: a thin coal seam is better than a thick deposit.

6) Gas saturation: gas and water saturation of the coal seam need to be fully understood before the ECBM / CCS project.

1.2.3 Fluid transport in the coal seam

Coal is different from other normal reservoir rocks (e.g. sandstone and carbonate rock). The matrix itself is made of tight materials. Hence, all the gases and water moving inside the coal seams need to do so via cleats/fractures in the system (Dryden, 1963, Jing et al. 2017). The cleat system formed during coalification and can be separated into face cleats and butt cleats, see Figure 1-5 for details. Face cleats have a more prominent morphology and are laterally extensive and continuous flow routes for gas and water. Butt cleats, however, are perpendicular to the face cleat, these cleats tend to be discontinuous and nonplanar cross joints and commonly end at the intersection with face cleats (Laubach et al., 1998). The permeability of different coal seams could range from 0.1-100 mD. The morphology and quantity of cleats, as well as the connectivity, are the main factors affecting gas transport and gas de-/adsorption.
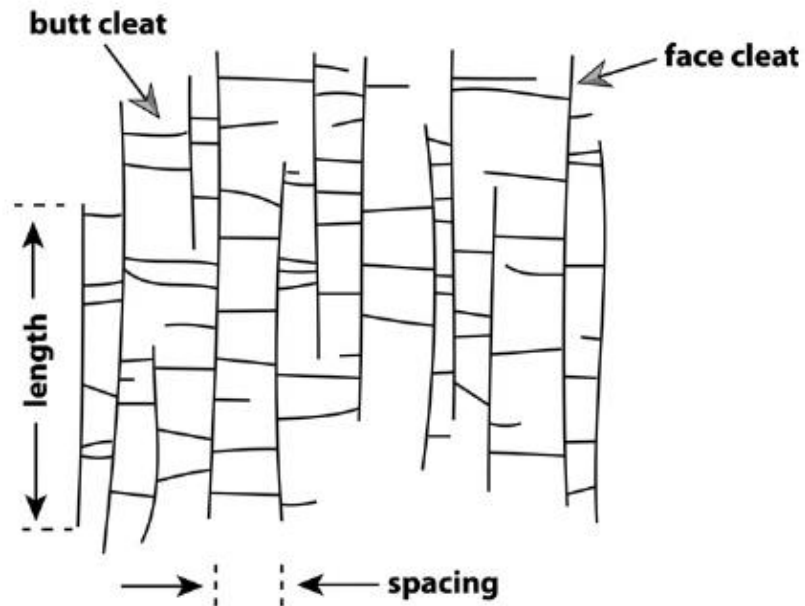
Figure 1-5 The schematic of face and butt cleats (Moore, 2012).

The permeability is extremely important in describing how easy the fluids pass through the coal seam. It is also vital to understand another type of coal permeability: the coal matrix. The matrix permeability is the coal matrix's permeability, without the natural fractures (e.g. the cleats). The original pore system (always at micro/nano scale) in the coal matrix determines matrix permeability; such matrix permeability is usually estimated from the laboratory core sample (less and no fractures) with orders of magnitudes lower than fracture permeability for the same coal seam. The matrix permeability is also higher in lower rank coals, where less maturity of the coal matrix always has more inside pore system (Laubach et al., 1998).

1.2.4   The coal structure changes in ECBM/CCS

The coal structure changes in ECBM/CCS may largely influence the coal permeability, production rate, and rock mechanical properties. Here, the coal structure, the former studies mainly focus on the cleats/fractures, which, as has been suggested, could be affected by pressure and gas swelling or desorption.

Water adsorption has been suggested to decrease the sorption capacity of $CO_2/CH_4/N_2$ in CBM/ECBM and storage volume for CO_2 geosequestration (Krooss et al. 2002; Ozdemir and Schroeder 2009). Further, water encroachment and associated water adsorption are natural during CBM/ECBM and CO_2 storage in coal seams (Stevens et al. 1998). The coal matrix undergoes adsorbed water stage and swelling and the cleats system close up. This, in turn, results in a lower permeability for the coal seam and reduces the gas production rate.

Carbon dioxide could also result in a large swelling effect of the matrix, as it has a higher adsorption value than CH_4. In general, the lower the rank of coal has more degrees affected by swelling because of CO_2 injection, compared with the higher rank equivalents (owing to its abundant cleats system). Karacan et al., (2003) claimed that the coals dominated by vitrinite and liptinite swelled more than inertinite and clay-rich coals.

To understand the swelling-fracture–permeability relationship,   several coal swelling permeability models have been built. The swelling characteristics are typically simulated by coal matrix strain change (e.g. Day et al. 2008; Vandamme et al. 2010) but these models have failed to explain the stress-controlled swelling laboratory test results (Liu et al. 2011). Therefore, a new strain model (Peng et al. 2014) has been tuned to match the laboratory results. These updated strain models, however, still

have significant limitations regarding predictions (Larsen 2004; Saikat Mazumder et al. 2006; Pan and Connell 2007).

Shrinkage occurs when the gas is desorbed from the coal matrix and is fundamentally related to the mechanical elastic properties of the coal. When the methane is desorbed, the micro pores inside the coal matrix, which stored the gas, shrink and return to their original size (George and Barakat, 2001). This effect on millions of micro pores has an enormous consequence on the particular area of the coal matrix, resulting in the cleat width increasing. One presented that the loss of moisture in a reservoir could result in matrix shrinkage (Ozdemir and Schroeder, 2009). Such coal matrix shrinkage largely depends on the coal's rank and organic composition (Wang and Ward, 2009) and such shrinkage can counteract any decrease in the permeability from the swelling effect.

Furthermore, such a coal cleats system is very sensitive to the pressure change. During methane production, the decreasing pore pressure could result in increased stress and such effective stress change may have a significant impact on the cleats' morphology. It has been thought that the cleats change when the in-situ stresses change (Chen et al., 2011). However, varying the microstructural morphology associated with such changes, especially in micro cleats (less than 20 µm), which is common in the coal matrix (Gamson et al., 1993), is poorly understood. Thus, the changes in cleats/fractures vary and are controlled by a combination of swelling, shrinkage, and effective stress. Some researchers did some pilot studies in this area, such as Rangathunga, et al., (2017) who conducted an experiment to determine the effects of volumetric strain on the brown coal sample for CO_2 adsorption and CH_4 production; see Figure 1-6 for the results of gas production variation with volumetric strain for natural production and different CO_2 injected pressure.
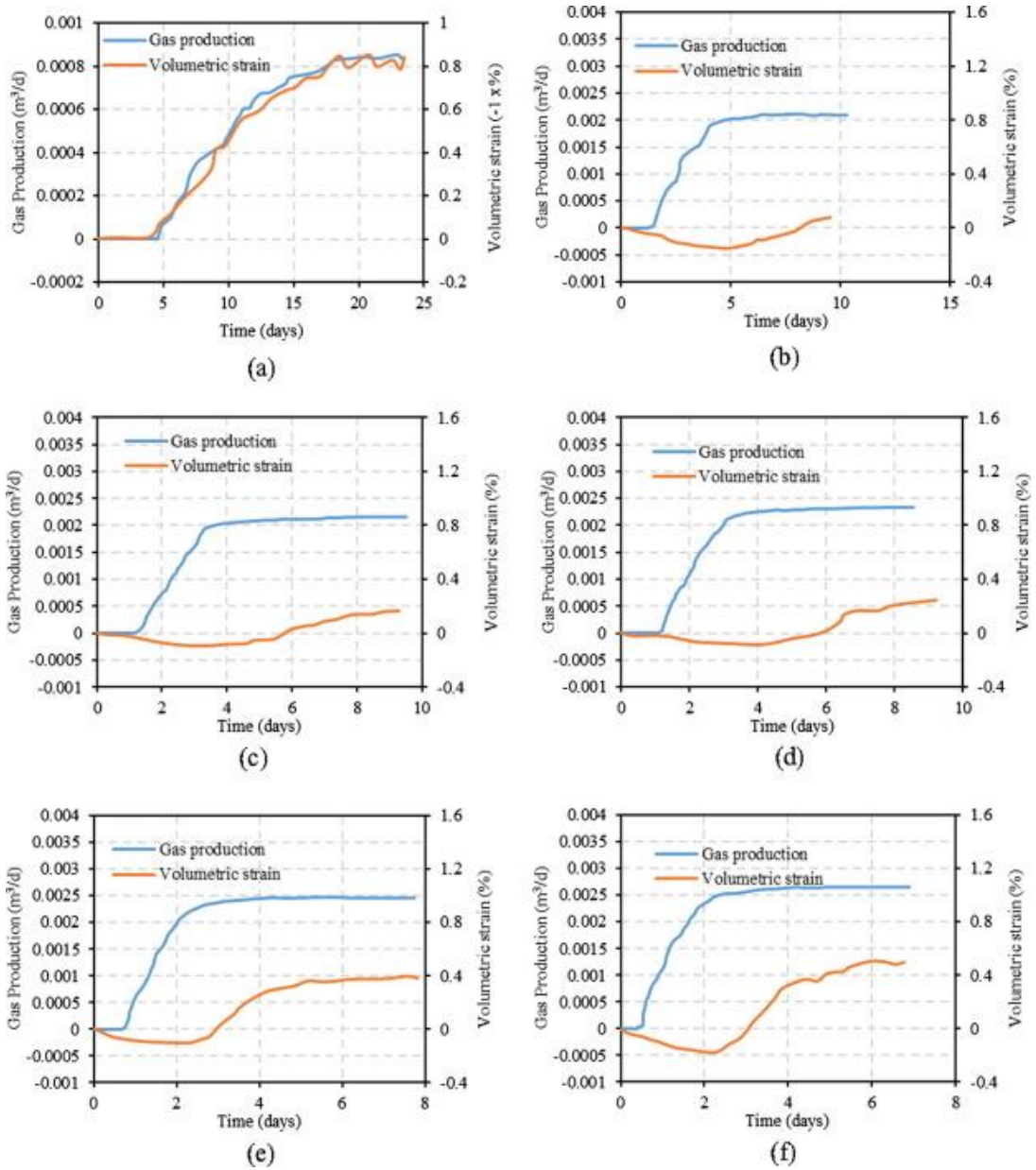
Figure 1-6 The gas production variation with volumetric strain for (a) natural production, (b) 5 MPa, (c) 6 MPa, (d) 7 MPa, (e) 8 MPa and (f) 9 MPa CO_2 floods (Rangathunga, et al., 2017).

1.3 Pore scale imaging

Coal microstructures has been investigated by different techniques: mercury injection capillary pressure (MICP) can obtain the pore throat size (Liu et al. 2016); nuclear magnetic resonance (NMR) is a non-destructive method that can identify the pore size distribution (Sun et al. 2016; Yao et al. 2014; Li et al. 2016); and scanning electron microscopy (SEM) can present the coal's microstructure with 2D nanoscale resolution (Predeanu et al. 2016).

The 3D microscale computed tomography (microCT) technique allow us to image the coal structures in 3D with high resolutions (Yu et al. 2012, Mathews et al. 2017, Lebedev et al. 2017a, 2017b, Shi et al. 2018), where the voxel size could be as high as $1 - 3$ µm. This method is much more precise than the 2D (SEM) method, as, for example, the quantified percolation threshold is much lower in the 3D method compared to the 2D method. The basic elements for microCT include an X-ray source, detector, and sample stage, where the sample stage is located between the x-ray source and detector while all the parts can move to alter the distance to adjust the magnification during scanning. The output data is displayed as a greyscale image; referring to voxel size and representing the effective x-ray attenuation coefficient (X-ray density) of the different materials of the scanning sample. See Figure 1-7 for the microCT image of an example of oil-sandstone after water flooding (Iglauer et al., 2012). Through the newly high-pressure high-temperature (HPHT) flooding cell (see Figure 1-8, Iglauer et al., 2011), the sample can now also be imaged at high resolution in reservoir condition.
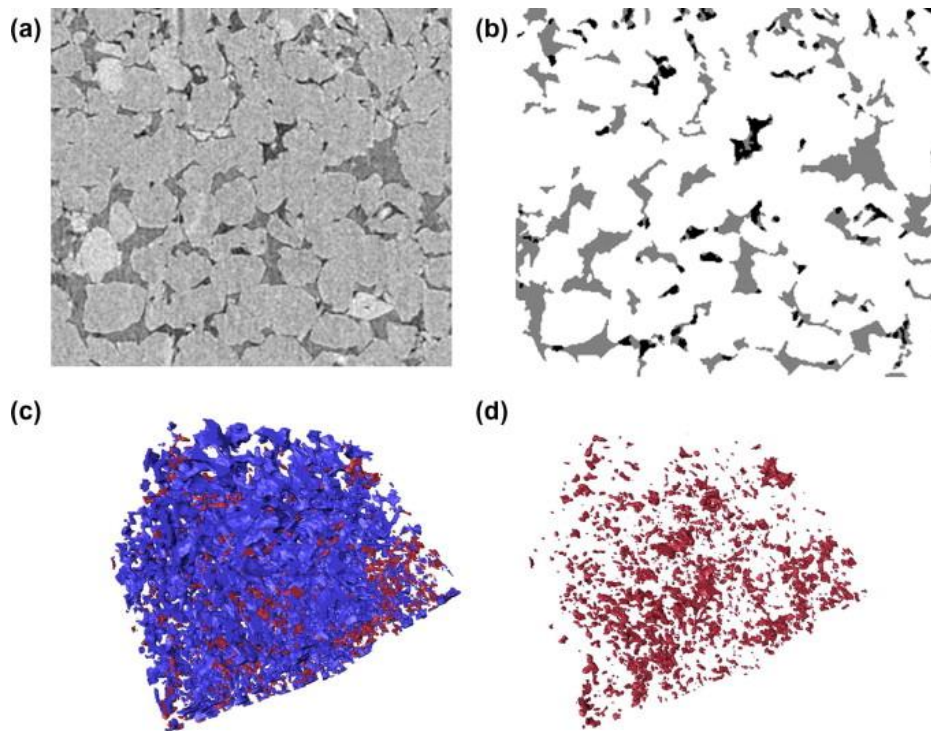
Figure 1-7 MicroCT images showing the oil-wet core after water flooding (nominal voxel size was $(9 \ \mu m)^3$): (a) two-dimensional slice through the core; oil is black, brine dark grey, and rock light grey; (b) the same image segmented; oil is black, brine dark grey and rock is white; (c) residual oil clusters (red) and surrounding brine (blue) in three dimensions; and (d) residual oil clusters (red) in three dimensions (Iglauer et al., 2012).

By such microCT tomography, the coal microstructures can be separated into different phases based on the x-ray density and then quantified followed by a reconstruction process. Some studies have been done on coal using this powerful tool. For example, Yao et al. (2009) measured the distributions of the coal matrix constituents, Mathews et al. (2011) analyzed the extent of thermal drying-induced deformations in coal, and Ramandi et al. (2016) mapped the 3D distribution of minerals in coal from the Bowen Basin, Australia and compared the results with

XRD, SEM, and QEMSCAN data. However, there is still lack of research using the in-situ microCT flooding technique to observe coal microstructure.
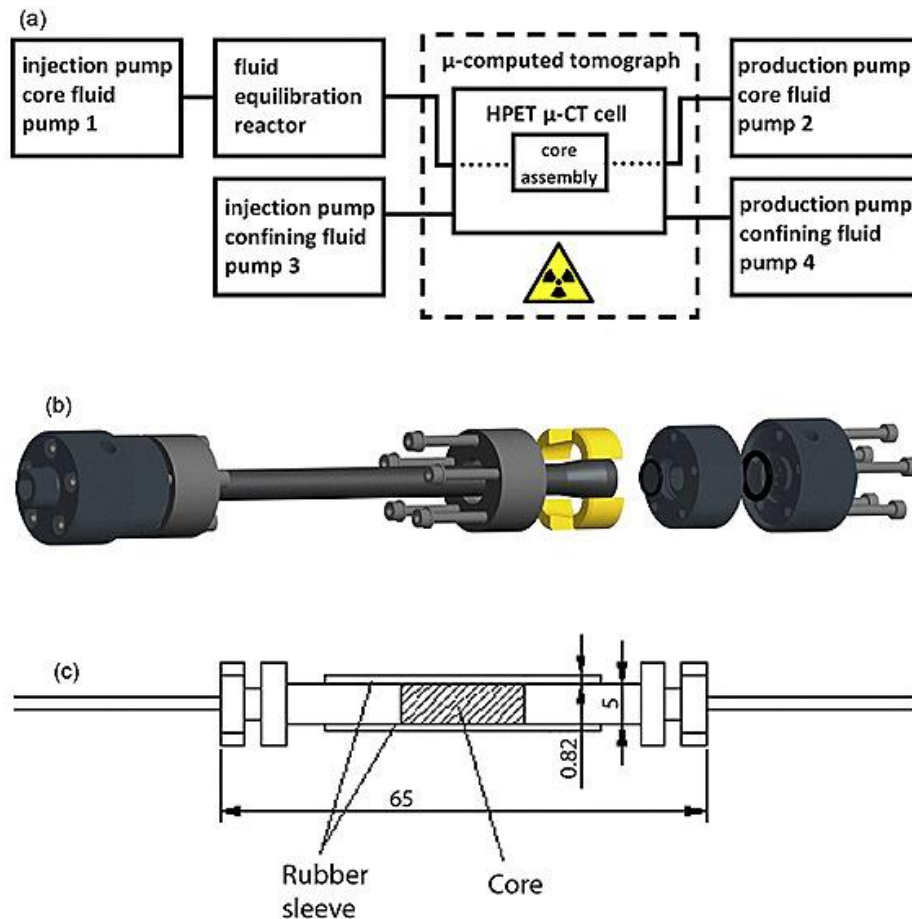
Figure 1-8 Sketch of the HPHT microCT core flooding system: (a) process scheme; (b) assembly plot of the high pressure elevated temperature (HPET) μ-CT cell; (c) core assembly (the thin aluminum foil is not shown), dimensions in millimeters (Iglauer et al., 2011).

1.4 Nanoindentation test

The coal's heterogeneous morphology results in the mechanical properties being also heterogeneous on the micro/nano scale. Such small-scale rock mechanical properties

are extremely important for multiscale fracture mechanisms and further precise modeling, where the mechanical performance can be predicted based on the material's structures and composition (Bobko et al. 2011, Constantinides et al. 2006, Fischer-Cripps 2006, Lebedev et al. 2014, Vialle and Lebedev 2015). Such small scale mechanical properties nowadays can be obtained by the newly nanoindentation experiment, which has been successfully applied to natural rocks such as sandstone (Zhu et al. 2009), limestone (Lebedev et al. 2014), coal (Manjunath and Nair 2015, Yu et al. 2017) and shale (Kumar et al. 2012, Li and Sakhaee-Pour 2016, Liu and Ostadhassan 2017, Zeszotarski et al. 2004). However, there is still lack of data about how such small-scale mechanical properties correlate with the coal's rank and the related anisotropy.

Experimentally, the penetration depth (h) of an indenter as a function of a loading and unloading force (P) is measured (see 1-9 for indentation technique, Lebedev et al. 2014). The indenter has a known geometry and mechanical properties and the indentation modulus (M, also called "reduced modulus") obtained from the acquired *P-h* curves, equation (1) (Fischer-Cripps 2004):

$$M = \frac{1}{2} \frac{\sqrt{\pi}}{\sqrt{A}} \frac{dP}{dh} \qquad\qquad 1\text{-}1$$

where A is the contact area and *dP/dh* is the unloading indentation stiffness, measured at maximum applied force P_{max} and maximum penetration depth h_{max}. For an isotropic material, Young's modulus E and Poisson's ratio v can then be related to M as:

$$M = \frac{E}{1-v^2} \qquad\qquad 1\text{-}2$$
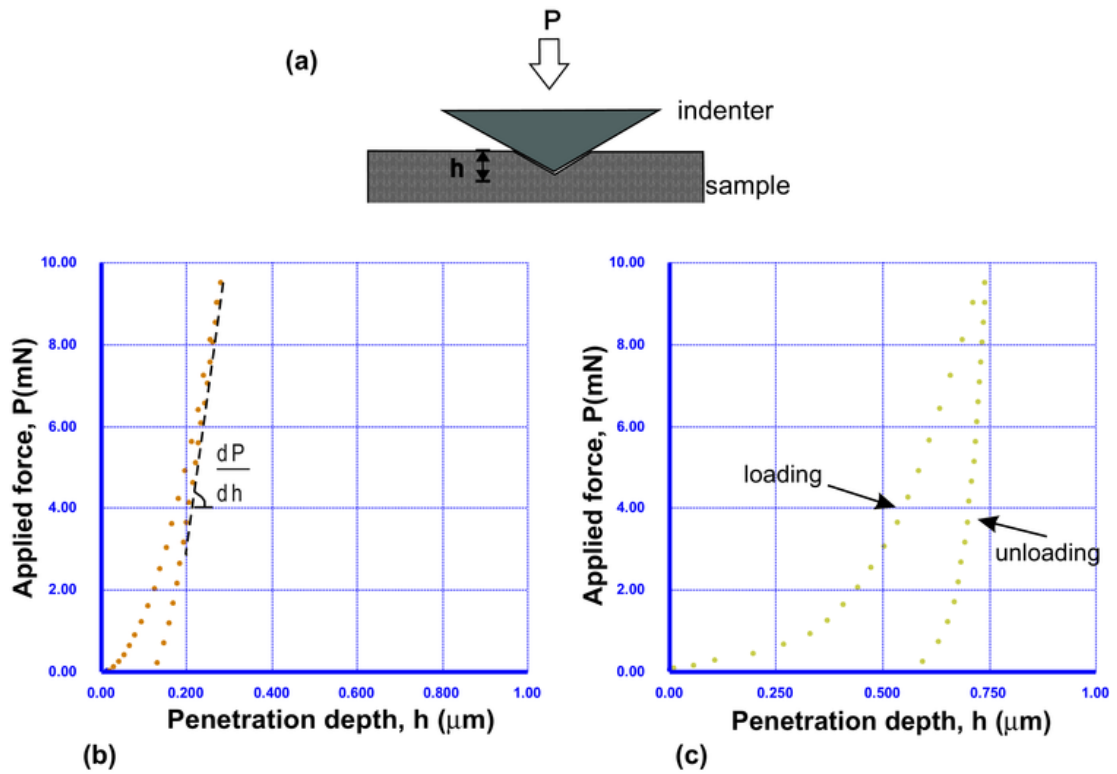
Figure 1-9 The indentation technique: (a) Penetration of indenter into the sample during loading. Typical load-unloading curves for two samples; (b) fused silica (Young's modulus 72.5 GPa, Poisson's ratio 0.17, measured indentation modulus 74.6 GPa); and (c) the Savonnières limestone sample (indentation modulus at this point is 65.4 Gpa) (Lebedev et al. 2014).

1.5 Thesis outline

In this thesis, the coal microstructures are investigated to better understand the related nanoscale rock-mechanical properties, and how the microscale morphological changes in different subsurface conditions: the different effective stresses,during water injection and $scCO_2$ adsorption, and also including the related porosity and permeability changes. The HPHT in-situ microCT core flooding system is also used for investigating how the micro-cleat structure inside the coal matrix closed induced

by supercritical CO_2 flooding in reservoir condition. Note that, Chapter 2 is the foundational chapter that characterizes all range of coal types (other body chapters mainly focus on the medium rank coal), laying a good foundation for later chapters and future work. This thesis consists of 7 chapters (also see Figure 1-10 for the flow chart of this thesis):

Chapter 1 − Introduction and literature review, which give the background and literature review in the area of enhanced coal bed methane and CO2 storage in the coal seam, pore scale imaging, and nanoindentation tests.

Chapter 2 − Pore scale 3D microCT characterization and rock mechanical property of high to low-rank coal seams. In this chapter, the 3D morphology and rock mechanical property of high to low-rank coals (anthracite, bituminous, sub-bituminous, lignite, and peat) are investigated by 3D high-resolution microCT scanning (3.43 μm voxel size) and nanoindentation testing.

Chapter 3 − Coal microstructure change under different effective stress. The sub-bituminous coal samples are imaged at two resolutions (medium - 33.7 μm and high - 3.43 μm voxel size) in 3D with x-ray micro-computed tomography as a function of applied effective stress and it is investigated how cleat morphology k and ϕ are influenced by the changes in effective stress and how these parameters are interrelated.

Chapter 4 − MicroCT in-situ water injection into coal. The dry coal plugs and swollen coal plugs (swollen because of brine adsorption) are imaged at high resolution $(3.43 \text{ μm})^3$ in 3D with x-ray micro-computed tomography (microCT).

Chapter 5 – MicroCT in-situ supercritical CO_2 injection into coal. Before and after supercritical CO_2, the coal is imaged at high resolution $(3.43\ \mu m)^3$ in 3D by a novel HPHT microCT flooding system.

Chapter 6 – Micro-scale fracturing mechanisms in coal induced by adsorption of supercritical CO_2. A new method is proposed combining x-ray microtomography imaging, nanoindentation testing, and DEM modeling.

Chapter 7 – Conclusion chapter. The highlights of the findings of this thesis and suggestions for future study in this area are presented.
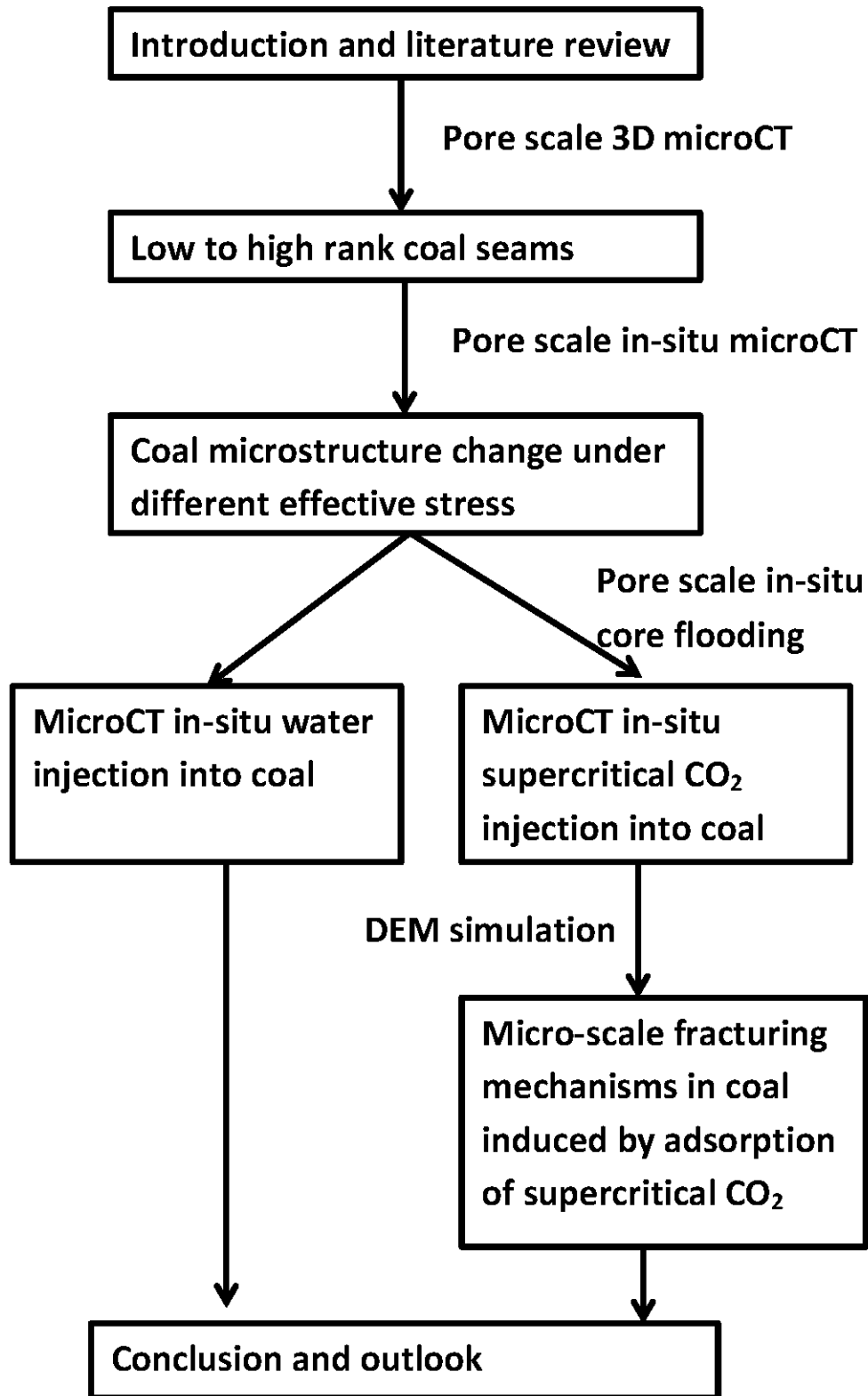
Figure 1-10 The flow chart of this thesis.

Chapter 2 Pore scale 3D microCT characterization and rock mechanical property of low to high rank coal seams

Abstract

The coal microstructure and the rock mechanical property are extremely important for the coal characterization and analysis in the coal seam explorations, coal bed methane (CBM), enhanced coal bed methane (ECBM), and CO_2 storage. However, how the coal rank related to the microstructure and rock mechanical property are still in-sufficient. Thus, in this study, the 3D high resolution microCT scanning (3.43 µm) and nanoindentation test on high to low rank coals – anthracite, bituminous, sub-bituminous, lignite, and peat were conducted. The coal microstructure is quantified after the image segmentation process which shows that the low rank coal has the most abundant pore system (including large pores and tiny pores) and high rank coal has the more mature fracture system. Furthermore, the coal indentation modules decrease from high to low rank coal, and such mechanical property is suggested be highly correlated with fixed carbon content.

2.1 Introduction

Coal is kind of heterogeneous materials which has multiscale pore systems with complex microstructures, and need to be fully characterization as the fundamentals for the coal seam explorations, coal bed methane (CBM), enhanced coal bed methane

(ECBM), and CO_2 geosequestration into deep unminable coal seams (Zhao et al. 2016) (Mathews et al. 2017, Mostaghimi et al. 2017, Zhou et al. 2017). The microstructures with different properties can largely affect the physical, chemical and mechanical properties of the coal in the bulk and field volume scale. Thus the detail characteristics of complex microstructures such as the pore structures, pore connectivity, mineral types, and spatial distribution appear to be crucial important which could help to understand the permeability, sorption capacity, gas migration, wettability and further for the CBM / ECBM / CO_2 storage.

The coal microstructures has been investigated by different techniques: the Mercury Injection Capillary Pressure (MICP) can obtain the pore throat size (Liu et al. 2016); the Nuclear Magnetic Resonance (NMR) is a no-destructive method which can identify the pore size distribution (Sun et al. 2016; Yao et al. 2014; Li et al. 2016); Scanning Electron Microscopy (SEM) can present the coal microstructure at nanoscale resolution at 2D (Predeanu et al. 2016); and the 3D Microscale Computed Tomography (microCT) technique developed in recent years allow us to image the coal structures in 3D at high resolutions (Zhang et al. 2016b; Mathews et al. 2017), where the resolution (voxel size) could as high as $1 - 3$ µm, such method is much more precise than 2D (SEM) where for example the quantified percolation threshold is much lower in 3D comparing with 2D. The basic elements for microCT are including X – ray source, detector, and sample stage, where the sample stage located between the X – ray source and detector while all the parts can move to alter the distance to adjust the magnification during the scanning. The output data is displayed as grey scale image; refer to voxel size and representing the effective X-ray attenuation coefficient (X – ray density) of the different materials of the scanning sample. By such microCT tomography, the coal microstructures can be separated

into different phases based on the X – ray density and then quantified followed by a reconstructed process. Some studies have been done on coal using this powerful tool, for example, Yao et al. (2009) measured the distributions of the coal matrix constituents; Mathews et al. (2011) (Mathews et al. 2011) analyzed the extent of thermal drying-induced deformations in coal; Ramandi et al. 2016 mapped the 3D distribution of minerals in coal from Bowen Basin, Australia and compared the results with XRD, SEM, and QEMSCAN data; and also the Chapter 4 and 5 in this thesis (Zhang et al. 2016e, d) However, most of the coal studies only focus on one kind of coal or in one specific coal rank, and there is lack of system studies present how the morphology correlated with coal's rank (from low to high).

Furthermore, the coal's heterogeneous morphology results the mechanical properties are also quite heterogeneous in micro/nano scale. Such small scale rock mechanical properties are extremely important for multiscale fractures mechanism and further precise modelling – where the mechanical performance can be predicted based on the material's structures and composition (Bobko et al. 2011, Constantinides et al. 2006, Fischer-Cripps 2006, Lebedev et al. 2014, Vialle and Lebedev 2015). Such small scale mechanical properties nowadays can be obtained by the newly nanoindentation experiment, which has been successfully applied on natural rocks such as sandstone (Zhu et al. 2009), limestone (Lebedev et al. 2014, Zhang et al. 2016a), coal (Manjunath and Nair 2015, Zhang et al. 2017) and shale (Kumar et al. 2012, Li and Sakhaee-Pour 2016, Liu and Ostadhassan 2017, Zeszotarski et al. 2004). However, there is still lack of data about how such small scale mechanical property correlating with the coal's rank and the related anisotropy.

In this chapter, we thus microCT imaged the different rank of coal (anthracite, bituminous, sub-bituminous, lignite, and peat) in high resolution (3.43 µm) and

followed with qualitative and quantitative analysis. We also conducted the nanoindentation test on these coal samples and discussed how the morphology based on coal ranks was correlated to rock mechanical property.

2.2   Methodology

2.2.1   Materials

The different coal rank samples were selected in this study: high rank (the anthracite from Hazelton, Pennsylvania, USA); medium rank (the bituminous from Morgantown, West Virginia, USA; the sub-bituminous, from Pingdingshan, Henan, China); and low rank (the lignite from North Dakota, USA). The petrophysical properties for the coal samples were tabled in Table 2-1. We also selected the peat from Glastonbury, England, which has been thought at the earliest stage (the lowest rank) during the formation of coal (Elliott 1981). The SEM images for these samples were presented in Figure 2-1, where the anthracite had the most "clean face" with few minerals (white colour); the bituminous had more and "cloudy" minerals; the sub-bituminous sample had large mineral vein in the coal matrix; the lignite had the significantly cleats/fractures, and the peat had the softest surface with many pore structures. The XRD test was also carried out for these coal samples by Bruker – AXS D9 Advance Diffract Meter and the crystallized minerals for each sample were tabulated in Table 2-2 (Not that the organically materials in the coal matrix cannot be detected in the XRD test). Then the small cylindrical coal plugs (5 mm diameter, and 10 mm length) were drilled parallel to the bedding plane and carefully prepared for the microCT scanning (see 2.2), and the cuboid coal samples ($l \times w \times h = 8$ mm $\times$

5 mm × 2 mm) were also cut and carefully polished for the nanoindentation tests (see

2.3).

Table 2-1 The petrophysical properties for coal samples studied.

Sample	Location	M (%)	V (%)	A (%)	C_f (%)	ρ (g/cm^3)
Anthracite .	Pennsylvania, USA	2.6	2.9	9.7	84.9	1.3
Bituminous	West Virginia, USA	2.0	32.4	6.4	59.2	1.3
Sub-bituminous	Henan, China	6.9	36.0	4.2	54.0	1.4
Lignite	North Dakota, USA	16.3	34.8	7.8	41.1	1.4

Note: M (%) is the moisture content; V (%) is the volatile matter; A (%) is the ash;

C_f (%) is the fixed carbon content, and ρ (g/cm^3) is the bulk density.
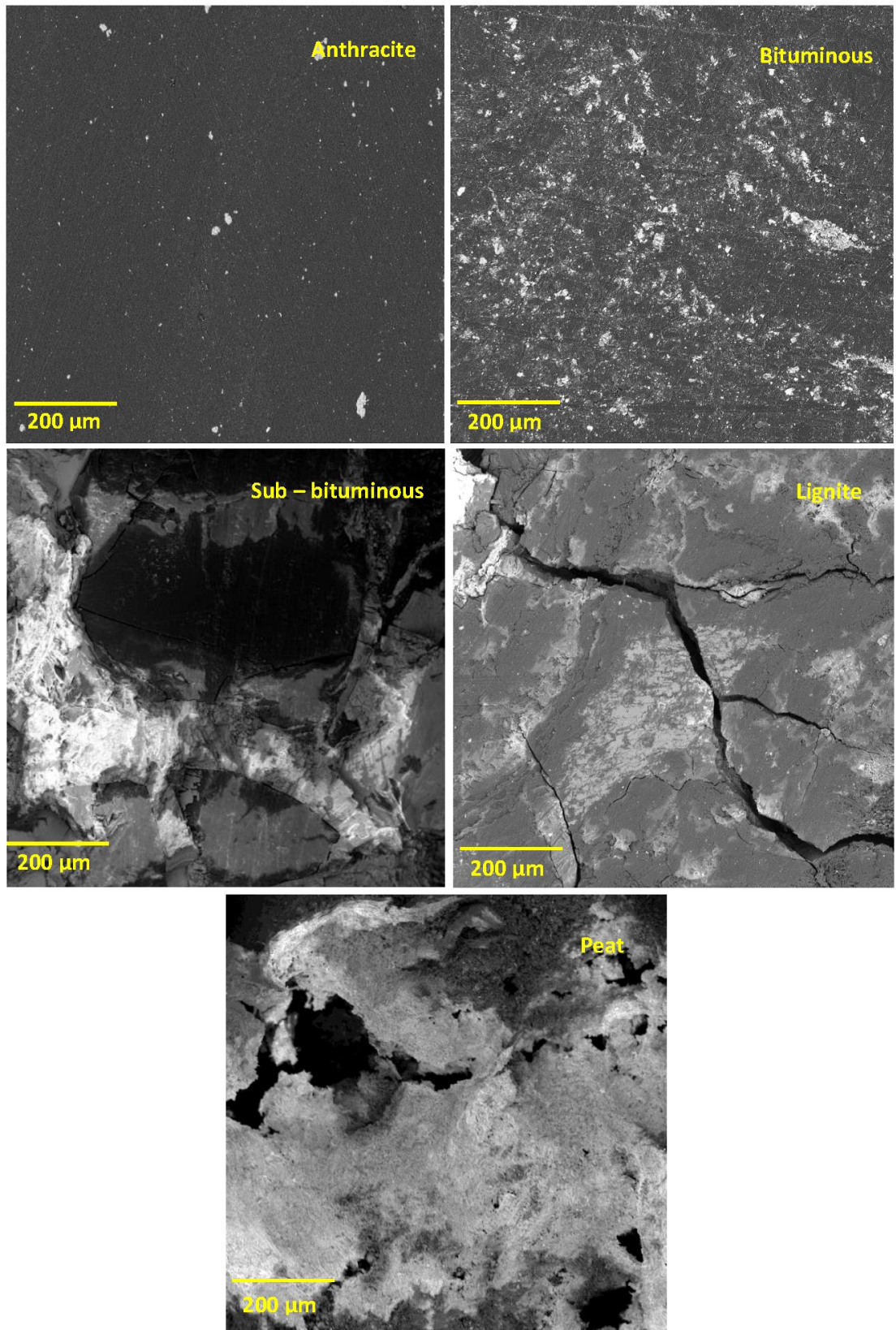
Figure 2-1 The SEM images for the coal samples from high to low rank: anthracite, bituminous, sub-bituminous, lignite, and peat.

Table 2-2 The XRD data for the crystallized minerals inside the coal samples (wt %).

Minerals	Anthracite	Bituminous	Sub-bituminous	Lignite
Illite	34	17	_	_
Kaolinite	24	30	3	24
Calcite	_	_	96	_
Quartz	21	41	1	76
Anatase	21	_	_	_
Montmorillonite	_	6	_	_
Illite-montmorillonite	_	6	_	_

2.2.2   High resolution microCT scanning

The small cylindrical coal plugs (5 mm diameter, 10 mm length) was imaged at high resolution (3.43 μm voxel size was selected) by a Xradia Versa-XRM instrument (cp. Iglauer et al. 2016, Zhang et al. 2016c, Zhang et al. 2016d, Zhang et al. 2016e) at ambient laboratory conditions (atmospheric pressure and 295 K), see Figure 2-2. During the scanning, 2000×2000 pixel detector was used for the radiograph acquisition, and the X-ray accelerating voltage set as 60kV. Each scanning took around 4 to 6 hours. Then all obtained microCT images were filtered with a 3D non local means filter method for noise remove (Buades et al. 2005) and segmented with a watershed algorithm for phase segmentation (Mangan and Whitaker 1999) using Avizo 9.1 software, then continually with qualitative and quantitative analysis (cp. Iglauer et al. 2013; Jing et al. 2017; Zhang et al. 2016b).
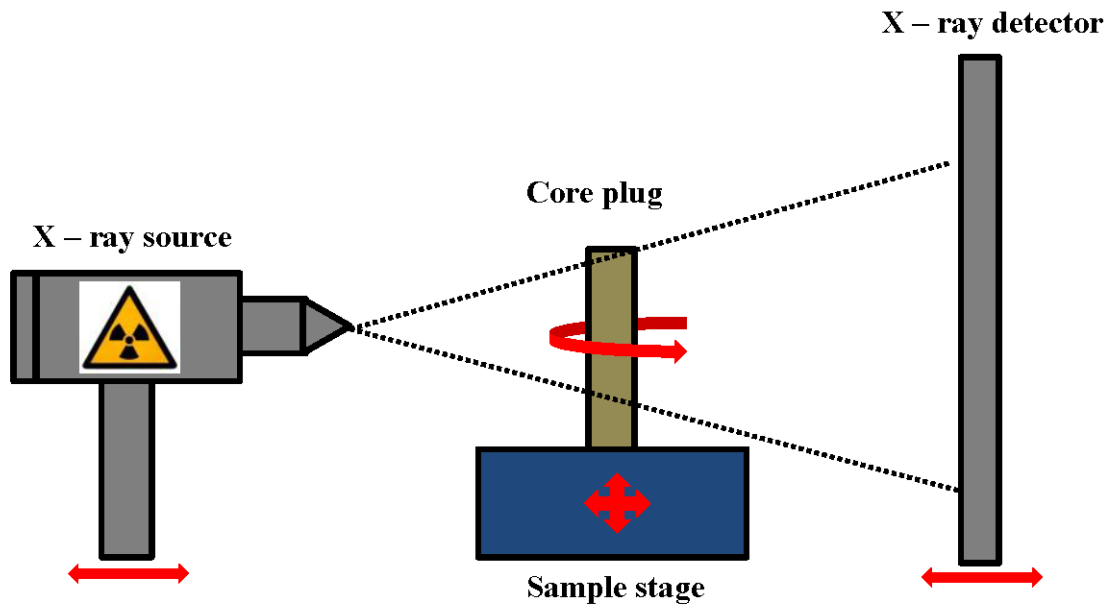
Figure 2-2 Schematic of the microCT scanning system.

2.2.3 Nanoindentation test

The IBIS Nanoindentation System from Fischer-Cripps Laboratories and Berkovich nano-indenter were selected for the nanoindentation test in this study (Figure 2-3). Prior to the tests, the samples were polished with a diamond abrasive paste (3 μm); then the tested sample amounted into the sample stage of the system. The indenter penetrates into the sample as loading stress increasing from 0 mN to 4mN, and the sample's surface undergoes plastic or elastic deformations; then the indenter goes up and releases the loading stress with a typical curve of the penetration depth (h) with "loading-unloading" force (P) are recorded. We selected the method proposed by Oliver and Pharr based on the Sneddon solutions to analysis the output data which has been thought as the most challenge work in the nanoindentation test, where the indentation modulus E_M (also called reduced modulus) is defined as (Fischer-Cripps 2011):

28

$$\frac{1}{E_M} = \frac{1-v^2}{E} + \frac{1-v_i^2}{E_i}$$

3-1

where for E is the Young's modulus for the test sample, v is the Poisson ratio for the test sample, Ei is the Young's modulus for the indenter, and vi is the Poisson ratio for the indenter. And the indentation modulus EM can obtain from the recorded P – h curve (Fischer-Cripps 2011):

$$E_M = \frac{dP}{dh} \frac{1}{2\beta} \frac{\sqrt{\pi}}{\sqrt{A}}$$

3-2

where A is the contact area, dP / dh is the slop of the unloading curve from the maximum applied force P_{max} and maximum penetration depth h_{max} (see C in Fig. 3), and the β set as 1.034 for the Berkovich indenter (King 1987).
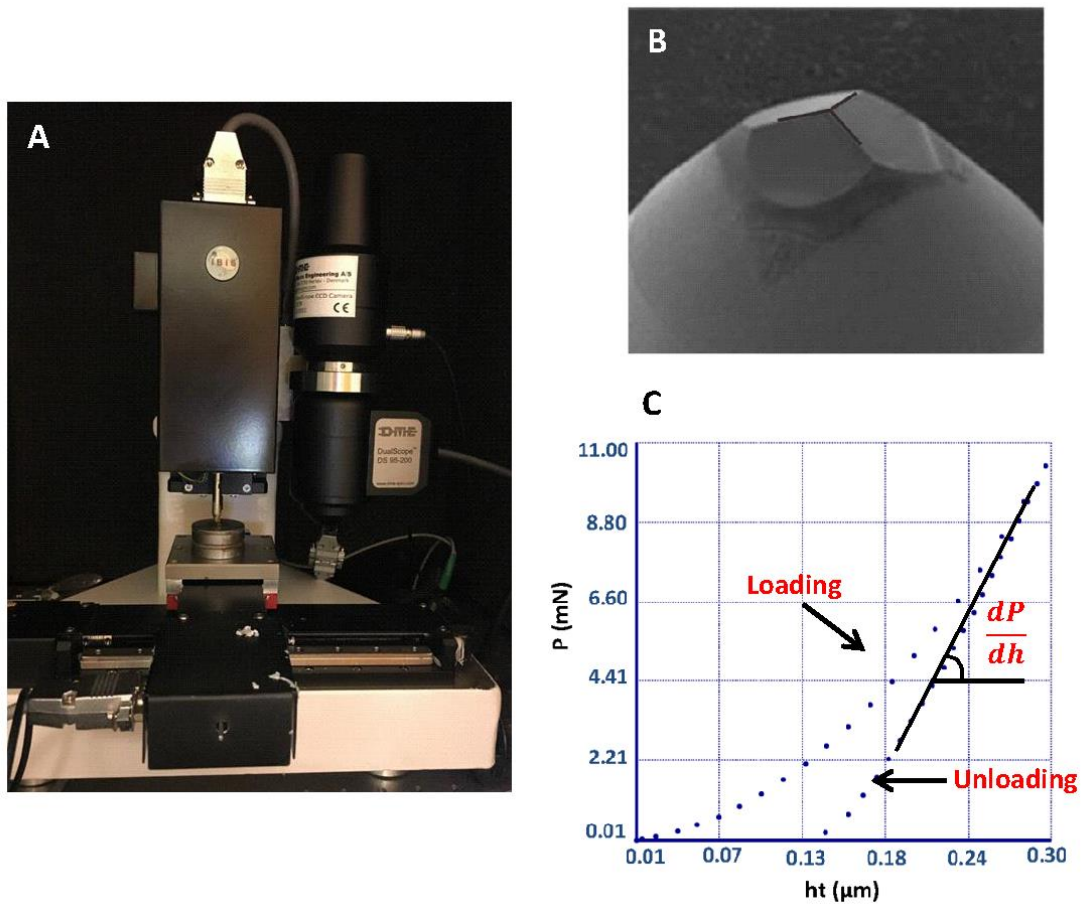
Figure 2-3 (A) Photo of the IBIS Nanoindentation System; (B) the Berkovich nano indenter; (C) a typical P (indentation force) − ht (indentation depth) curve for a calibration sample (quartz), with Young's modulus 72.5 GPa, Poisson's ratio 0.17, and a measured indentation modulus of 74.5 GPa.

2.3 Results and discussion

2.3.1 Pore scale morphology heterogeneous

The 2D raw microCT slices (voxel size: 3.43μm) were presented in Figure 2-4 and the 3D raw images were summarized in Figure 2-5, where the coals could be simply separated into three phases: the pores/fractures (black − the darkest part of the raw images), coal matrix (grey), and minerals (white, the highest radiodensity). Overview, the microstructure morphology was quite different for the different coal samples where the peat had the abundant pores system and the sub-bituminous had the largest amount of mineral phase. In particular, the pores inside the peat was quite large with the diameter can reach to the mm scale, the crystallized minerals random presented inside the coal matrix with each other, and the matrix was not compact. Such microstructure reflected the low pressure and low temperature sedimentary environment (McCabe 1984). For the lignite sample, the lamina can be clearly seen which represented to the horizontal sedimentary layer, and the pores/fractures majorly located between the lamina with a high aspect ratio (could reach to 300; e.g. 0.1 mm width with 3mm length); the crystallized mineral existed between the lamina. For the sub-bituminous sample, large amount of mineral vein presented as grid to connect to each other, such morphology somewhat resembled the coal cleats system (face cleats and butt cleats) which indicated the calcite invasion into the cleats

system after the coal seam formed (Zhang et al. 2016e; Solano-Acosta et al. 2007; Karacan and Okandan 2000; Su et al. 2001); the micro cleats/fractures were mainly located between the mineral phase and matrix, also in the matrix. The bituminous coal had the significant bed morphology where the mineral phase could indicate the horizontal layer structure, however, the voids/pores were not much in this sample. The anthracite was the highest rank coal in our samples, which had cleaner morphology – a uniform coal matrix with some slightly cloudy minerals; moreover, a clear fracture perpendicular crossed the coal sample.
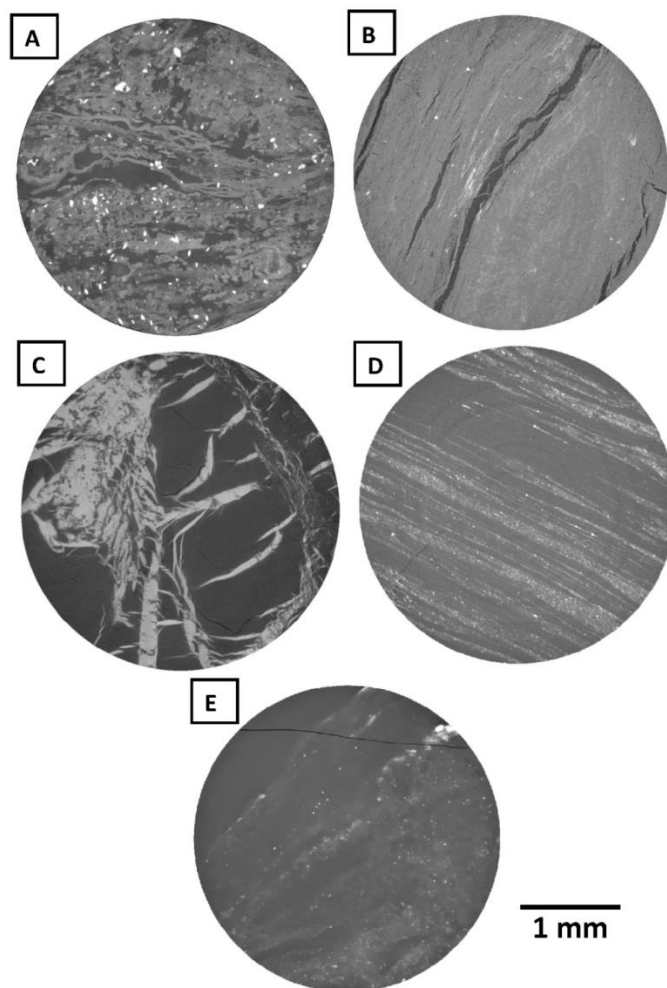
Figure 2-4 The raw microCT images (3.43 μm voxel size) for the tested coal samples: (A) peat; (B) lignite; (C) sub-bituminous; (D) bituminous; (E) anthracite.
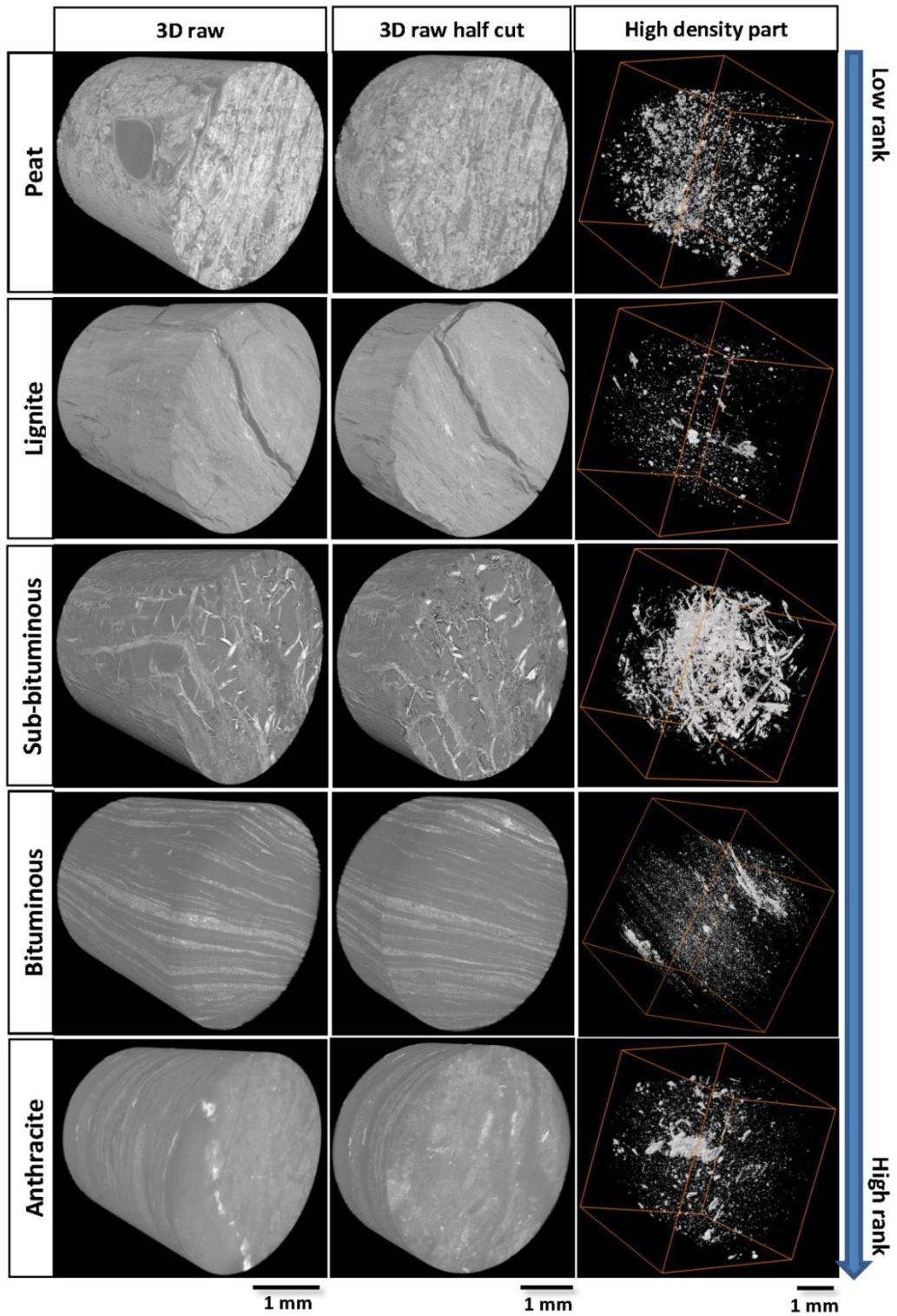
Figure 2-5 The 3D raw microCT images for the coal samples from low to high rank.

After the image processing steps (see Iglauer et al. 2016; Zhang et al. 2016c), these greyscale raw images were successfully segmented to three phase: pores/fractures, minerals, and coal matrix (see Figure 2-6).We The 3D visualization images of the pores/fractures and coal matrix are also presented in Figure 2-7 and quantified the volume fraction in Figure 2-8, where the peat had the highest pore volume fraction (16.86%) and the sub-bituminous had the highest mineral volume fraction (30.08%); the details of the volume fraction for each coal sample were tabulated in Table 2-3. We can see that the low rank coal has more pore volume fraction. However, the mineral phase volume fraction result was quite different with the ash content (mineral matter, wt%) where the sub-bituminous coal had the highest mineral phase volume but lowest ash content (wt%), it could be explained by such mineral phase had high porosity and many other crystalized minerals inside the coal matrix for other coal samples was too small (with mixed with coal matrix) to capture during the image processing (for instance, some tiny mineral phase – white "cloudy part" in anthracite cannot be separated and be treated as coal matrix); such mineral matters could be both detrital and authigenic in natural and their distribution was variable in the different coal seams (Vassilev et al. 1996), thus we concluded that such mineral volume fraction was not a function with coal ranks.

The coal pores/fractures system was extremely important for the coal bed methane (CBM), enhanced coal bed methane recovery (ECBM), and carbon dioxide storage; which directly influence the permeability and adsorption capacity (Li et al. 2017, Mostaghimi et al. 2017, Zhang et al. 2016e). Here the pore (fracture or cleat) size

(3D volume, µm3) distribution was measured for the different coal rank samples, see Figure 2-9. The peat had a large amount of "big pore" where it has the highest number of the pores >1000 μm^3; and the peak area was between 100 μm^3 to 1000 μm^3 which were one order larger than lignite – the pores 'size mainly located at 10 μm^3 to 100 μm^3. However, we noticed that the distribution figure (Figure 2-9 B) somehow became flat from lignite to anthracite, which means the less tiny pores and more fractures/cleats fraction – indicated the coal matrix became tight as the coal rank increasing.

Moreover, the average pore size was also obtained, they are 21727 μm^3, 6105 μm^3, 825 μm^3, 1127 μm^3, and 7378 μm^3 for peat, lignite, sub-bituminous, bituminous and anthracite separately. Such results were consistent with former researchers where the pore cleat spacing varies with coal rank, decreasing from lignite through bituminous and increasing through anthracite coals – a bell shaped distribution (Laubach et al. 1998). Thus, it can be concluded that the medium rank coal always has the poor pore/cleat system (combine the microCT morphology results, we suggested the original cleats were invaded by detrital minerals); moreover, the low rank coal has the most abundant pore system (including large pores and tiny pores) and high rank coal has the more mature fracture system.
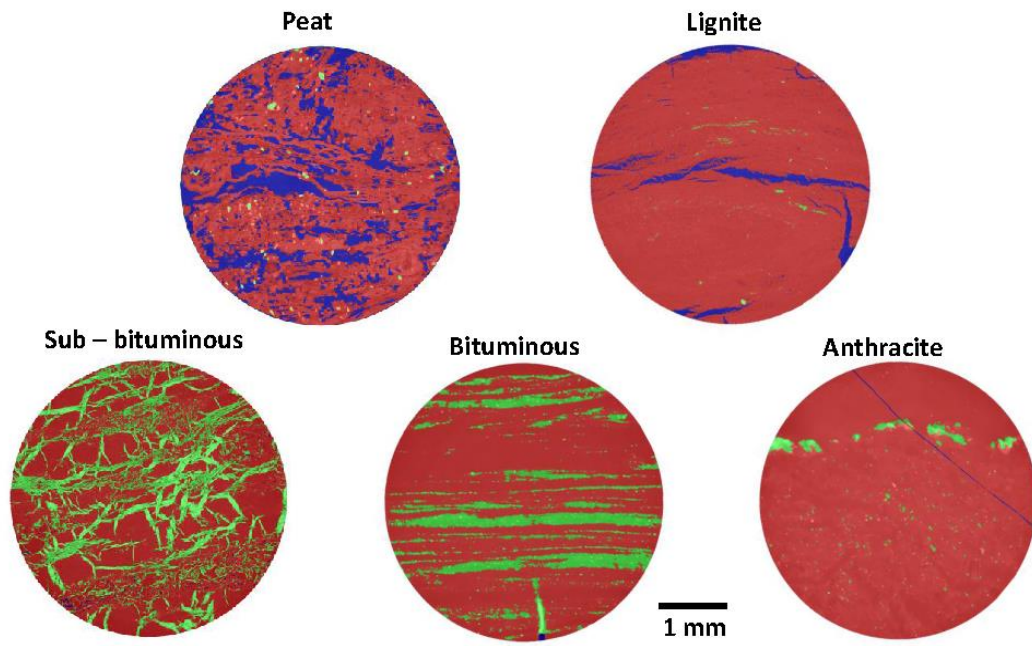
Figure 2-6 The 2D slice for different rank coals after image segmentation where the blue is the pores/fractures, green is the mineral phase, and red is the coal matrix base.
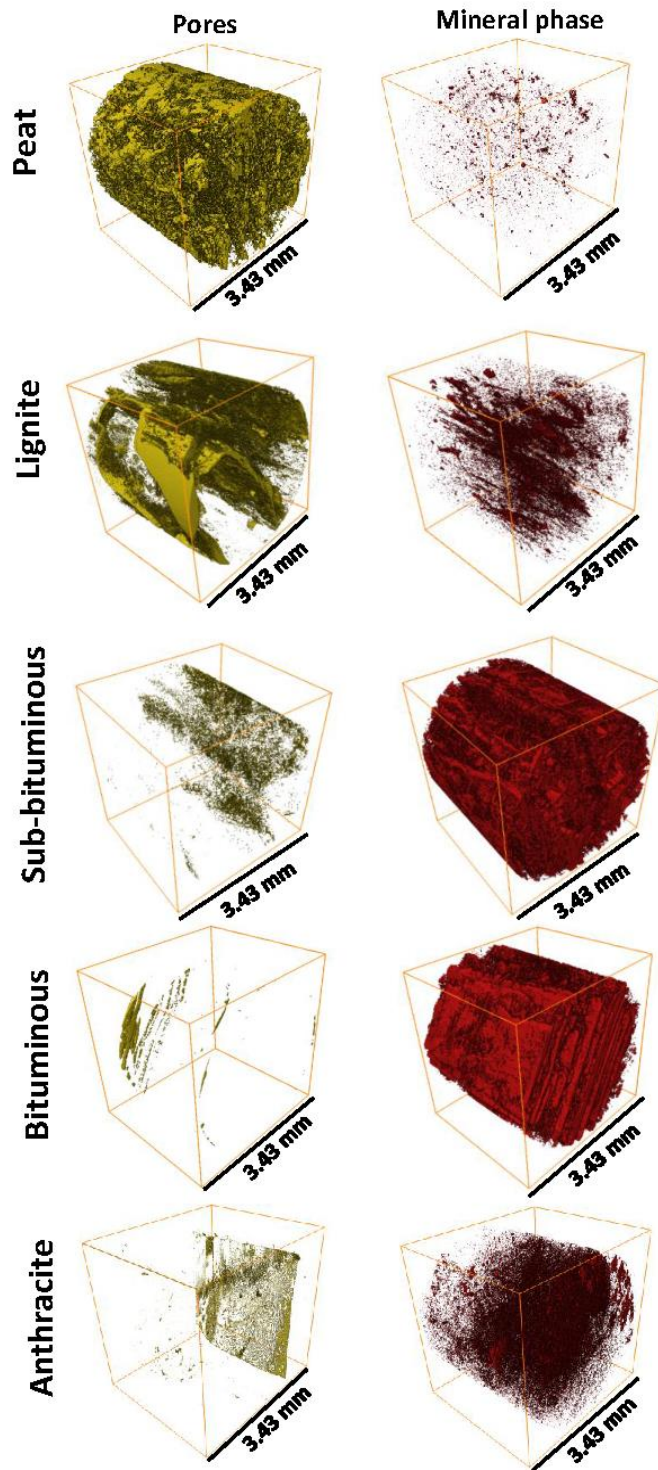
Figure 2-7 3D visualization of the pores and mineral phase for different rank coal samples, the nominal resolution is 3.43 µm.
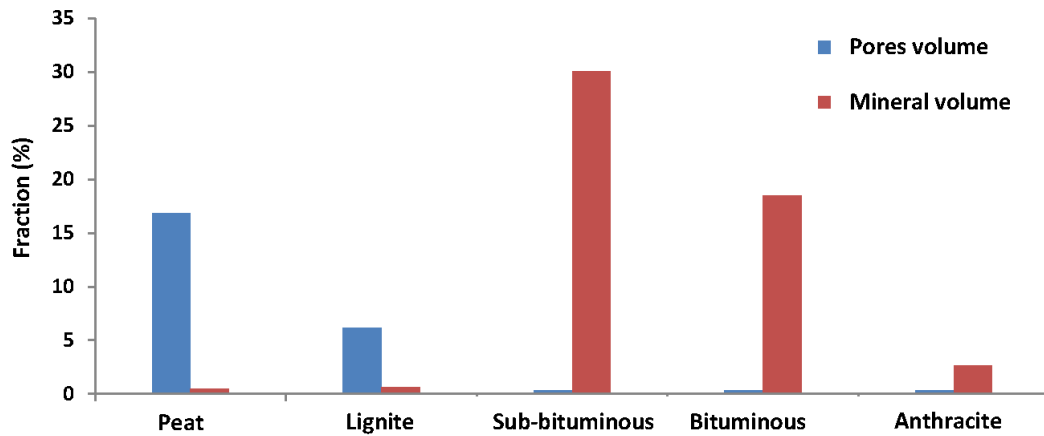
Figure 2-8 The imaged based volume fraction for all coal samples, where the peat has the largest pore volume fraction and sub-bituminous has a largest mineral phase volume fraction.

Table 2-3 The data of the volume fraction (image based) for different rank coal samples.

Sample	Pores/fractures (%)	Coal matrix (%)	Mineral (%)
Anthracite	0.33	97.01	2.66
Bituminous	0.06	81.44	18.50
Sub-bituminous	0.30	69.62	30.08
Lignite	6.16	93.23	0.61
Peat	16.86	82.64	0.50
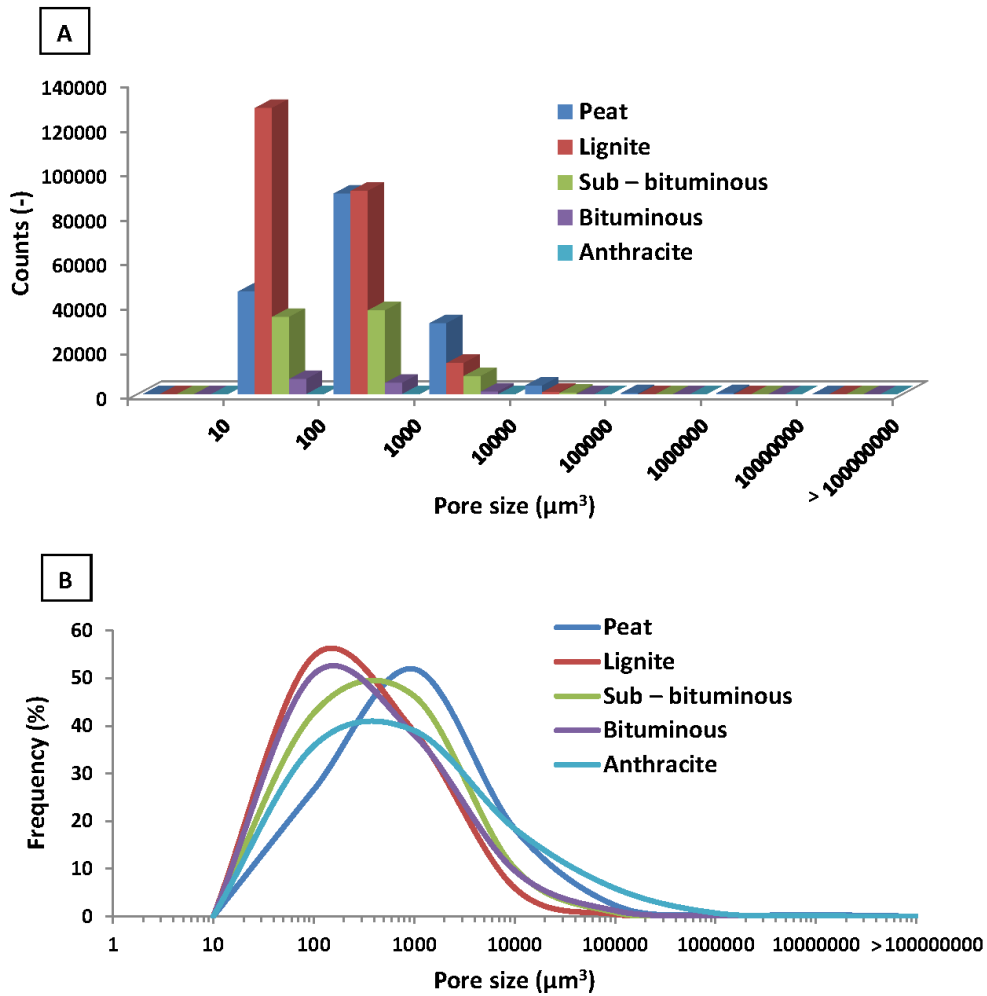
Figure 2-9 The pore size distribution for different rank coal samples, (A) by counts (-); (B) by frequency (%).

2.3.2 Pore scale rock mechanical heterogeneous

Totally 961 effective tested points were obtained for each anthracite, bituminous, sub-bituminous, and lignite sample. However, we only obtained 31 valid test points on peat (for total 961 tests conducted) due to such material was so loose concentration where most of the loading indenter went inside the large pores. Thus we only presented the indentation modulus E_M (GPa) distributions for the anthracite, bituminous, sub-bituminous, and lignite coal samples (see Figure 2-10 A); it was clear show that the crest moves to the right (E_M increased) from low to high rank coal

sample. Moreover, the heterogeneity of sub-bituminous coal also reflected on the distribution figure where it had the highest amount of EM larger than 20 GPa – consistent with the morphology analysis where it had the highest mineral volume fraction; such crystalized mineral phase always has much higher elastic modulus than coal matrix (cp. Zhang et al. 2016a; Lebedev et al. 2014; Zhang et al. 2017). The average indentation modulus for each coal sample was presented in Figure 2-10 B, it is clear show that the coal became rockmechanical weak from high rank (anthracite coal) to low rank – it decreased around half to lignite and 90% to peat. We thus suggested that the safety issues (geohazard) for low rank coal seam should be always priority than high rank coal seam (due to lower indentation modulus) for the coal seam exploration, CBM/ECBM, and CCS projects.

To investigate how and which parameter control such indentation modulus, the indentation modulus with four important petrophysical properties were compared (Figure 2-11): moisture content M (%), volatile matter V (%), ash A (%), and fixed carbon content Cf (%). The results show that the indentation modulus and moisture content / volatile matter were in inverse proportion. However, the indentation modulus had the positive relationship ash percentage - which directly presented that the mineral matter could improve the rockmechanical performance of the coal. Furthermore, the most important, the indentation modulus had the strongest (positive) relationship (see Figure 2-11 D) with carbon content where a trendline best fitted the tested data with $R^2 = 0.99$, the trendline equation could be expressed as

$$E_M = 0.1137C_f + 0.5458 \hspace{4cm} 3\text{-}$$

Thus the carbon contend was the main parameter to determine such pore scale rock mechanical property.
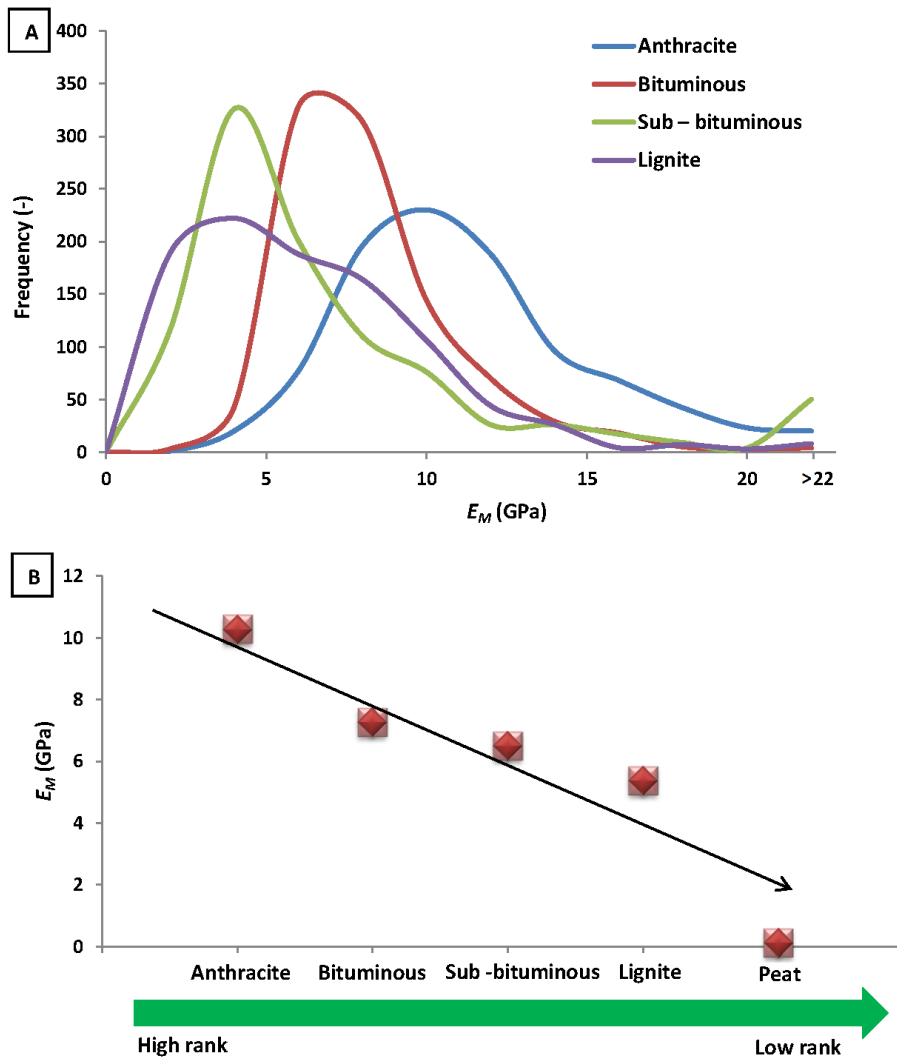
Figure 2-10 (A) The indentation modulus E_M (GPa) distribution for coal samples; (B) the (average) indentation modulus E_M (GPa) as a function of the coal rank.
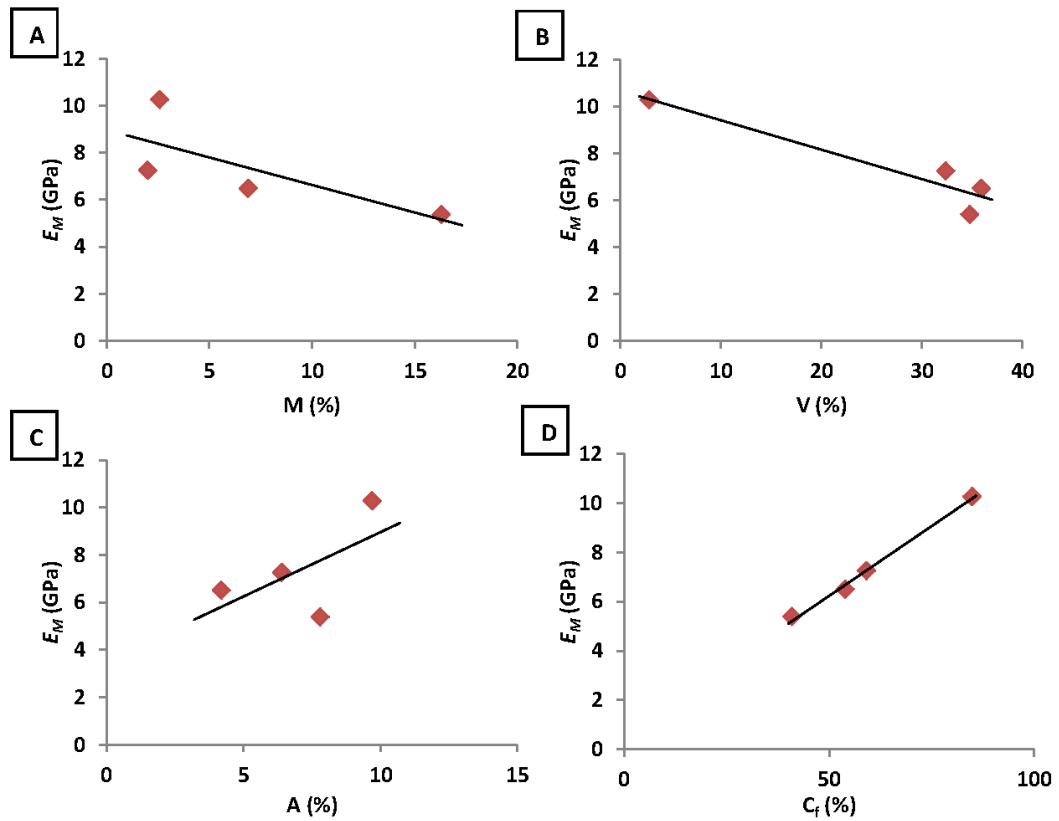
Figure 2-11 The relationship of indentation modulus (E_M) with coal petrophysical properties, (A) the moisture content M (%); (B) volatile matter V (%); (C) ash A (%); (D) fixed carbon content C_f (%).

2.4　Conclusion

The coal microstructure and rockmechanical properties are extremely important for the deep coal seam exploration, CBM/ECBM, and carbon dioxide geosequestration. However, the coal is kind of very complex materials and could be separated from low to high rank coal based on the maturity. However, how coal microstructure and rockmechanical properties related to the coal rank are only poorly understood. Thus, in this paper, the high resolution (3.43 µm voxel length) microCT scanning and nanoindentation test were conducted on anthracite, bituminous, sub-bituminous, lignite, and peat. The results show that the different coal has quite different

microstructure where the low rank coal has more volume fraction and sub-bituminous coal has mineral phase, and the average pore size is a function of the coal rank – a bell shaped distribution (Laubach et al. 1998). The indentation modules increased as the coal rank build up and such indentation modules have high correlation with "fixed carbon content" of the coal. The conclusion of this chapter is that the low rank coal has the most abundant pore system (including large pores and tiny pores) and high rank coal has the more mature fracture (cleat) system; and the safety issues (geohazard) for low rank coal seam should be always in priority consideration than high rank coal seam for the coal field exploration, CBM/ECBM, and CCS projects.

Chapter 3 Coal microstructure change under different effective stress

Note that this chapter has published as a journal paper:

Abstract

Gas permeability (k) and porosity (ϕ) are the most important parameters in CBM/ECBM and CCS in deep unmineable coal seams. k and φ depend on the coal micro structure, and k and ϕ significantly change with varying effective stress. However, how the coal micro structure is related to such permeability and porosity changes is only poorly understood. This chapter thus imaged sub-bituminous coal samples at two resolutions (medium - 33.7 µm and high - 3.43 µm voxel size) in 3D with an x-ray micro-computed tomograph as a function of applied effective stress; and investigated how cleat morphology, k and φ are influenced by the changes in effective stress and how these parameters are interrelated. In the images, three phases were identified: micro cleats (void), a mineral phase (carbonate) and the coal matrix. When effective stress increased, the micro cleats became narrow and closed or disconnected. This resulted in a dramatic permeability drop with increasing effective stress, while porosity decreased only linearly.

Keywords

3.1 Introduction

Gas permeability is a key factor in coal bed methane (CBM) and enhanced coal bed methane recovery (ECBM), and carbon geo-sequestration in deep unmineable coal seams (Pekot and Reeves, 2002; Moore, 2012). It is well established that gas permeability is highly sensitive to effective stress (Harpalani and Chen, 1992; Palmer and Mansoori, 1996; Karacan and Okandan, 2000; Connell et al., 2010; Cai et al., 2014). This is directly relevant for field production processes, e.g. in ECBM another gas (e.g. nitrogen) is frequently injected to increase the reservoir pore pressure (and thus reduce effective stress) to release methane; or during CBM production reservoir pressure is depleted and effective stress increases. In this context it has been shown that permeability increases by matrix shrinkage due to methane desorption, or permeability decreases by cleat compaction due to pore pressure loss (Harpalani and Chen, 1997; Kumar et al., 2012). It also has been well documented that permeability decreases drastically with depth (because the overburden stress and thus effective stress increase), and it has been suggested that this is caused by fracture closure (Enever et al., 1999). However, most investigations on coal permeability change focus on the coal swelling effect during gas injection (e.g. CO_2: e.g. Reeves, 2004; Larsen, 2004; Siriwardane et al., 2009) or water encroachment (e.g. Zhang et al., 2016; Stevens et al. 2004); while the influence of effective stress on permeability and associated coal micro structural changes are still poorly understood.

44

Traditionally dual coal porosity and permeability sets are distinguished, one for the coal matrix and the second set for the natural fracture (cleats) network. The permeability of the coal matrix is much lower than that of the cleats network, thus the cleats network effectively controls the overall permeability of the coal seam (Harpalani and Chen, 1992; Karacan and Okandan, 2000; Connell et al., 2010). Furthermore, cleats can be subdivided into butt cleats, which are orthogonal to the coal bedding, and face cleats, which are perpendicular to the coal bedding (Laubach et al., 1998). Cleat properties such as size, structure, orientation, and connectivity all significantly affect permeability (Laubach et al., 1998; Flores, 2013). It has been thought that the cleats change when the in-situ stresses change (Chen et al., 2011). Besides the large scale, the "cleats form" also existed in microscale. However, the variation of the microstructural morphology associated with such changes, especially in micro cleats (less than 20 μm), which are common in the coal matrix (Gamson et al., 1993), is only poorly understood.

Typically such microscale investigations are performed via SEM measurements (e.g. Huggins et al., 1980; Kutchko et al., 2013; Ye et al., 2013), and these give a very high resolution (up to 1-20 nm voxel size); however no effective stress can be applied during such a measurement and only 2D images at vacuum conditions can be obtained. The 3D pore morphology, however, is of key importance as it determines the permeability (2D is insufficient information, Stauffer 1979). However, recent developments in the area of x-ray micro-computed tomography (microCT) applied in core analysis (e.g. Iglauer et al., 2011; Lebedev et al., 2014; Rahman et al., 2016) enable the application of effective stresses to a sample while it is imaged in-situ in 3D at high resolution.

It thus microCT imaged the coal micro structures and their changes in 3D at high resolution as a function of effective stress in-situ and related these changes to independent gas permeability and porosity measurements.

3.2 Methodology

3.2.1 Materials

A coal block was acquired from a famous coal mine in the middle of China: the Pingdingshan coal mine, Henan Province. This coal block was identified as sub-bituminous with a fixed carbon content of 54% ($\pm$2%) and volatile matter content of 36% ($\pm$1%) measured by Chinese Standard GB/T 212-2008 and DL/T 1030-2006; additional properties of this coal are tabulated in Table 3-1. We specifically selected this coal, because at such low carbon content (less than 75%) always a significant cleat system prevails (Clarkson and Bustin, 1999), which is advantageous when studying the influence of effective stress on cleat morphology and associated changes in permeability. Standard cylindrical (38.1 mm diameter and 76 mm length) core plugs were drilled out of the coal block parallel to the coal bed direction; these plugs were subjected to microCT scanning (Xradia VersaXRM instrument) and gas (N_2) permeability tests in an AP 608 instrument. Furthermore, smaller cylindrical coal plug (5 mm diameter and 10 mm length) were cut from the same coal block adjacent to a position from which the larger plugs were drilled. These smaller plugs were also microCT imaged, but at a much higher resolution, see below.

Furthermore, SEM-EDS tests were performed on more than 10 samples cut from the same coal block, and cleats, coal matrix and a mineral phase were clearly identified, Figure 3-1. The micro cleats can be divided into three groups according to their

spatial position; micro cleats in the coal matrix (e.g. Figure 3-1A), the micro cleats between coal matrix and mineral phase (e.g. Figure 3-1B), and micro cleats in the mineral phase (e.g. Figure 3-1D). The mineral phase was identified as calcium carbonate via EDS analysis; these carbonates also filled in some cleats (e.g. Figure 3-1C).

Table 3-1 Physical properties of the coal studied.

ρ (g/cm^3)	M_{ad} (%)	V_{daf} (%)	A_{ad} (%)	C_f (%)	E (GPa)	υ
1.35	6.90	36.00	4.20	54.00	2.60	0.31
($\pm$0.03)	($\pm$0.50)	($\pm$1.00)	($\pm$0.20)	($\pm$2.00)	($\pm$0.40)	($\pm$0.1)

Note: ρ is the bulk density; M_{ad} is the moisture content; V_{daf} is the volatile matter; A_{ad} is the ash yield; C_f is the fixed carbon content; E is Young's Modulus; and υ is Poission's ratio. All properties were measured using Chinese Standard GB/T 212-2008.
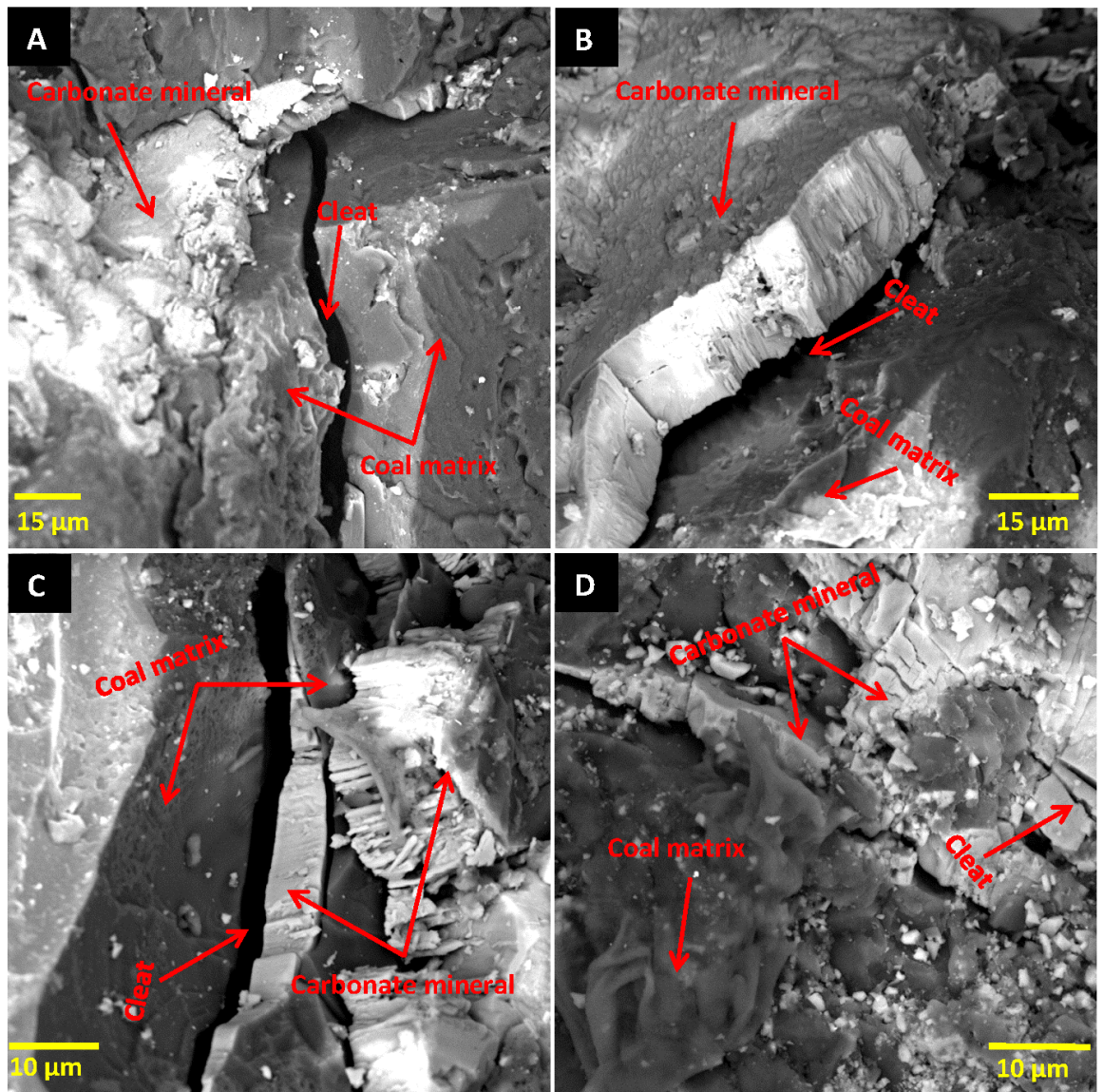
Figure 3-1 SEM images of the coal sample's surface, where the coal matrix, mineral phase and cleats were clearly identified. (A) cleat inside the coal matrix; (B) cleat between the coal matrix and the mineral phase; (C) minerals filled in the cleat (D) cleat inside the mineral phase.

3.2.2 Gas permeability measurements

We selected nitrogen for our gas permeability tests (conducted with an AP-608 automated porosimeter-permeameter, accuracy $\pm$ 0.1 %) in order to minimize

swelling (note that nitrogen causes only a minimal swelling effect: volume strain and linear strain ratio is ≤ 0.2 %, George and Barakat, 2001) and guarantee a minimum degree of gas slippage (Wang et al., 2014). The pore pressure was set constant at 1.38 MPa during the test, while the confining pressure was stepwise increased from 3.5 MPa to 24 MPa. Thus effective stresses from 1.12 - 22.62 MPa were investigated. Four coal plugs (38 mm diameter and 76 mm length, marked as A, B, C, and D) underwent this gas permeability test matrix.

3.2.3   Micro-CT in-situ imaging

An in-situ micro-CT scanning apparatus was set up (Figure 3-2), where two different X-ray transparent core holders can be used and different plug sizes imaged (5 mm diameter plugs, "small plugs", cp. Iglauer et al., 2011; Rahman et al., 2016; or 38 mm diameter plugs, "large plugs", Lebedev et al., 2014). A high precision syringe pump (Teledyne ISCO 500D) provided the confining pressure by compressing DI water. Initially a large coal plug (sample E) was mounted inside the large diameter core holder (c.p. Figure 3-2 E), and the plug was imaged in-situ at three different effective stresses (0 MPa, 5 MPa and 10 MPa) at $(33.7 \ \mu m)^3$ 3D voxel resolution at ambient conditions (atmospheric pressure and 296 K). Subsequently a small coal plug was imaged in-situ at the same three effective stresses (0 MPa, 5 MPa and 10 MPa), but now at a much higher resolution, $(3.43 \ \mu m)^3$ voxel size. No fluids were injected, i.e. the confining pressures equalled the effective stresses. The x-ray beam diameter was approximately 0.3 μm, and a 1000 x 1000 pixel detector was used for radiograph acquisition. The X-ray accelerating voltage was chosen as 60 kV, and the total acquisition time for one 3D image was approximately 4 hours. The acquired microCT images were then filtered with a 3D non local means filter (Buades et al.,

2005) and segmented with a watershed algorithm (Schlüter et al., 2014) for quantitative analysis using Avizo 9 software, cp. Mathews et al., 2011; Jing et al., 2016; Zhang et al., 2016c.
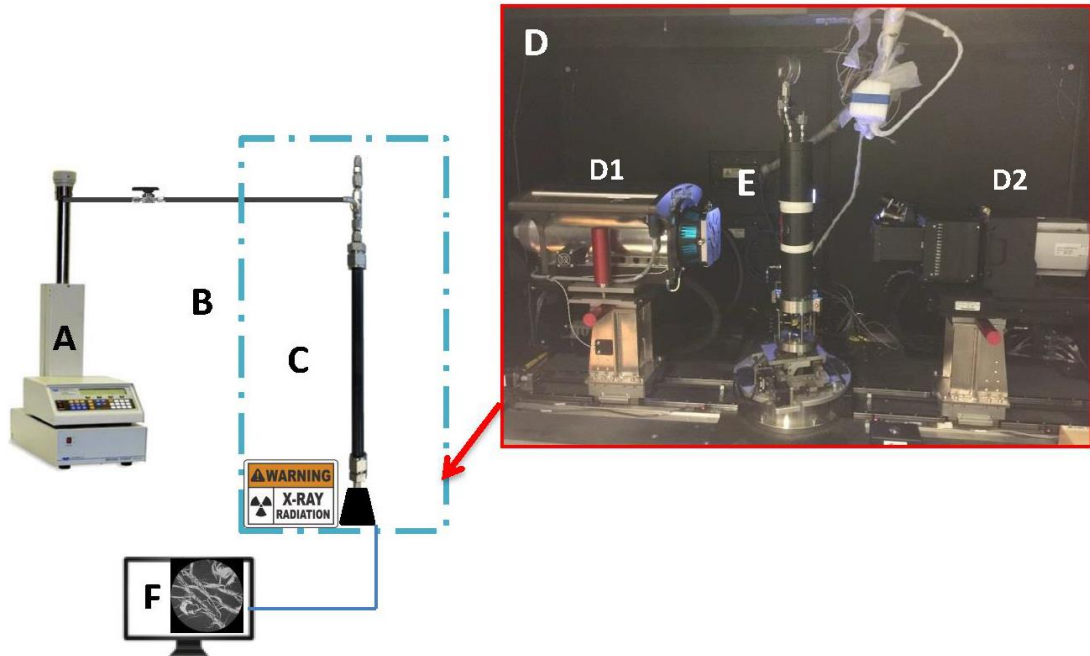
Figure 3-2. Experimental microCT coreflooding apparatus, (A) confining pressure pump, (B) microCT, (C) core holder for small plug sample (plug diameter = 5 mm), (D) microCT inside view, D1 is the X-ray source, D2 is the X-ray detector, (E) is the core holder for large plug samples (plug diameter = 38 mm), (F) images output and processing.

3.3   Results and Discussion

3.3.1   Gas permeability and porosity

Gas permeability (k) and porosity (ϕ) decreased with increasing effective stress (σ) as expected, Figures 3-3 and 3-4. The permeability data followed a power law relation $k = a\sigma^b$, k dropped rapidly when effective stress increased (Figure 3-3),

consistent with earlier investigations (e.g. Chen et al., 2011; Li et al., 2014). However, the porosity decreased only linearly when effective stress increased, Figure 4. We conclude that any incremental change in effective stress in the high effective stress region does not significantly change permeability, while porosity is still significantly affected.
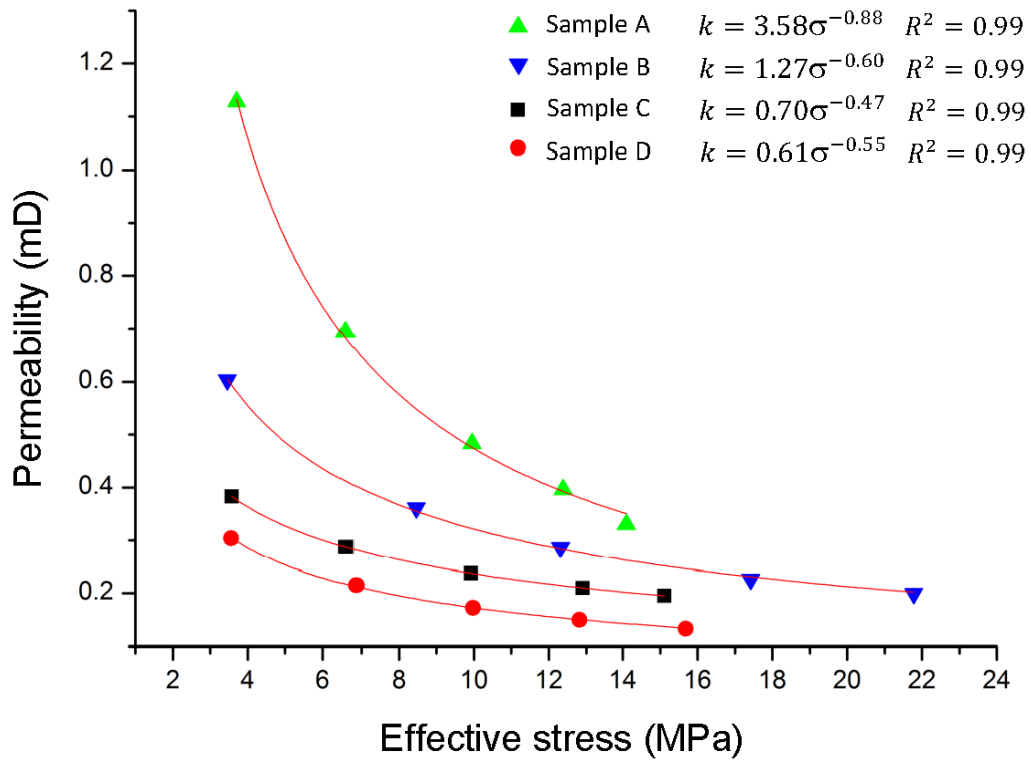
Figure 3-3. Gas permeability versus effective stress for all four coal plugs tested. The fitting equations are shown in the legend together with their Regression Coefficients.
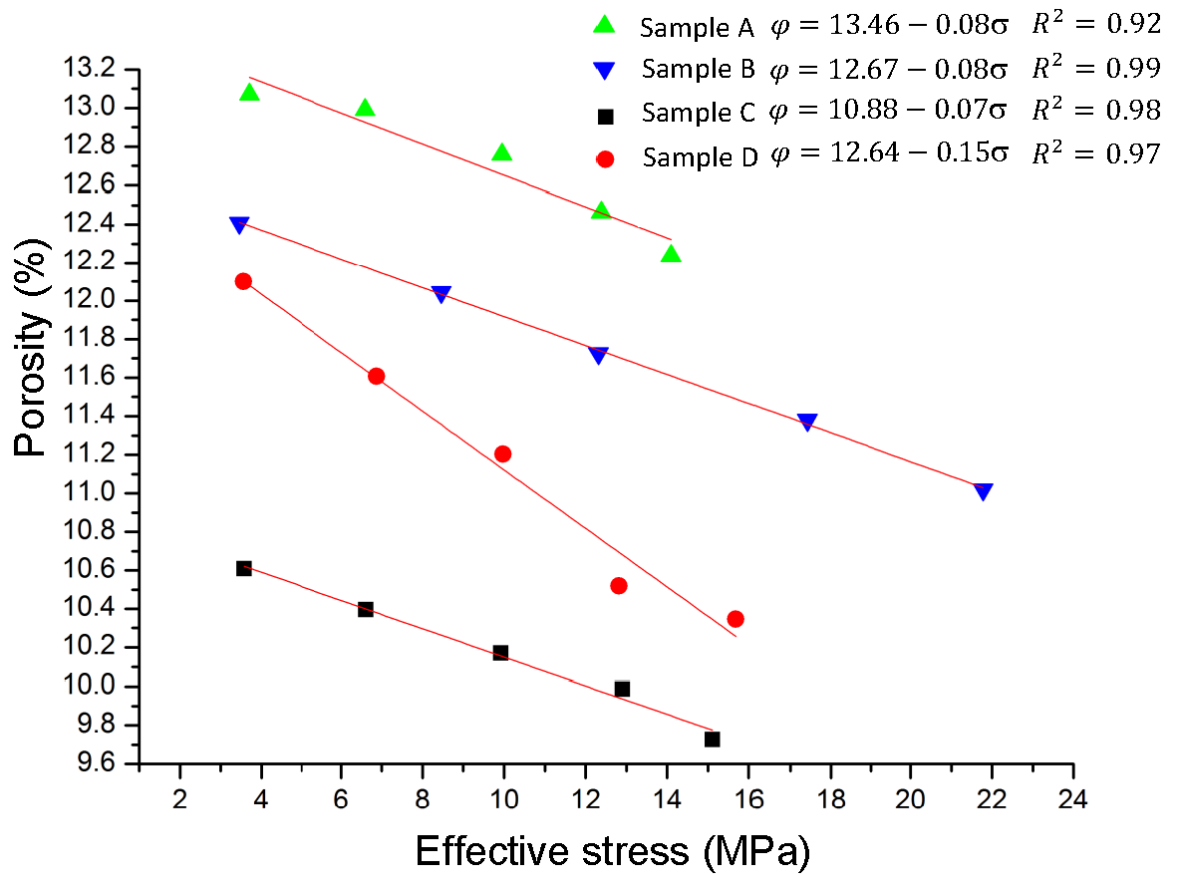
Figure 3-4. Porosity versus effective stress for the four coal plugs tested. The fitting equations are shown in the legend together with their Regression Coefficients.

3.3.2   X-ray micro-computed tomography imaging

3.3.2.1   Qualitative analysis

In the tomograms three phases were identified (Figure 3-5): cleats (black), mineral phase (white) and the coal matrix (grey), consistent with previous microCT images of coal (Yao et al., 2009; Golab et al., 2013; Ramandi et al., 2016; Zhang et al., 2016). A few macro cleats were visible in the large plug which was imaged at medium nominal resolution $(33.7 \ \mu m)^3$, Figure 3-5 A. The macro cleats/fractures were oriented parallel to the mineral veins (Figure 3-6). The macro cleats at 0 MPa

effective stress had a 0.1-0.2 mm width, ~ 1 cm length, and ~ 1.5 cm depth, Figure 3-7, and the macro cleat/fracture volume fraction amounted to ~ 0.5 %; these macro cleats/fractures were almost closed at 5 MPa effective stress and completely closed at 10 MPa effective stress, Figure 3-7. This result thus experimentally confirms the previous hypothesis (McKee et al., 1987; Palmer and Mansoori, 1996; Chen et al., 2011) that cleats close at high effective stress and dramatically reduce coal permeability.

The minerals were also mainly oriented perpendicular to the coal bed, but they showed a stream-like pattern where some mineral streams were connected by perpendicular smaller mineral sub-streams in a ladder-like pattern, "T-junctions". These mineral structures thus somewhat resembled the morphology of "face cleats" and "butt cleats"; this is an indication that mineral invaded and filled the macro cleats after the coal seam formed (Karacan and Okandan, 2000; Su et al., 2001; Solano-Acosta et al., 2007). The structural pattern of the mineral phase, and that it is oriented perpendicular to the coal seam bed, is visualized in Figure 3-6 in 3D. Furthermore, at high resolution, the mineral veins also reveal subtle structural patterns, which were not evident at the medium resolution (Figure 3-5). In addition, when we zoomed in further, micro cleats were visible (Figure 3-5 B); these micro cleats/fractures were randomly distributed in the coal matrix with width ~ 5-10 µm and lengths up to 2 mm. Moreover, light grey tones indicating less x-ray dense mineral are present in the image s (Figure 3-5). This is probably less consolidated calcite (which has nanoporosity which is below the resolution of the microCT images).

When comparing the high resolution images for the three different effective stresses (Figure 3-8) the change in cleat morphology becomes obvious: the micro cleats in the

coal matrix became narrower when effective stress increased (e.g. points 1, 2, and 5 in Figure 3-8), and some of these micro cleats disconnected from each other creating dead ends for flow (e.g. point 7 in Figure 3-8). Moreover, the micro cleats between the matrix and mineral phase disappeared at high effective stress (e.g. points 3 and 4 in Figure 8); however, the micro cleats inside the mineral phase underwent almost no change (e.g. point 6 in Figure 3-8) because the mineral compressibility is significantly lower than that of the coal matrix.
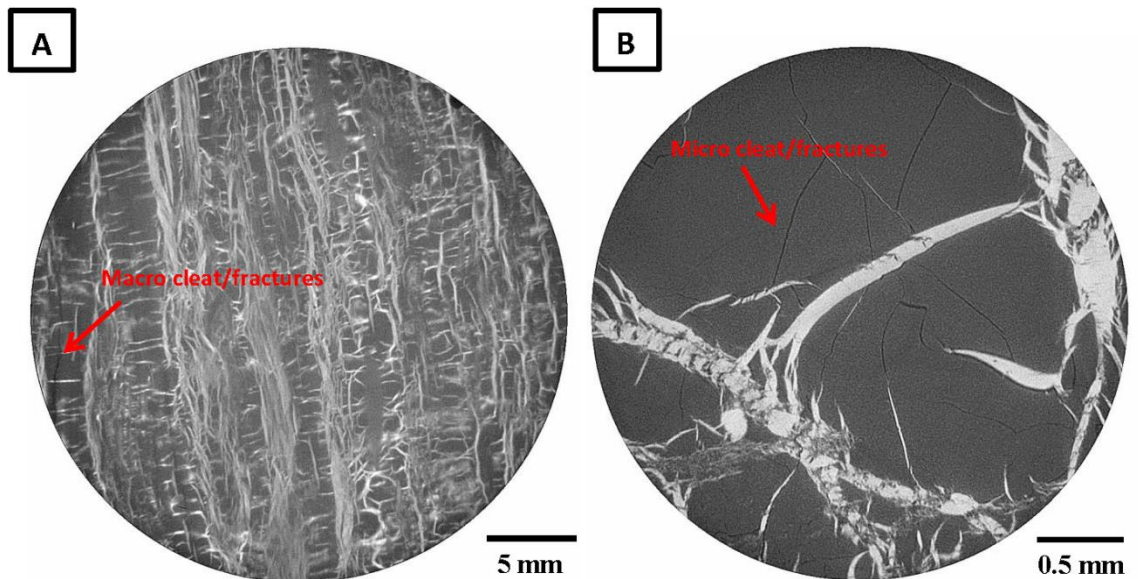
Figure 3-5. 2D slices through the coal microCT images (0 MPa confining pressure), (A) the large coal plug (33.7 μm nominal resolution); (B) the small coal plug (3.43 μm nominal resolution). Minerals are white, coal matrix is grey and cleats are black.
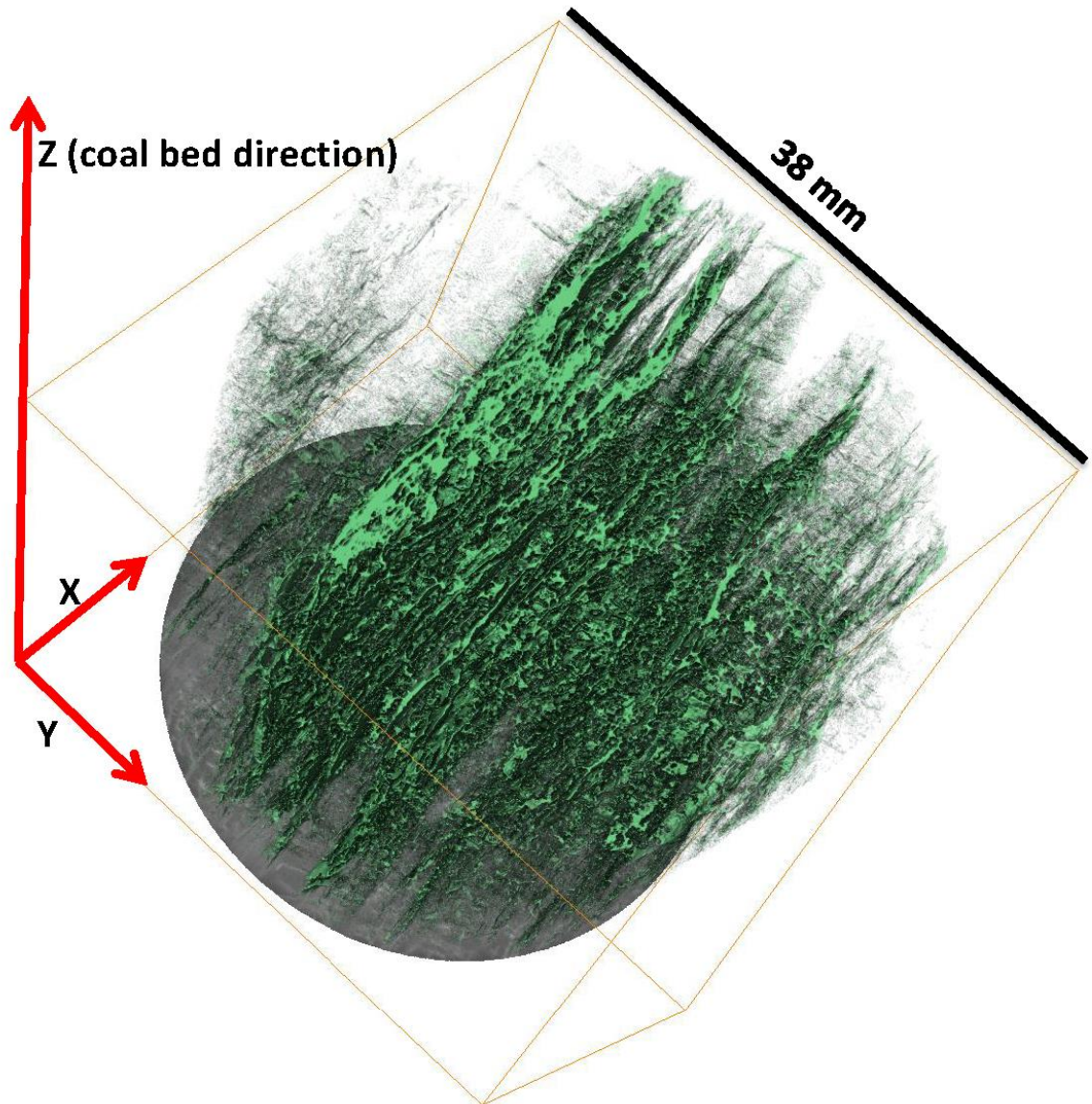
Figure 3-6. 3D visualization of the mineral phase (green) in the large coal plug at 0 MPa effective stress (38 mm diameter, 33.7 μm voxel resolution). The mineral phase is oriented perpendicular to the coal bed direction (z direction).
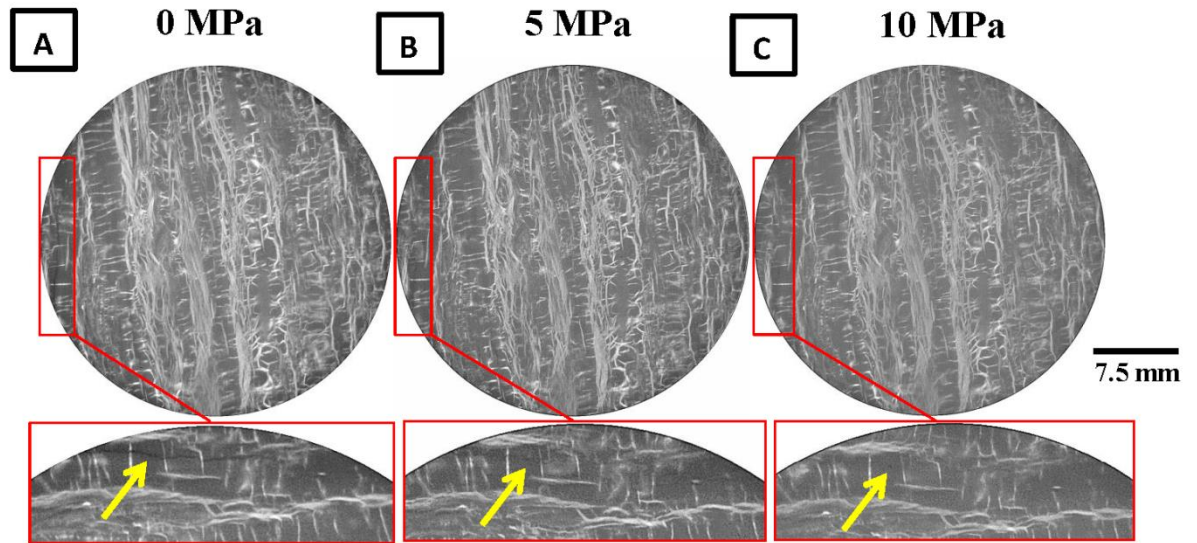
Figure 3-7. Image slices through the large coal plug (38 mm diameter). Mineral is white, coal matrix grey and cleats are black. Different effective stress situations are illustrated: (A) 0 MPa effective stress, (B) 5 MPa effective stress, and (C) 10 MPa effective stress. The macro cleat observed in (A) (see red boxes and yellow arrows) was almost closed in (B) and completely closed in (C). The mineral phase and coal matrix, however, showed no significant change with increasing effective stress. Nominalresolution is 33.4 μm.
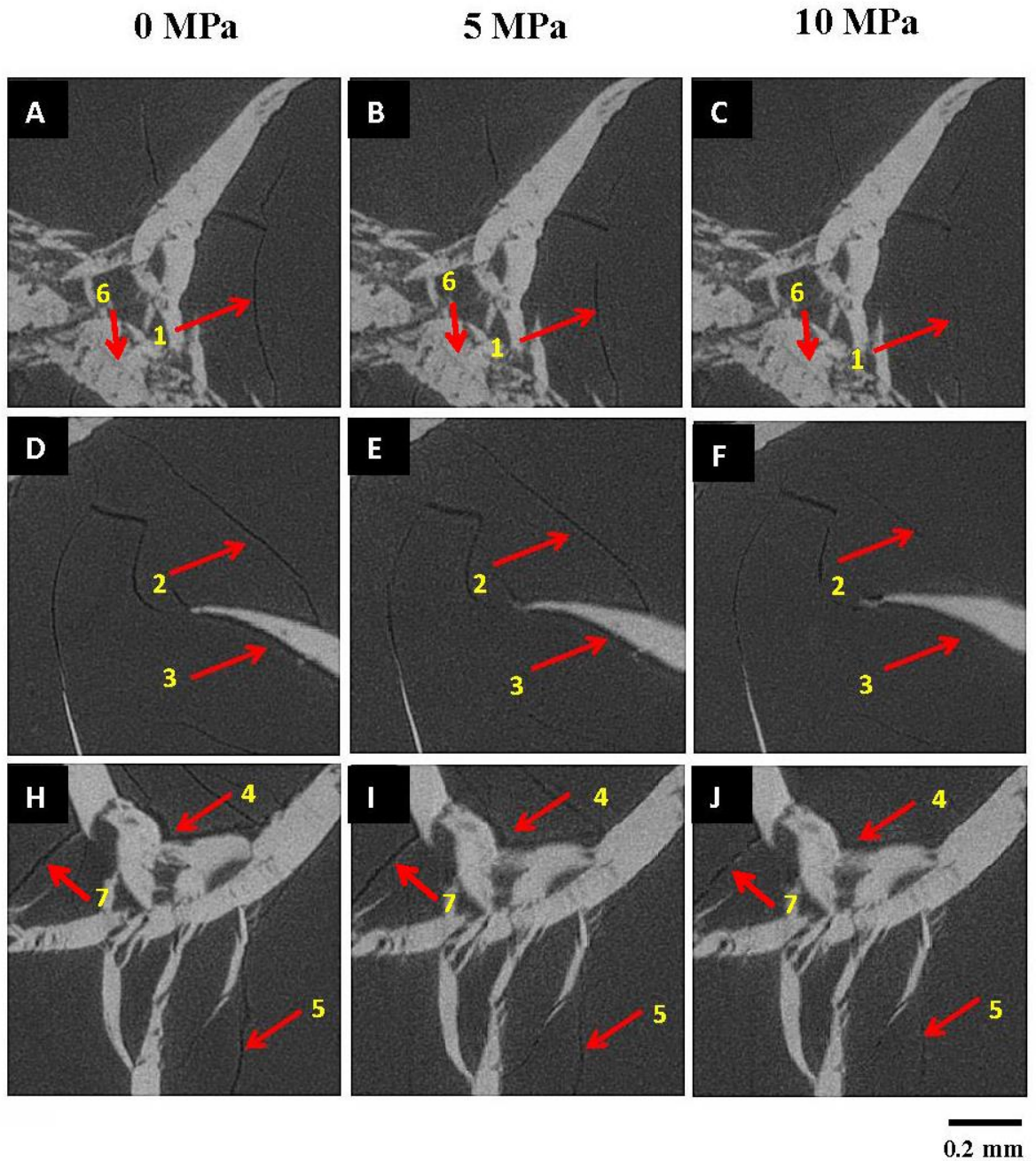
Figure 3-8. Slices through the coal plug at different effective stresses (0 MPa, 5 MPa and 10MPa), 3.43 μm nominal resolution; A-C, D-F and H-J show three different areas. The numbers and red arrows indicate cleats: cleats 1, 2, 4 and 5 became narrower; cleat 7 became disconnected; cleat 3 disappeared at high effective stress; while cleat 6 showed almost no change.

3.3.2.2 Quantitative analysis

The micro cleats porosity (volume of the segmented micro cleats divided by the total volume) as a function of effective stress was quantified on the microCT images, and it significantly decreased with increasing effective stress, by more than half at 10 MPa effective stress. Precisely, cleat porosity decreased from 0.52 %, to 0.33 % and to 0.22 % at 0 MPa, 5 MPa and 10 MPa effective stresses, respectively (Figure 3-9); however, the volume fractions of the mineral phase and the coal matrix showed no significant difference.

In the segmented images each cleat/fracture was separated and labelled. The cleat size (3D volume, μm^3) distribution was then measured as a function of effective stress (Figure 3-10). The frequency of the large micro cleats (> 10000 μm^3) decreased dramatically when effective stress increased from 0 MPa to 10 MPa; consistent with the 3D visualizations (Figure 3-9 A-C) and permeability measurements. However, the frequency of the small micro cleats (< 10000 μm^3) did not change significantly; the number of micro cleats smaller than 100 μm^3 even slightly increased. This could be due to large micro cleats becoming disconnected with increasing effective stress, which are then counted as several small micro cleats, e.g. see Figure 3-8 J or Figure 3-9 , where a large micro cleat disconnected at 10 MPa effective stress. Note that cleats propagating outside the imaged volume (i.e. the field of view, FOV) are cropped to the FOV and thus this measurement is biased towards smaller cleats/fractures.
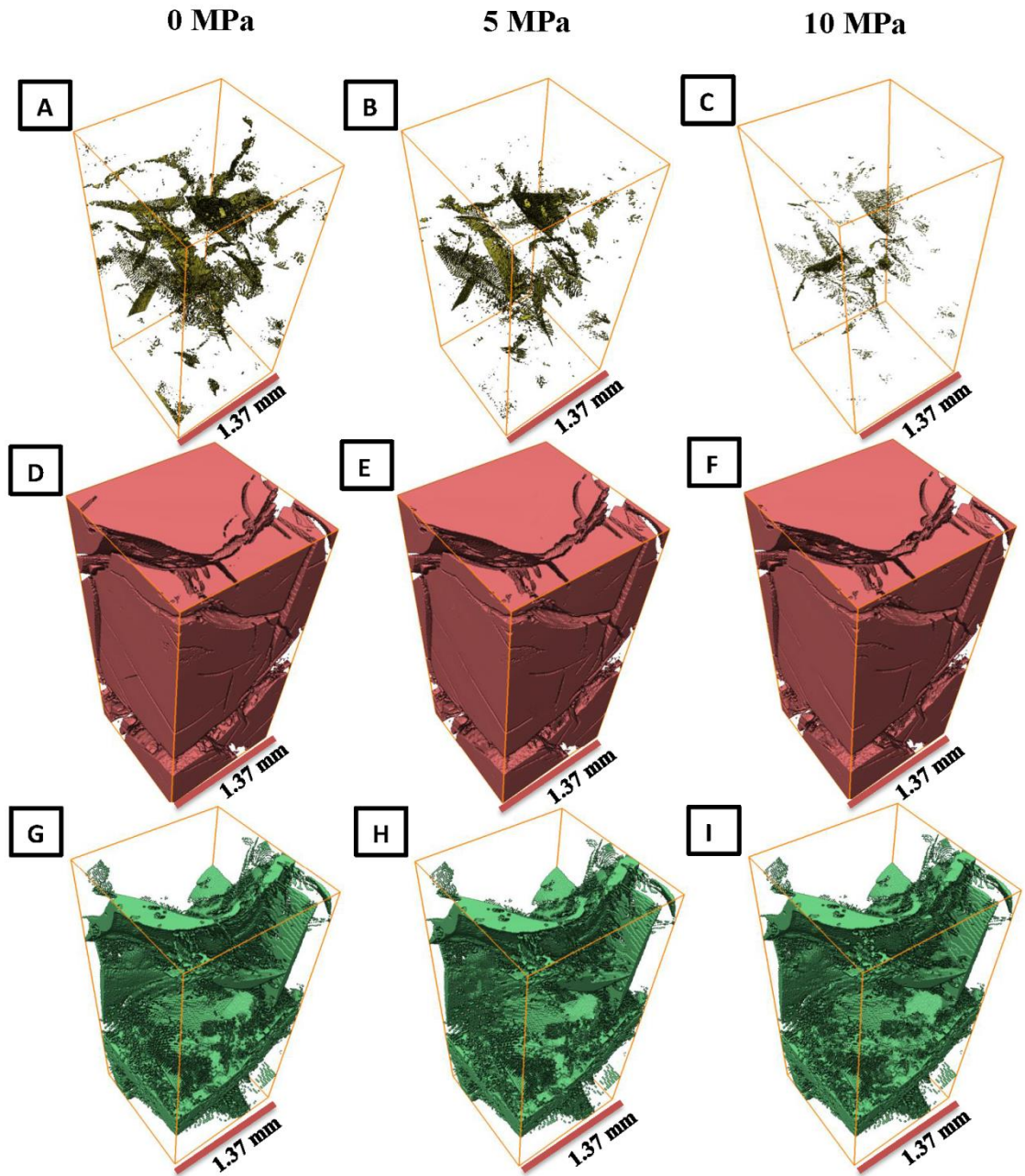
Figure 3-9. 3D visualizations of the different phases in the small coal plug at the three different effective stresses, 0 MPa, 5MPa and 10MPa (A-C, micro cleats - golden; D-F, coal matrix - red; G-I, mineral phase - green). Volumes shown are 12.2 mm^3 (400 x 400 x 884 voxels) and nominal resolution is 3.43 µm. While the coal matrix and mineral phase show no significant difference, the cleats close upon increasing effective stress.
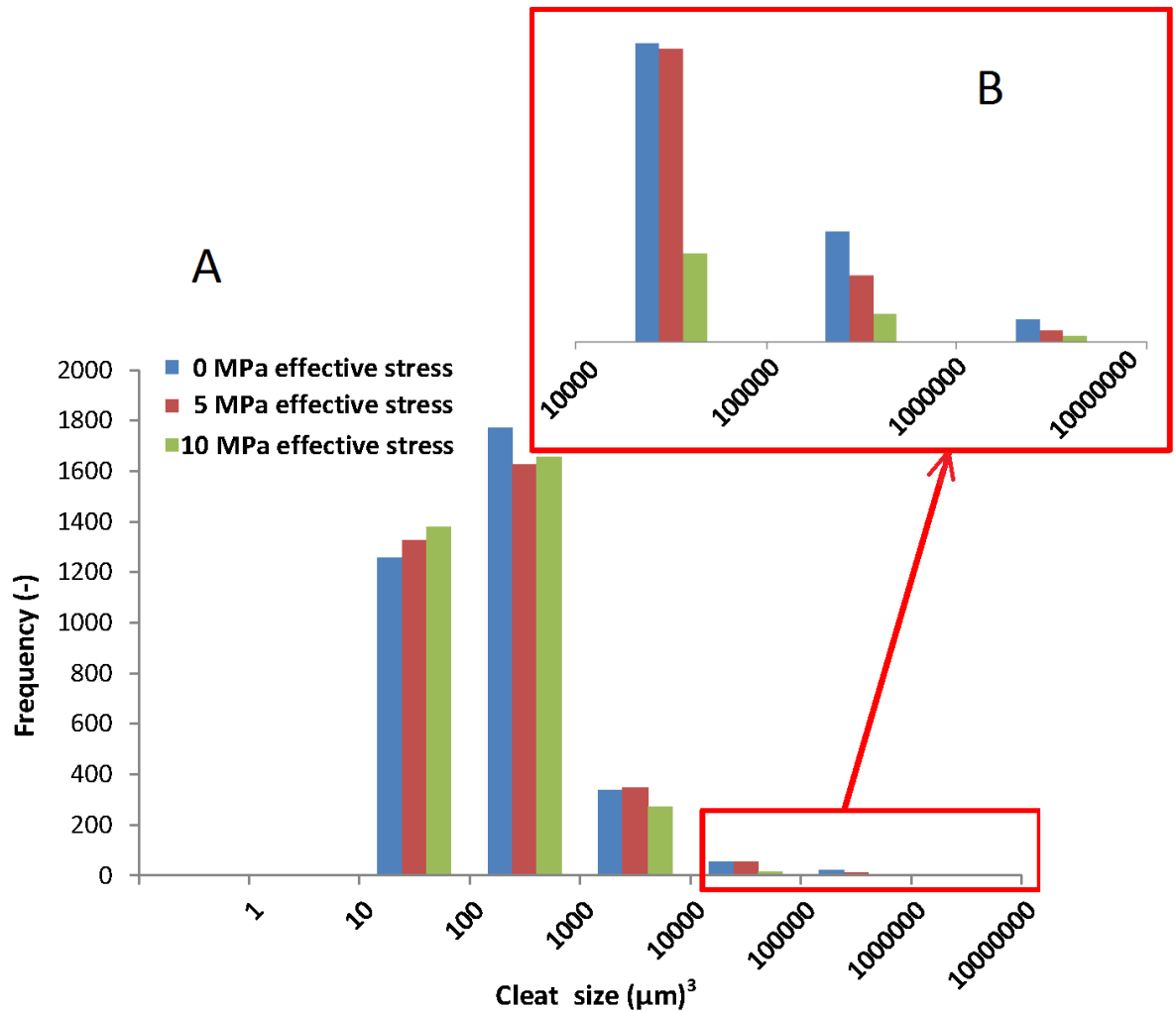
Figure 3-10. The micro cleat size distribution in the coal as a function of effective stress; (A) full spectrum; (B) zoomed-into the largest cleats area. Large cleat (> 10000 μm³) frequency dramatically decreased at 10 MPa effective stress.

3.3.3   Relation between cleat morphology, permeability and porosity

The volume fraction of the cleats measured at the two microCT resolution scales (33.7 μm and 3.43 μm voxel size) was approximately   1.02 % (0.5%   macro cleats/fractures + 0.52% micro cleats), which is significantly smaller than the gas

porosity (11.5 % ± 0.5 %) measured on the large plug. We conclude that most void space lies in the coal matrix and is of nanometer scale (i.e. always less than 3 μm, smaller than the highest microCT nominal resolution 3.43 μm), consistent with literature data (Laubach et al., 1998). This is also consistent with the linear porosity decrease with increasing effective stress (Figure 3-5), i.e. the change in cleat morphology had only a marginal influence on porosity; thus the porosity change is mainly a function of coal compressibility.

Moreover, the underlying mechanism for the rapid permeability drop also becomes clear: as effective stress increases, the cleats close and become disconnected; however, as the cleats are the major fluid conduits (Laubach et al., 1998), permeability drops dramatically, Figure 3-4, consistent with measurements on larger plugs (Liu and Rutqvist, 2010; Jasinge et al., 2011; Li et al., 2014). The residual permeability at high effective stress (> 10 MPa) is then caused by the remaining cleats in the mineral phase – these cleats are still open as coal matrix compressibility is much higher than the compressibility of the minerals.

3.4   Conclusions

Porosity and permeability are key properties in CBM / ECBM and CO_2 geo-sequestration applications. However, coal porosity and permeability are functions of the effective stress (Somerton et al., 1975; George and Barakat, 2001; Chen et al., 2011; Jasinge et al., 2011), and the relation between coal micro structure, permeability/porosity and effective stress is only poorly understood. This chapter thus imaged coal plugs at high resolution (33.7 um and 3.43 μm voxel size) with an

x-ray micro-computed tomograph in 3D as a function of effective stress (0 MPa, 5 MPa, 10 MPa) to measure the coal micro - structure.

Three phases were identified: cleats (void), coal matrix and mineral phase. Micro cleats closed upon increased effective stress, and the related cleat void space shrank from 0.52 % to 0.22 % when effective stress increased from 0 to 10 MPa. These morphological results are consistent with the gas porosity-permeability tests: gas permeability dropped dramatically (with increasing effective stress), while porosity dropped only linearly.

It concludes that effective stress causes closure of micro cleats in the coal, which leads to a drastic drop in permeability, but only a moderate drop in porosity as most void space is located in the coal matrix as nanopores.

Chapter 4   MicroCT in-situ water injection into coal

Note that this chapter has published as a journal paper:

Abstract

Porosity and permeability of deep unmineable coal seams are key parameters in the context of (enhanced) coalbed methane recovery and CO_2 geo-storage in coal beds as they determine productivity and injection rate. Porosity and permeability are again determined by the micro-structure of the coal, and the cleat network-coal matrix system. Furthermore, it is well established that swelling of the coal matrix due to water adsorption can significantly reduce permeability. However, the exact effect of swelling due to water adsorption on the coal micro-structure is only poorly understood, and how this microstructural change impacts on the permeability and porosity characteristics of the coal. This chapter thus imaged dry coal plugs and swollen coal plugs (swollen due to brine adsorption) at high resolution $(3.43 \ \mu m)^3$ in 3D with an X-ray micro-computed tomograph (microCT). On the microCT images two types of cleats were identified; cleats in the coal matrix and cleats syngeneic with the mineral phase. Approximately 80% of the coal matrix cleats closed upon water adsorption, while the cleats in the mineral phase were not affected. This cleat

closure by water adsorption dramatically reduced porosity and particularly permeability, consistent with dynamic permeability core-flood measurements.

Keywords

coal; swelling; cleat; microCT; porosity; permeability

4.1 Introduction

Coalbed methane recovery (CBM) has gained substantial interest in recent years. Essentially CBM is a method to produce natural gas from deep unmineable coal seams, and it utilizes pressure-driven fluid flow for hydrocarbon recovery, often in combination with hydraulic fracturing (Holditch et al., 1988) or N_2/CO_2 injection for enhanced production (ECBM) (Reeves 2001; Reeves et al., 2004). However, the coal permeability is dramatically reduced by several orders of magnitude (Pekot and Reeves 2003; Shi and Durucan 2005a) due to water (Charrière and Behra 2010, Walker et al., 1988) or gas (Reeves 2004; Shi and Durucan 2005a) adsorption, which cause coal swelling and seriously limits the application of this technology (Reeves 2004). Water adsorption, on which we focus here, has also been suggested to decrease the sorption capacity of CO_2 / CH_4 / N_2 in CBM/ECBM and storage volume for CO_2 geo-sequestration (Krooss et al., 2002; Ozdemir and Schroeder 2009) Water encroachment and associated water adsorption, however, is natural during CBM / ECBM and CO_2 storage in coal seams (Stevens et al. 1998).

To address these issues and to predict CBM production, several coal swelling – permeability models were built, and the swelling characteristics are typically simulated by coal matrix strain change (e.g. Day et al., 2008; Vandamme et al., 2010). However, these models failed to explain stress controlled swelling laboratory test results (Liu et al., 2011) and thus newer strain model (Peng et al., 2014) have been tuned to match the laboratory results. These models, however, still have significant limitations with respect to predicting the effect of water swelling on porosity and permeability. Specifically, these models treat the swelling effect as independent of the fracture system, i.e. the cleats are fixed or only change due to effective stress changes; while it has been suggested that swelling may close the cleats and thus reduce permeability (Larsen 2004; Saikat Mazumder et al., 2006; Pan and Connell, 2007).

Thus to fully understand the cleat system is of vital importance. Note that typically macro cleats and micro cleats (< 20 μm), on which we focus here, are distinguished. Such micro cleats have been analysed with medical x-ray computed tomography (medicalCT) (e.g. S Mazumder et al., 2006, Montemagno and Pyrak-Nolte 1995)) and SEM (e.g. (Huggins et al., 1980, Kutchko et al., 2013, Ramandi et al., 2016, Ye et al. 2013)). However, medicalCT has a relatively low resolution (~500 μm)3 (Cnudde et al., 2006) and the coal microstructure (i.e. micro cleat system) cannot be resolved; while SEM only produces 2D information of the sample surface, and that usually at vacuum conditions. The detailed 3D morphological characteristics are, however, vital as 2D space has significantly different fluid mechanical properties (e.g. the percolation threshold is much lower in 3D than in 2D, Stauffer 1979. More recently, x-ray micro-computed tomography (microCT) – which has a significantly higher resolution than medicalCT - has been increasingly used in petrophysical

studies (e.g. compare the reviews by Blunt et al., 2013, Wildenschild and Sheppard 2013 or Cnudde and Boone 2013 or for example (Iglauer et al., 2011; Iglauer et al. 2013), and the micro structure of coal was imaged (e.g. Ramandi et al., 2016; Yu et al., 2012; Pant et al., 2015). However, there is a serious lack of information regarding the effects of water swelling on the microstructure. It thus now expanded on this microCT analysis and investigated how water swelling influences the 3D morphology of coal at the micro-meter level.

4.2 Experimental Methodology

4.2.1 Materials

A coal block was acquired from a depth of 750m in the Pingdingshan Ten coal mine, Henan Province of China. The coal was a typical sub-bituminous coal (medium rank) with carbon content 54($\pm$ 2) % and volatile matter content 36($\pm$ 1) %, measured by Chinese Standards GB/T 212-2008 and DL/T 1030-2006. Stripes of white minerals were identified visually with sporadic distribution on the coal sample surface. Small samples were cut from adjacent positions from the block, and subjected to SEM and EDS analysis, Fig. 1. The coal had a relatively high oxygen content (~30 wt%; cp. points A and D in Fig. 1); the minerals were identified as $CaCO_3$ (cp. points B and C in Figure 4-1). Furthermore, a small dry coal plug (5mm diameter, 10 mm length) was cut, again from the same block and a position adjacent to the other samples, and this plug (Sample A) was imaged with an x-ray micro-computed tomography (Xradia Versa-XRM) at a high resolution of $(3.43 \ \mu m)^3$. X-ray accelerating voltage was chosen as 40 kV, the x-ray beam size was approximately 0.3 μm, and a 1000 x 1000

pixel detector was used for radiograph acquisition Total time for 3D imaging of the sample was ~ 4 hours.
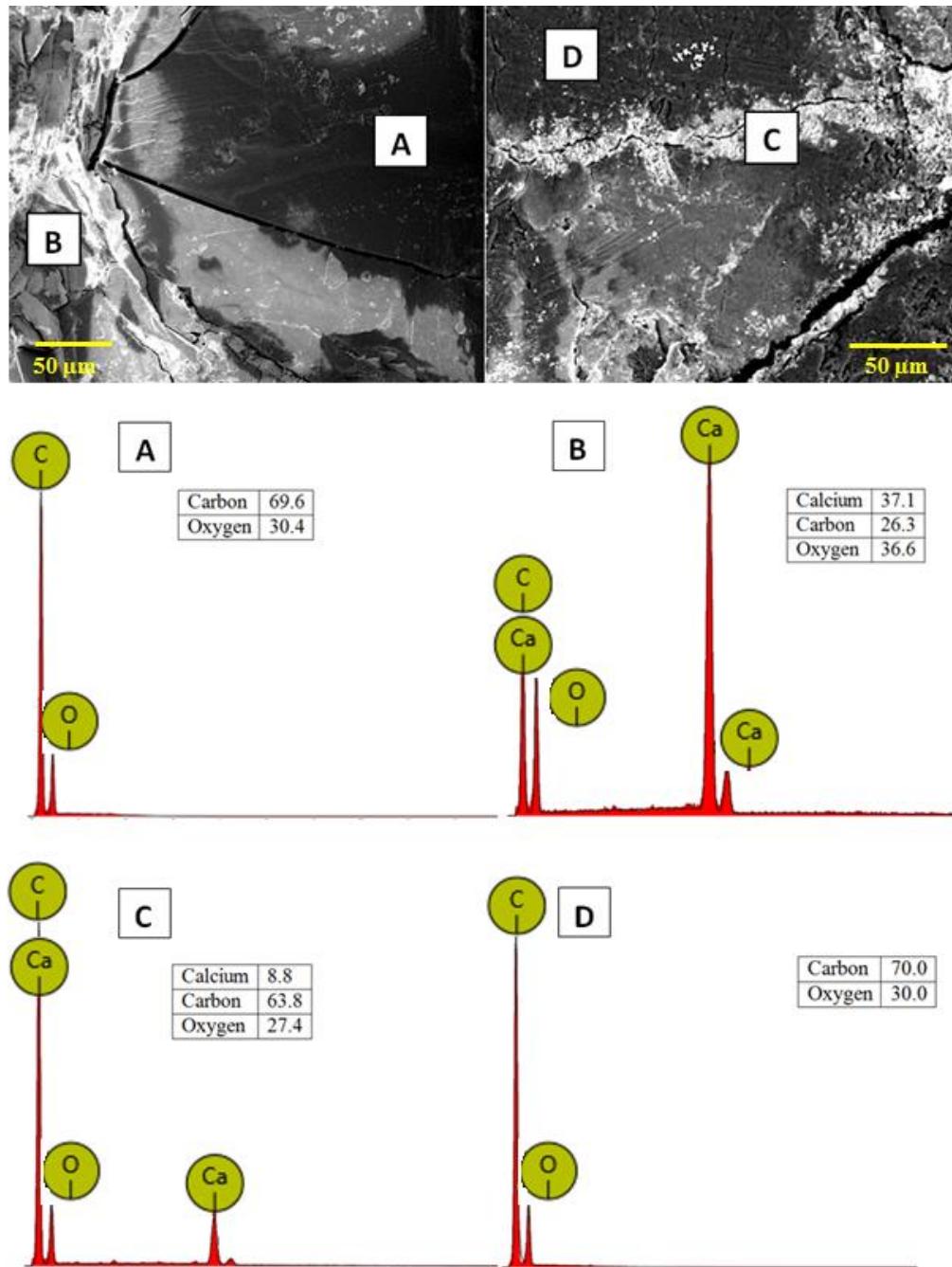
Figure 4-1 SEM images of the coal sample with elemental compositions (wt % measured by EDS) for different points A, B, C and D indicated.

4.2.2 Permeability measurements and image processing

An experimental core flood apparatus was built for gas and brine permeability measurements (Figure 4-2). The small coal plug was mounted into an X-ray transparent flow cell, and the whole apparatus was vacuumed for 12 hours to ensure that there is no air inside the plug sample or the tube system. A confining pressure of 5 MPa was applied, and subsequently more than 7000 pore volumes (PV) of brine (5 wt% NaCl in deionized water, which did not show the X-ray density during the CT scanning, is different with former studies using NaCI, e.g. Rahman et al, 2016) were injected at a flow rate of 0.02 mL/min through the plug with a high precision syringe pump (Teledyne ISCO 500D) at 296 K; and the pressure drop across the plug was continuously measured with high accuracy pressure sensors (Keller PAA-33X, accuracy 0.1%). Permeability was then calculated using Darcy's law. This test was repeated thrice to test repeatability; all the three samples (Sample A, Sample B and Sample C) were cut from the same coal block.
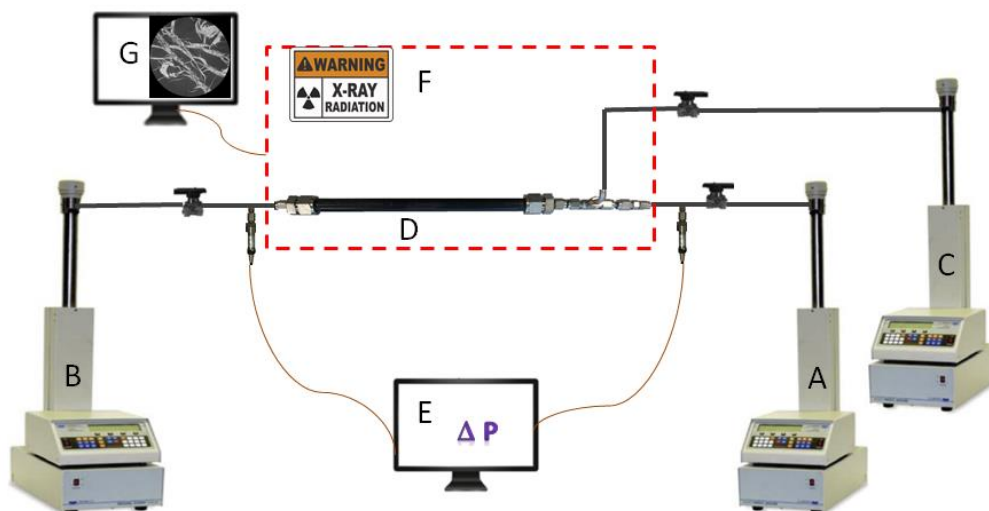
Figure 4-2 Experimental apparatus used; (A) injection pump, (B) production pump, (C) confining pressure pump, (D) core holder, (E) pressure data acquisition, (F) microCT, (G) microCT images processing.

Injection was stopped after ~120 hours flooding time (when the permeability reduced by > 80%, Figure 4-12), and the brine saturated plug was microCT imaged again at the same high resolution (without confining stress). . Note that the plug was mechanically fixed inside the microCT cell; thus the same sample volume was imaged. All microCT images were filtered with a non-local means filter (Buades et al. 2005) and segmented with a watershed algorithm (Roerdink and Meijster 2000) (Schlüter et al., 2014) Figure 4-3.

0.2 mm
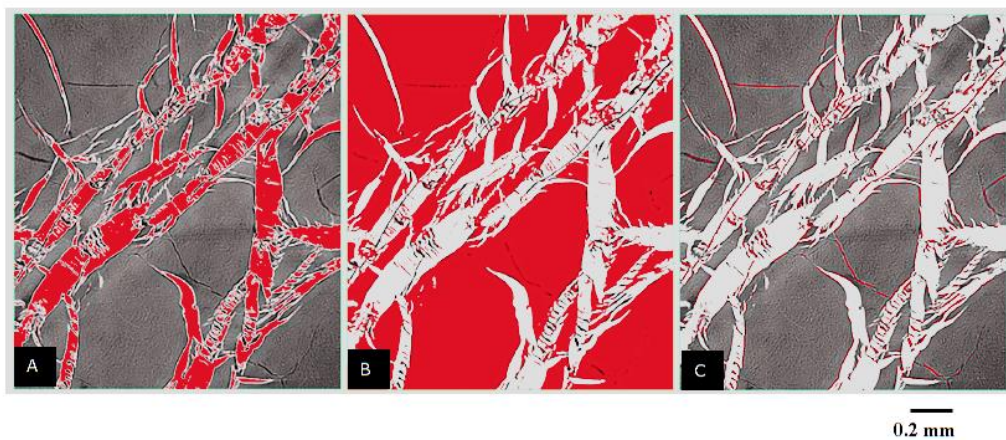
Figure 4-3 Axial slices through the segmented microCT coal sample image: (A) calcium carbonate minerals (red), (B) coal matrix (red), (C) micro cleats (red).

4.3 Results and Discussion

4.3.1 Microstructure characteristics and segmented phases

Three phases were clearly identified in the raw and segmented 2D/3D microCT images: micro cleats (black), coal matrix (grey) and minerals (white) in raw images (Figure 4-4); with white, blue and red in the segmented images (Figure 4-5). The widths of the micro cleats in the dry plug were 5-10 µm (no confining stress), while lengths up to 2 mm were measured. These micro-cleats can be divided into two groups according to their location in the sample: they can be a) in the coal matrix (e.g. A in Figure 4-4or A in Figure 4-1) or b) in the mineral phase (e.g. B in Figure 4-4 or C in Figure 4-1). Cleary, the coal sample's microstructure is highly heterogeneous.
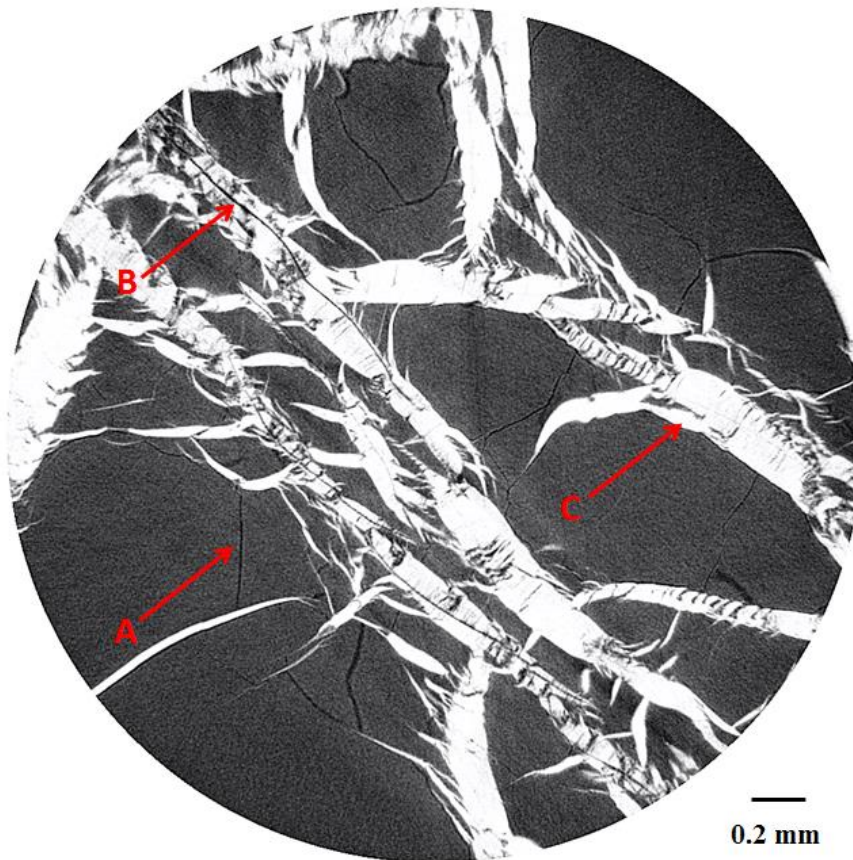
Figure 4-4 Axial 2D slice through the dry coal (3.43 µm resolution; raw image); the different features can be clearly identified: (A) micro cleat in the coal matrix, (B) cleat inside mineral, (C) mineral phase.
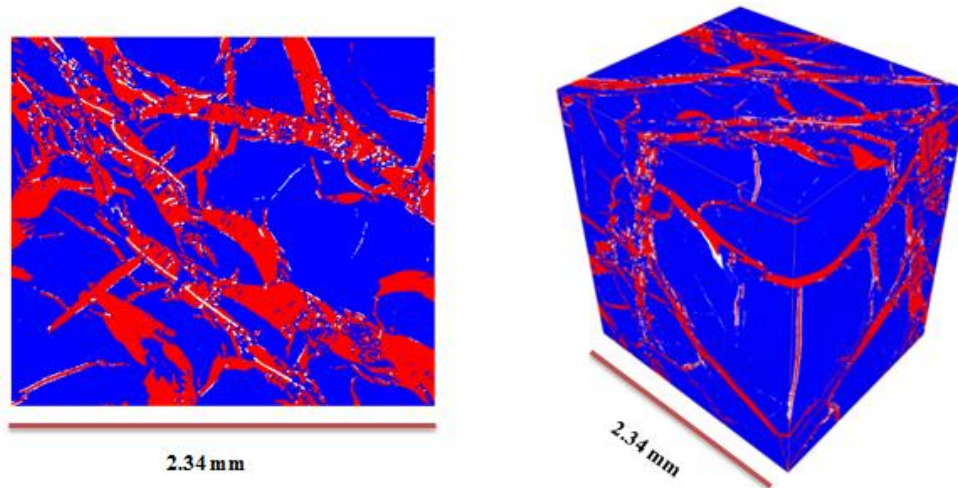
Figure 4-5 2D and 3D views of the segmented coal sample; three phases were identified: micro cleats (white); mineral phase (red); and coal matrix (blue).

4.3.2 Microstructure evolution due to swelling

4.3.2.1 Qualitative analysis

A clear change in the micro-structure was observed on the microCT images before and after swelling (Figure 4-6). Essentially the cleats in the coal matrix disappeared after the sample was saturated with brine. However, no significant change was observed in terms of the mineral phase and the cleats inside the mineral phase. In this context the concept of "internal swelling stress" was proposed (Liu and Rutqvist 2010); essentially, the coal "internal swelling stress" closed the cleats; at the same time, the mineral phase had no such "internal swelling stress" and it is less compressible, thus the open cleats were protected from closure by the mineral phase.

The micro cleats and generally the pore volume decreased significantly when the sample was saturated, this is clearer in the segmented images (Figure 4-7). All these evidence indicat that water adsorption into the coal matrix and associated coal matrix swelling.
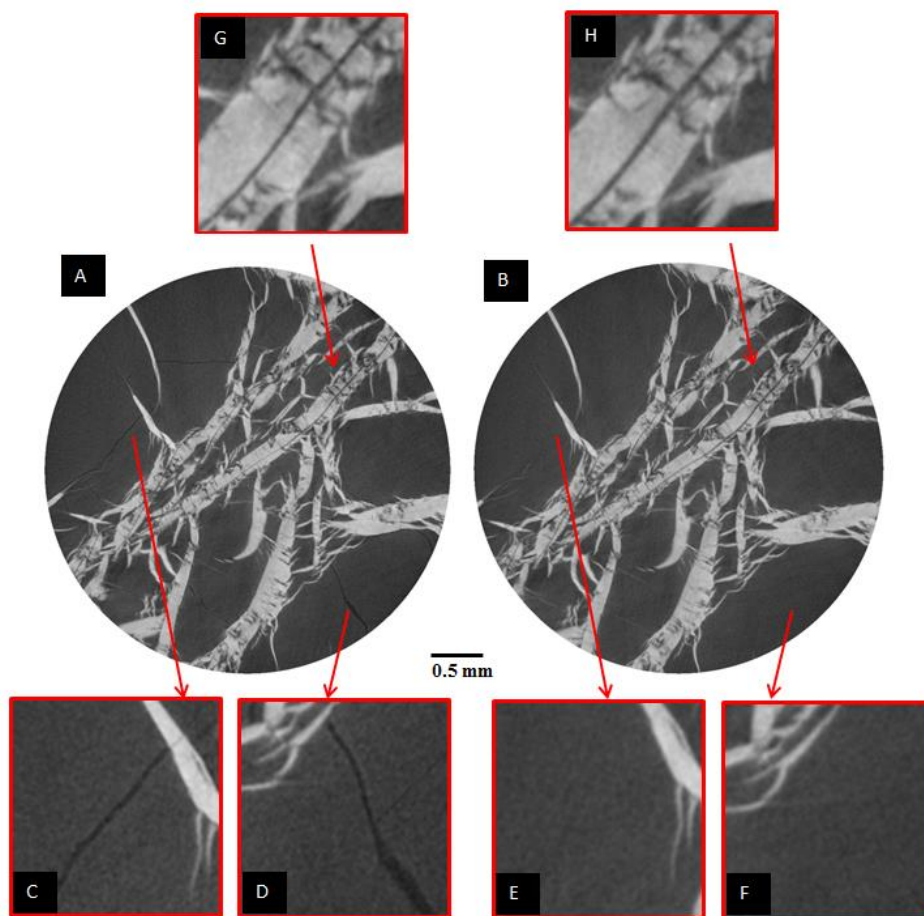
Figure 4-6 Axial 2D image slices through the coal plug (raw image); (A) dry sample, (B) brine saturated sample (same slice), (C and D) zoomed-into image A: the cleats and minerals can be seen clearly, (E and F) the sample area as shown in C and D: the cleats disappeared but the mineral phase did not change, (G and H) the cleats inside minerals showed no change before and after brine saturation.
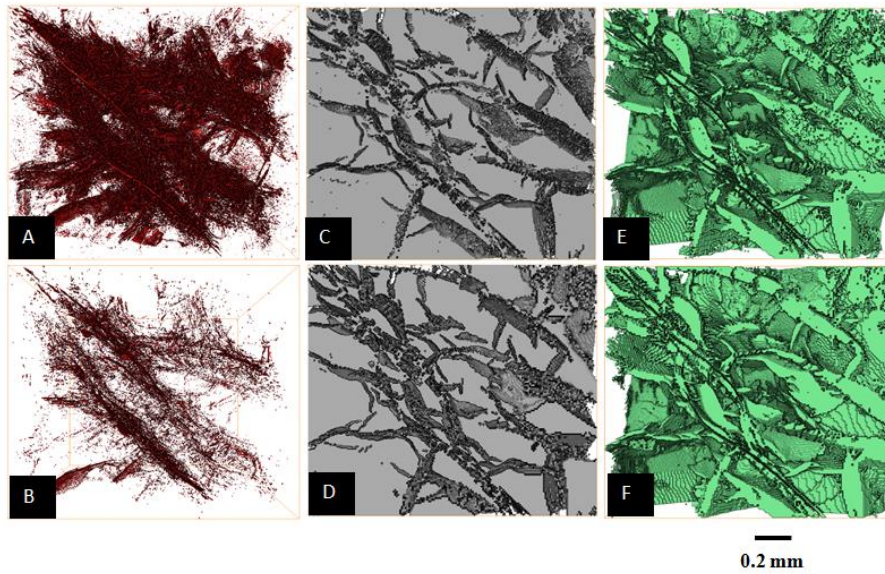
Figure 4-7 3D images of the three segmented phases; (A) micro cleats, dry plug; (B) micro cleats, brine saturated plug; (C) coal matrix (shown in grey), dry plug; (D) coal matrix, brine saturated plug; (E) mineral phase, dry plug; (F) mineral phase, saturated plug.

4.3.2.2 Quantitative analysis

The microCT images were further analysed and the volume fractions of the different phases were measured before and after brine saturation. The micro cleat volume shrank significantly (by ~ 75%) due to brine saturation, while the coal matrix volume increased by the same nominal amount, but the mineral fraction volume stayed approximately constant, Table 4-1.

Table 4-1 Volume fractions of the different phases in the coal plug measured on the micro-CT images.

	Dry plug	Saturated plug
Micro cleats total (%)	2.85 %	0.71 %
Micro cleats – Below threshold size (%)[*]	1.20 %	0.19 %
Micro cleats – Above threshold size (%)[*]	1.65 %	0.52 %
Minerals (%)	28.79 %	28.83 %
Coal matrix (%)	68.36 %	70.46 %
Effective cleat porosity[*]	1.19 %	0.19 %

[*]Cross-sectional threshold value = 50000 μm^2.

The 3D topographies (A and B in Figure 4-8) illustrate how the micro cleats changed due to brine saturation. The cross sectional area (μm^2) was chose as the threshold value which is better description for the morphology of cleats (thin and long) than the volume (μm^3) value, We further divided small micro cleats (C and D in Figure 4-7; all void cross-sectional areas $\sim$ 50000 μm^2) and larger micro cleats (E and F in Figure 4-9) for better visualization; all void space significantly shrank due to brine saturation, furthermore almost all larger micro cleats were oriented vertically where along the coal bed. The absolute porosity (ϕ) for each image slice was computed, and ϕ was clearly reduced by swelling throughout the plug (Figure 4-9). We further analysed the effective porosity (ϕe); ϕe also dramatically decreased (from 1.19 % to 0.19 %).This is consistent with our pore size distribution measurements on the microCT images: all micro-cleats shrank, particularly the larger ones (Figure 4-10).

Finally we extracted a pore network for the dry and brine saturated plug with a skeletonization algorithm (Liang et al., 2000), Figure 4-11; clearly the number of fluid conduits was significantly reduced by brine saturation.
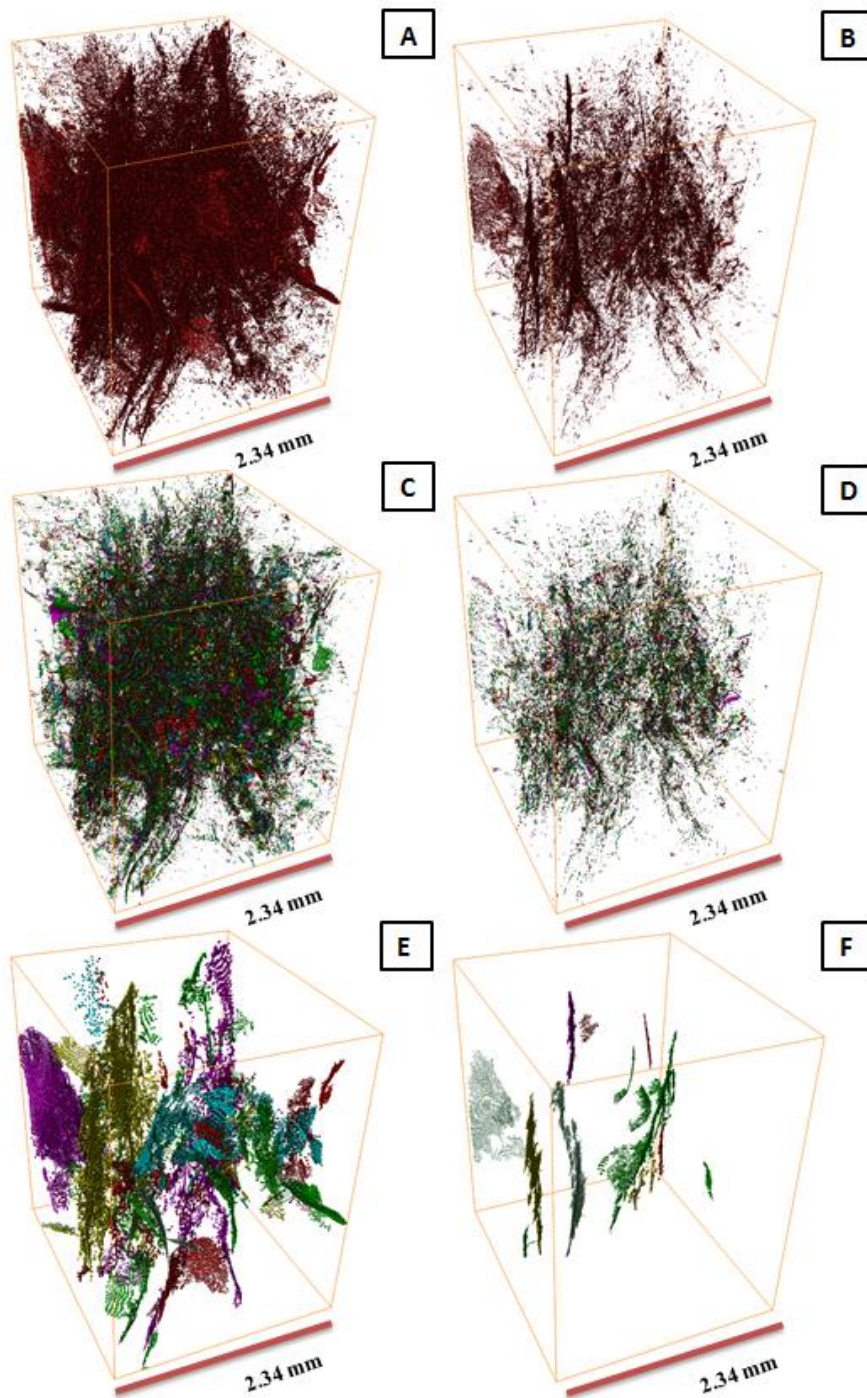
Figure 4-8 3D visualization of the micro cleat system before (left) and after (right) brine saturation; a threshold value of 50000 μm^2 was set for the cleat cross-sectional

area to distinguish smaller and larger cleats; (A) micro cleats, dry sample; (B) micro cleats, brine saturated plug; (C) micro cleats ($\leq 50000 \ \mu m^2$), dry sample; (D) micro cleats ($\leq 50000 \ \mu m^2$), saturated plug; (E) micro cleats ($> 50000 \ \mu m^2$), dry sample; (F) micro cleats ($> 50000 \ \mu m^2$), saturated plug.
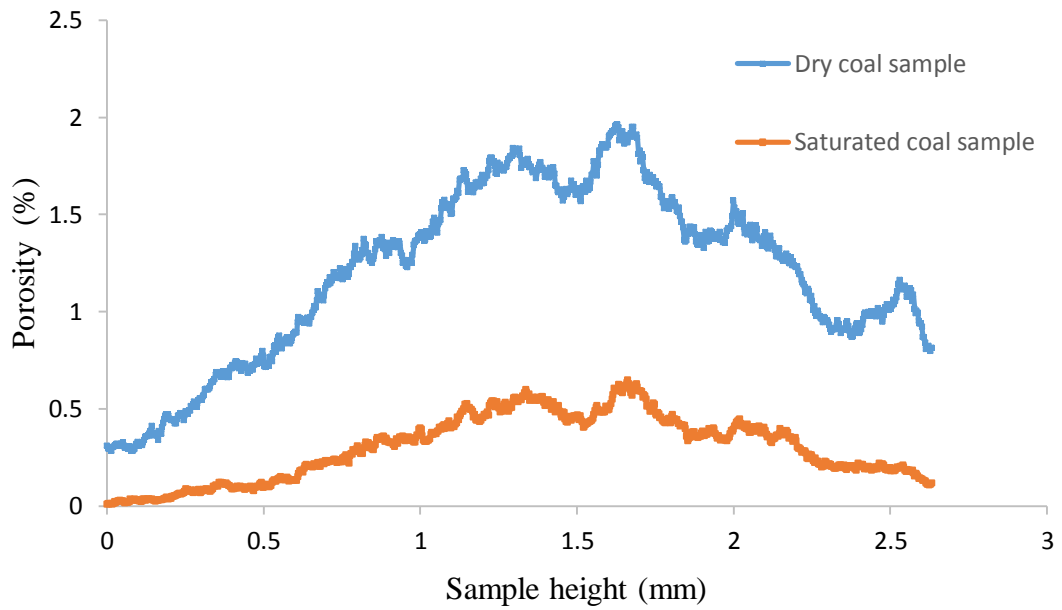
Figure 4-9 Porosity versus sample height.
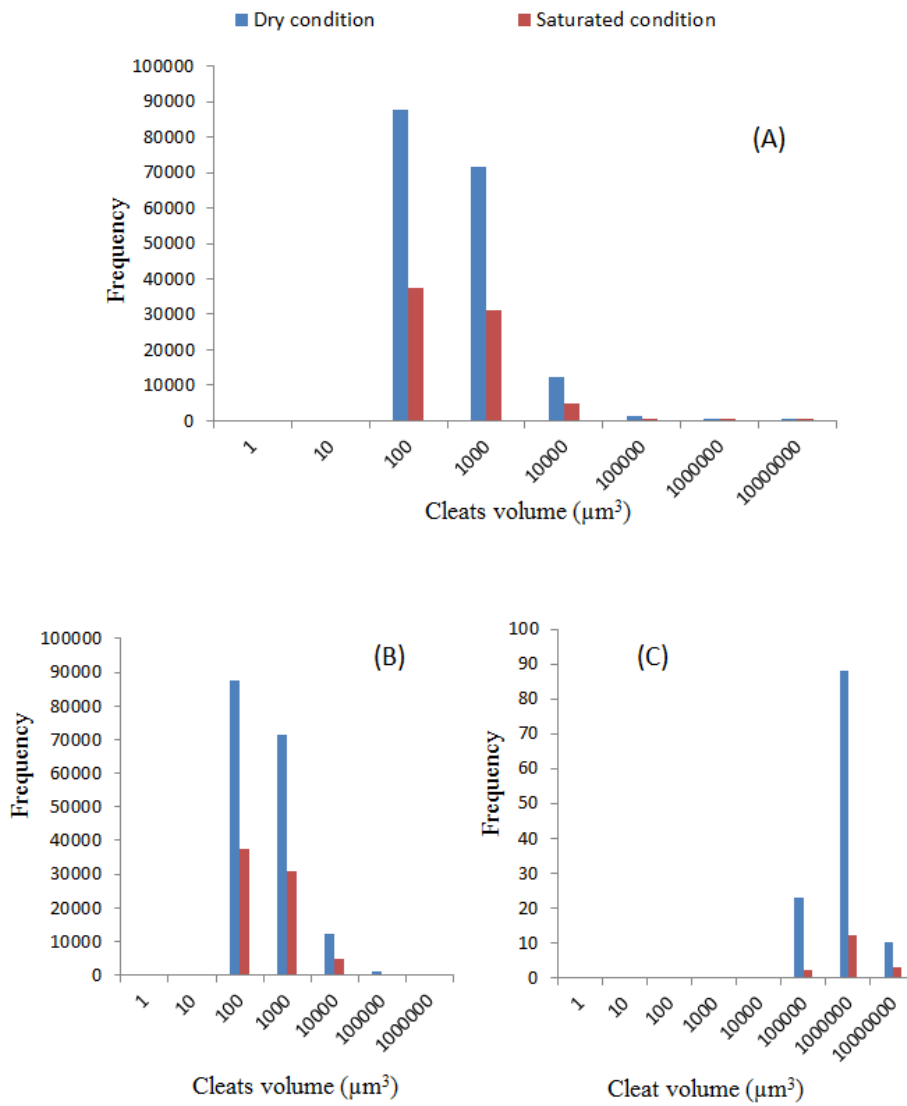
Figure 4-10 Cleat size distributions before and after swelling (caused by brine saturation); (a) all cleats; (b) cleats ≤ 50000 μm^2; (c) cleats > 50000 μm^2. 50000 μm^2 is the threshold value of cross-sectional void area.
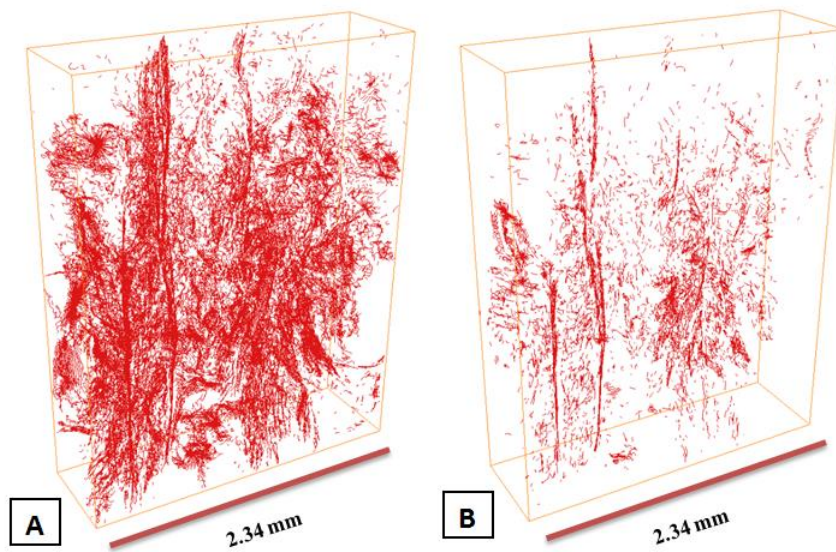
Figure 4-11 Pore networks extracted by skeletonization algorithm (Liang et al. 2000), no confining stress; (A) dry coal sample; (B) brine saturated coal sample.

4.3.3 Permeability evolution

The dynamic permeability during brine injection was measured on three separate plugs (Sample A, B and C), see above in the methodology section. Permeability consistently dropped rapidly in the first 60 hours of the experiment (~ 3700 PV of brine injected), Figure 4-12. This permeability drop can be fitted with logarithmic curves (printed onto the graphs in Figure 4-12). However, the plugs had significantly different absolute permeabilities; which is expected as coal is a rather heterogeneous material (cp. section 3.1). The graphs were quite similar though, all samples underwent a >80% permeability loss after injection of ~ 7300 PV of brine. This permeability drop is consistent with the microCT analysis above: porosity significantly reduced during the water adsorption process (from 2.85% to 0.81%);

and permeability loss was caused by closure of 80% of the micro cleats (cp. Figure 4-11), which was induced by coal matrix swelling.
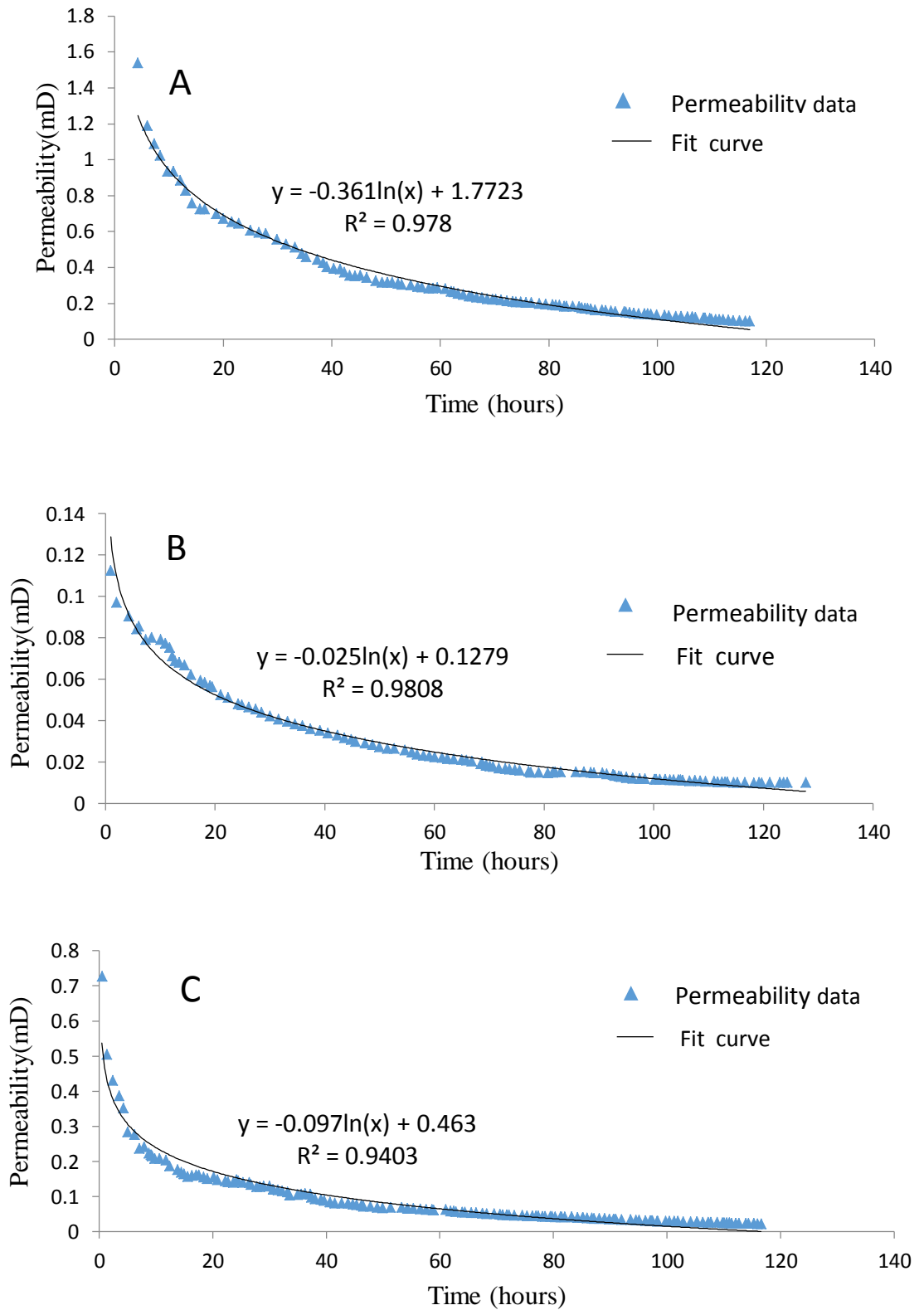
Figure 4-12 Dynamic permeability versus brine injection time for the three coal samples tested (confining stress = 5 MPa), brine was injected at a flow rate of 0.02 mL/min (i.e. 100h correspond to ~6200 PV of brine injected); A for sample A, B for sample B and C for sample C.

4.4   Conclusions

Coal porosity and permeability are key parameters as they control natural gas production from deep (unmineable) coal seams (Gale and Freund 2001; Creech and McConachie 2014; Sharma et al., 2013). However, the microstructure of the coal – which ultimately determines coal porosity and permeability – is only poorly understood. This is especially true for the effect of swelling on the microstructure (e.g. Syed et al., 2013)– which is a well-known cause for permeability change (e.g. (Saikat Mazumder et al., 2006))

Thus dry and swollen (due to brine adsorption) coal plugs were imaged with 3D microCT at a high voxel resolution (3.4 μm)^3. The dry images were similar to those acquired by (Pant et al., 2015) and (Ramandi et al., 2016); and the medium rank coal was highly heterogenous and had a low porosity (2.85 % ± 1%) and permeability (~0.1 mD -10 mD) and a significant mineral content. Micro cleats were visible in the coal matrix and the mineral phase, consistent with SEM imaging (cp. Figure 4-1). However, when brine was injected into a dry coal plug, more than 80% of these cleats closed due to swelling, which caused a dramatic reduction in porosity and particularly permeability. But the cleats in the mineral phase were still open after the coal matrix swelling; this could be explained by the lower internal stress in the mineral and the lower compressibility of the mineral.

It concludes that water adsorption into dry coal causes significant swelling effects. This swelling drastically alters the microstructure of the coal; which again drastically reduces coal permeability.

Chapter 5   MicroCT in-situ supercritical CO2 injection into coal

Note that this chapter has published as a journal paper:

Abstract

Enhanced coalbed methane recovery and CO$_2$ geo-storage in coal seams are severely limited by permeability decrease caused by CO$_2$ injection and associated coal matrix swelling. Typically it is assumed that matrix swelling leads to coal cleat closure and as a consequence, permeability is reduced. However, this assumption has not yet been directly observed. Using a novel in-situ reservoir condition x-ray micro computed tomography flooding apparatus, for the first time we observed such micro cleat closure induced by supercritical CO$_2$ flooding in-situ. Furthermore, fracturing of the mineral phase (embedded in the coal) was observed; this fracturing was induced by the internal swelling stress. It concludes that coal permeability is drastically reduced by cleat closure, which again is caused by coal matrix swelling; which again is caused by flooding with supercritical CO$_2$.

5.1   Introduction

CO$_2$-enhanced coalbed methane recovery (ECBM), especially in combination with carbon geo-sequestration (CGS) in deep unmineable coal seams has received

considerable interest in recent years (e.g. Shi and Durucan, 2005a; Shi and Durucan, 2005b; Kaveh et al., 2011; Chen et al., 2012; Syed et al., 2013). Technically, CO_2 is injected into the coal seams and it adsorbs onto the coal surface in micro pores and fractures thereby displacing methane (Zhang et al., 2011; Moore, 2012). However, the coal matrix swells when CO_2 is injected (Reucroft and Patel, 1986; Karacan, 2003; Izadi et al., 2011; Wang et al., 2011), which drastically reduces the coal permeability by orders of magnitudes (Pekot and Reeves, 2003; Shi and Durucan, 2005b) and consequently seriously limits application of this technology (Reeves, 2004). Mechanistically, it has been hypothesised that the dramatic permeability decrease is caused by cleat closure induced by coal swelling (Mazumder et al., 2006; Pan and Connell, 2007; Wu et al., 2011). However, this effect has not been directly observed yet.

Thus this chapter imaged the changes in coal microstructure caused by supercritical (sc) CO_2 injection directly in-situ via high resolution X-ray micro-computed tomography at reservoir conditions; and we observed that the coal matrix swelled significantly due to CO_2 adsorption, which led to matrix cleat closure. Interestingly new fractures were formed in the mineral phase by the internal swelling stresses in the coal matrix; however, the overall permeability drastically dropped.

5.2   Experimental procedure

A small coal plug (diameter = 5 mm, length = 10 mm) was cut from a coal block acquired from 750 m depth at the Pingdingshan Ten coal mine, Henan, China. The coal was a typical sub-bituminous (medium rank) sample and had a carbon content of 54($\pm$ 2.0) % and a volatile matter content of 36($\pm$ 1.0) % measured by Chinese

standard GB/T 212-2008. Nitrogen porosity and permeability (10.0 % and 0.2 mD) were measured on a separate standard sister plug (38.1 mm diameter and 76 mm length) cut from the same block at 5 MPa effective stress (6 MPa confining pressure and 1 MPa injection pressure) with an AP-608 Permeameter-Porosimeter (accuracy ± 0.1 %).

The small cylindrical coal plug was then mounted into a high pressure-high temperature (HPHT) x-ray transparent core holder, which was integrated into a HPHT microCT (Xradia VersaXRM) coreflooding apparatus (cp. Iglauer et al. 2011, Rahman et al. 2016 and Zhang et al. 2016) , Figure 5-1. The swelling experiments were then conducted following below steps:

1. The core and tubing system were vacuumed for 24 hours to ensure no air remained inside the system.

2. All flood lines, fluids and the core holder were continuously isothermally heated to 323 K [=50°C] with heat jackets and continuously circulating warm water.

3. A confining pressure of 5 MPa (effective stress = 5 MPa) was applied, and the sample was imaged at a high resolution of (3.43 µm)^3 in-situ.

4. The coal plug was then flooded with supercritical CO_2 at 10 MPa backpressure, while a confining pressure of 15 MPa was applied (i.e. the experiment was conducted at constant effective stress, 5 MPa). The scCO_2 was injected at 0.1 ml/min flow rate (viscosity of the CO_2 was 0.0326 mPa.s, Fenghour et al., 1998). The pressure drop across the coal plug was continuously measured with high accuracy pressure sensors (Keller PAA-33X, accuracy 0.1%) and dynamic permeability was calculated via Darcy's

law. Flooding was stopped after 17 hours when more than 5000 pore volumes (PV; note: 1 PV = 19.63 mm^3) of scCO$_2$ were injected.

5. The coal plug was then microCT imaged again at the same high resolution (3.43 μm)^3 in-situ at 323 K and 10 MPa pore pressure.

6. All microCT tomograms acquired were filtered with a 3D non-local means filter (Buades et al., 2005) and segmented with a watershed algorithm (Roerdink and Meijster, 2000; Schlüter et al., 2014) for the quantitative analysis.
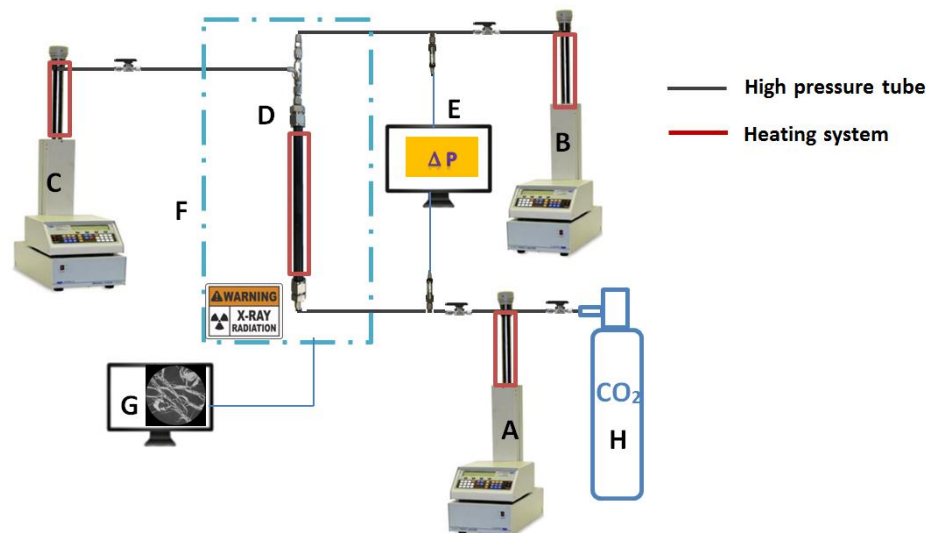
Figure 5-1 High pressure-high temperature in-situ microCT coreflooding apparatus: (A) injection pump, (B) production pump, (C) confining pressure pump, (D) core holder assembly, (E) pressure data acquisition, (F) microCT, (G) microCT image processing, (H) CO$_2$ cylinder.

5.3   Results and discussion

5.3.1   Micro cleat morphology changes and associated permeability reduction

The microstructure of the coal is visualized in Figures 5-2 and 5-3, where micro cleats are black, the mineral phase is white (the mineral phase was identified as $CaCO_3$ by SEM-EDS analysis) and the coal matrix is dark grey (Figure 2) or illustrated in colour in 3D (Figure 5-3: coal matrix is blue, mineral phase is green and micro cleats are red). The volume fractions of these phases were then measured on the segmented images (71.4 % coal matrix, 28.2 % mineral phase, and 0.4 % micro cleats), and the morphologies of the micro cleats were analysed; width ~5-10 μm and lengths up to 2 mm were measured, with an effectively random distribution in the coal matrix. The micro cleats volume percentage (0.4 %) was much smaller when compared to the total porosity (10 % nitrogen gas porosity, see above; including both cleat system and coal matrix; note that the pore structure in the matrix is nanoscale (Harpalani and Chen, 1997; Cui et al., 2004) which cannot be resolved by microCT); however, the micro cleats still controlled the permeability.

In this unconstrained condition (but at constant confining stress), the permeability rapidly and substantially decreased from 0.2 md to 0.002 md during $scCO_2$ flooding, Figure 5-4. Such a large permeability reduction is consistent with previous studies (e.g. Reeves, 2004 observed a one order magnitude permeability reduction near the wellbore in a field experiment; and Siriwardane et al., 2009 measured a 90% permeability decrease in a lab test). Now, when comparing the micro cleat morphology (Figures 5-2, 5-3) before and after $scCO_2$ flooding, a significant change is obvious. All cleats in the coal matrix closed; and as cleats are the major fluid conduits (Laubach et al., 1998) this observation is consistent with the independently measured drastic permeability drop.
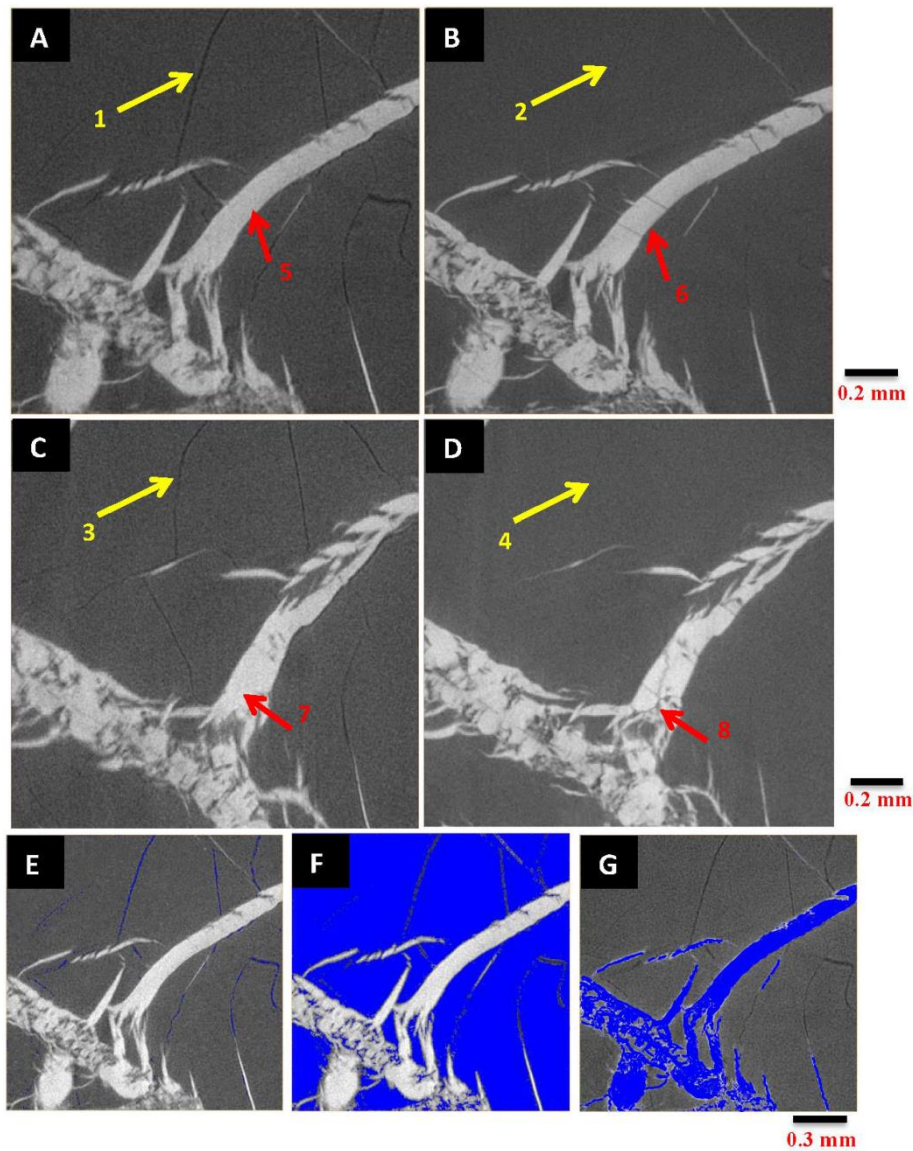
Figure 5-2 (A) image slice through the coal before scCO2 flooding (raw image); micro cleats are black, coal matrix is dark grey, and mineral phase is white; (B) image slice (same area as in A) after scCO2 injection (raw image), the cleats in the coal matrix disappeared (cp. points 1 and 2); (C) and (D) another example of coal matrix cleat closure before (C) and after (D) scCO2 injection, cp. points 3 and 4; furthermore new fractures appeared in the minerals phase after scCO2 flooding, cp. points 5 and 6, and 7 and 8; (E) micro cleats (blue), segmented image; (F) coal matrix (blue), segmented image; (G) mineral phase (blue), segmented image.
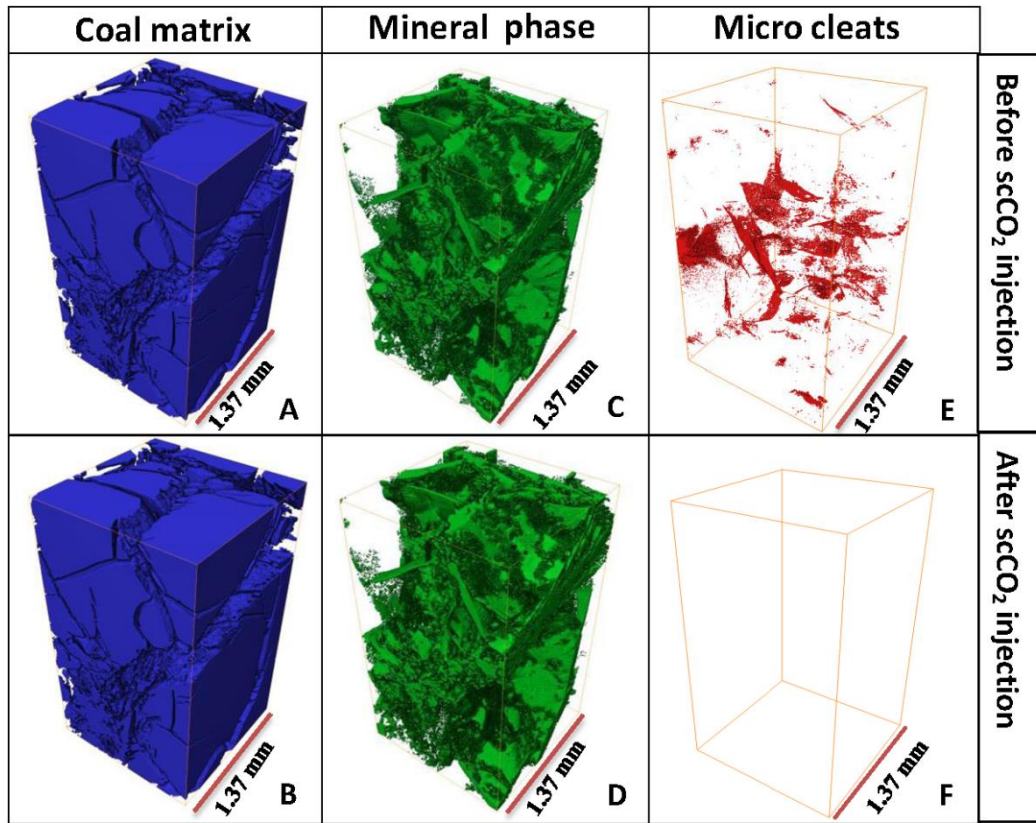
Figure 5-3 (A) and (B) 3D visualization of coal matrix (blue), before and after scCO2 injection; (C) and (D) 3D visualization of mineral phase (green), before and after scCO2 injection; (E) and (F) 3D visualization of micro cleats (red), before and after scCO2 injection. The volumes shown are 5.16 mm3 (400×400×800 voxels).
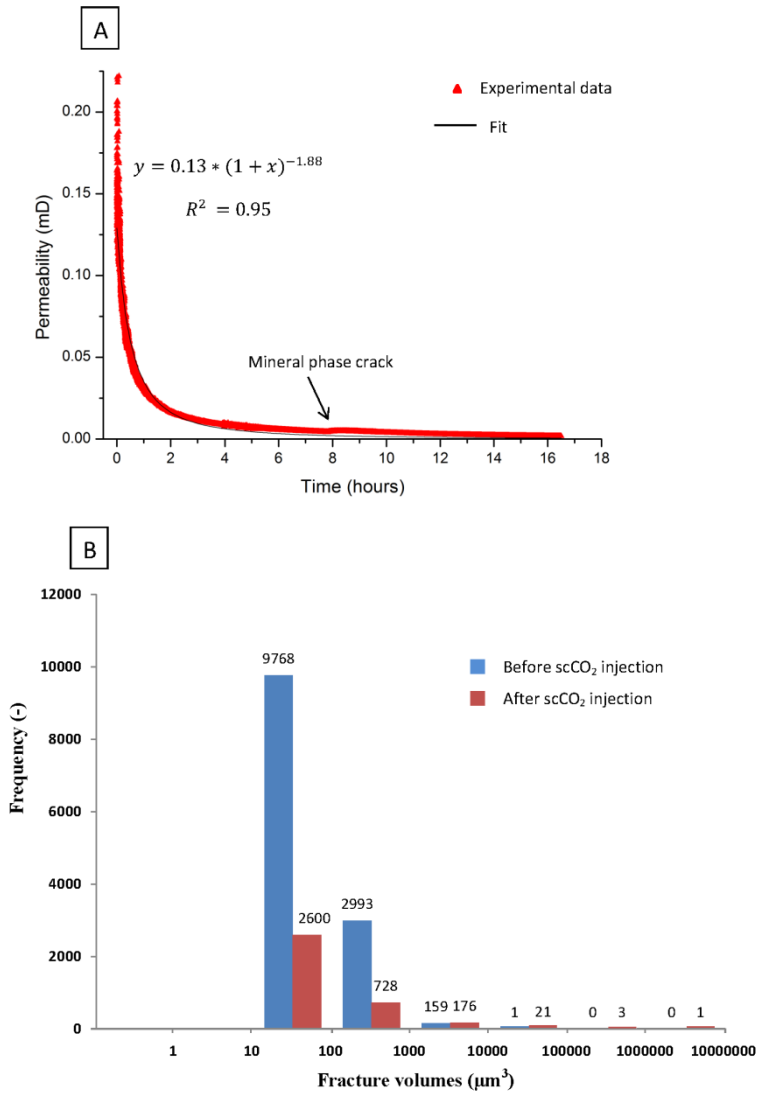
Figure 5-4 (A) Dynamic permeability measured injection time ($scCO_2$ was injected at 0.1 mL/min). (B) Fracture size distribution in mineral phase before and after $scCO_2$ injection.

5.3.2 New fractures appeared in the mineral phase

Furthermore, we observed an interesting phenomenon: new fractures appeared in the mineral phase (Figures 5-2 and 5-5, cp. also the Supporting Information). These new fractures were mainly located at the interface between coal matrix and mineral phase.

Their width was ~ 5 µm and they usually spread through the whole width of the mineral vein (length < 0.3 mm). Mechanistically these new fractures were created by the coal matrix swelling stress (the swelling stress as hypothesized by Liu and Rutqvist, 2010). This becomes clear when measuring the volume matrix strains for the phases on the microCT images, and applying the swelling stress (σs) theory, where in the particular coal matrix area is constrained during the $scCO_2$ adsorption as for the mineral phase (without swelling effect) as a boundary. Based on this analysis (details are given in the Supporting Information), we calculated an internal swelling stress in the coal matrix of 15.52 MPa. Thus the compressive stress exerted onto the mineral was above the plastic deformation limit of limestone (which for example is approximately 13 MPa for Saint Maximin limestone, Baud et al. 2009).

Furthermore these newly formed fractures in the mineral phase were likely the cause of the residual permeability in the swollen coal (cp. Figure 5-4). Indeed we observed a slight (but significant) pressure drop after ~ 8 hours injection time (Figure 5-4), and we attribute this to the formation of a new fracture in the mineral phase. However, these new fractures were typically disconnected and much shorter when compared with the cleats in the coal matrix; moreover the mineral phase was heterogeneously distributed in the coal matrix, and thus permeability was not significantly influenced by these new fractures. Note that the porosity of the mineral phase (fractures' volume fraction) increased from 1.2% to 5.6% after $scCO_2$ injection (cp. also Figure 5). We also measured the size distribution of the fractures in the mineral phase (Figure 4); the number of small fractures (less than 1000 µm^3) decreased after $scCO_2$ injection, which is probably caused by internal swelling stress compression. However, the number of larger fractures (> 1000 µm^3) increased leading to an overall porosity increase in the mineral phase, see above.

A

B

New fractures in mineral phase

0.85 mm

C

D

0.85 mm

E

F

0.85 mm

0.85 mm
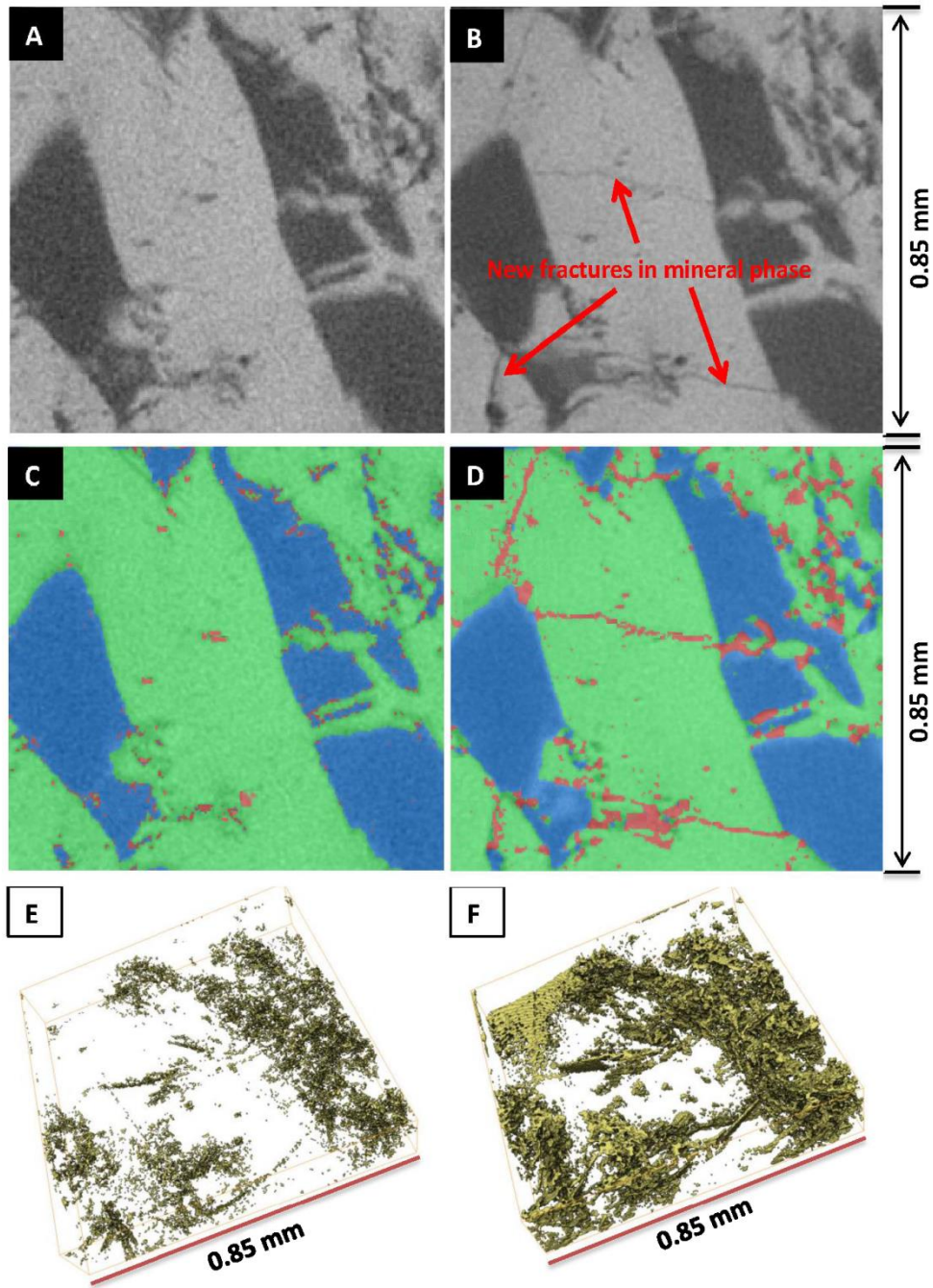
Figure 5-5 (A)-(D) image slices through coal plug; (A) before CO_2 injection (raw image); (B) after CO_2 injection (raw image); (C) and (D) segmented images (A) and (B) with fractures (red) in minerals, mineral (green), and coal matrix (blue); (E) 3D visualization of fractures in the mineral phase (same area as in A-D) before $scCO_2$ injection (E) and after $scCO_2$ injection (F). (E) and (F) show a volume of ~0.12mm3 ($250\times250\times50$ voxels).

5.4   Conclusions

Coal permeability is a key parameter, which determines the efficiency of CO_2 enhanced coalbed methane recovery and geological CO_2-sequestration in unmineable coal seams. However, a sharp drop in permeability during the CO_2 injection process (Shi and Durucan, 2005b; Larsen 2004) severely limits application of this technology (Reeves, 2004). Permeability is mainly determined by the cleat network and cleat morphology (Harpalani and Chen, 1992); however, how CO_2 adsorption changes this cleat network is poorly understood.

Thus a coal plug at reservoir conditions (15 MPa confining pressure, 5 MPa effective stress, 323 K) was imaged before and after $scCO_2$ injection in-situ with a novel HPHT microCT core flooding apparatus (Iglauer et al. 2011; Rahman et al. 2016), which can mimic near injection wellbore conditions. It has observed that all micro cleats in the coal matrix were closed due to CO_2 adsorption, consistent with the dramatic decrease in permeability (from 0.2 mD to 0.002 mD). Interestingly, new fractures were formed in the mineral phase (carbonate) by internal swelling stress (porosity of the mineral phase increased from 1.2 % to 5.6 %).

It concludes that coal matrix swelling due to CO_2 adsorption dramatically changes the morphology of the micro cleat network and thereby drastically reduces coal permeability, and such swelling induces fracturing of the mineral phase in the coal seam. Comparing to Chapter 4 - which is the brine saturation experiment, we also concluded that the scCO2 induced swelling is much stronger than the brine induced.

Chapter 6   Micro-scale fracturing mechanisms in coal induced by adsorption of supercritical CO$_2$

Note that this chapter has published as a journal paper:

Abstract

Coal bed methane production can be assisted by CO$_2$ injection. However, CO$_2$ adsorption in the coal matrix leads to a dramatic reduction in permeability and an associated change in microstructure caused by coal matrix swelling. Furthermore, it has been recently observed that the induced swelling stress fractures the unswelling (mineral) phase in laboratory investigations. However, the failure mechanisms are still not understood, and the way internal swelling stresses are generated is not clear. Thus, in this chapter, it proposes a new method which combines x-ray microtomography imaging, nanoindentation testing and DEM modeling with which we can predict the rock mechanical performance at micro scale. Indeed such swelling processes inside a coal sample were successfully simulated, including a simulation of the fracture mechanism of the mineral phase, and a quantification of the in-situ von Mises stresses generated by swelling. It concludes that the proposed method is an efficient way for analysis and prediction of coal microfracturing and the associated microscale rock mechanical behavior.

6.1 Introduction

Coal bed methane (CBM) is an unconventional energy resource, which exists in coal mines and deep unmineable coal seams (Hamawand et al., 2013). Recently, due to the decline in conventional energy resources coupled with a globally increasing energy demand (Lior 2008), CBM has gained increasing popularity (Connell et al., 2011; Pillalamarry et al., 2011; Hamilton et al., 2015; Vishal et al., 2015). Furthermore, CBM can be enhanced (enhanced coal bed methane, ECBM), e.g. through CO_2 injection, which efficiently displaces CH_4 from the coal matrix (White et al., 2005; Saghafi 2010). However, CO_2 injection dramatically reduces the coal seam's permeability (Mazumder et al., 2006; Siriwardane et al., 2009; Anggara et al., 2016), which largely limits application of this technology. Mechanistically, cleats (the main flow conduits in coal) close due to coal matrix swelling induced by CO_2 adsorption (Shi and Durucan 2005b; Wu et al., 2011; Zhang et al., 2016b; Liu and Rutqvist 2010; Espinoza et al., 2014) and it has recently been discovered that the swelling stress in the coal matrix can fracture the unswelling phase (i.e. inorganic mineral), Zhang et al. 2016b. However, the detailed failure mechanisms and swelling stress quantification are still poorly understood due to only limited theoretical understanding of the micro-scale rock mechanical performance. It is thus of vital importance to further understand these mechanical changes in the coal so that advanced ECBM techniques can be developed.

The mechanical properties of small areas (up to nanoscale) on a material's surface can now be obtained by nanoindentation measurements; such method has for instance been applied to natural rock samples including sandstone, limestone, shale and coal (Zhu et al., 2009; Bobko et al., 2011; Lebedev et al., 2014; Manjunath and Nair, 2015; Vialle and Lebedev, 2015; Liu et al., 2016). Thus nanoindentation gives

us a way to identify the mechanical properties of heterogeneous coal (note that coal consists of the organic coal base matrix, inorganic minerals and pores). These mechanical properties are essential input data into numerical models, which can predict the mechanical behavior of the whole (heterogeneous) material. Earlier studies considered the coal matrix as a homogenous elastic continuum (e.g. Izadi et al., 2011), which obviously cannot capture the clearly heterogeneous character of the coal, and thus can only provide rather biased predictions. To overcome this serious limitation we use discrete element method (DEM) modelling (cp. Cundall and Strack, 1979; Wang et al., 2014; Zhang et al., 2016g; Bai et al., 2016), where each material – coal matrix, mineral and void are assigned their respective true and individual mechanical properties, and combine this with high resolution x-ray micro-computed tomography (microCT) imaging, which can provide the detailed 3D morphology of the coal (Zhang et al., 2016b, 2016c, 2016d; Jing et al., 2016; Mostaghimi et al., 2017). Thus, in this paper, using this approach, we were able to quantify the swelling stresses generated by supercritical CO_2 injection into coal, and to identify the failure mechanisms occurring in the un-swelling phase.

6.2 Experimental work

A small cylindrical coal plug (5 mm diameter and 10 mm length) was cut from a heterogeneous subbituminous medium rank coal block obtained from a coal seam at ~650m to 700m depth (buried at Permian period) from Pingdingshan coal mine, China; the generalized stratigraphic column is shown in Figure 6-1. The coal had a 54% ($\pm$2%) carbon content and a 36% ($\pm$1%) volatile matter content (measured by Chinese Standard GB/T 212-2008 and DL/T 1030-2006; Xu et al., 2016; Zhang et al., 2016f), additional properties are tabulated in Table 6-1.The microstructure of the

sample is shown in Figure 6-2, the coal matrix, cleats and mineral phase can clearly be seen. The mineral was identified as calcite in SEM-EDS analysis. This plug was mounted into a HPHT (high pressure – high temperature) x-ray transparent flow cell (core holder), which was integrated into an in-situ microCT core flooding system (cp. Lebedev et al., 2016; Zhang et al., 2016b, 2016c; Iglauer et al., 2011; Rahman et al. 2016). The plug was vacuumed for 8 hours and subsequently more than 5000 PV (pore volumes) of $scCO_2$ were injected at typical reservoir conditions (confining pressure = 15 MPa, pore pressure = 10 MPa, temperature = 323 K (50$^{\mathrm{o}}$C), Pentland et al., 2011; Iglauer et al., 2011). The coal plug was imaged at high resolution (voxel size = 3.43 μm) with an Xradia VersaXRM instrument in 3D, before and after $scCO_2$ flooding. Indeed the sample's micro-morphology changed significantly, micro cleats/fractures in the coal matrix closed due to swelling induced by $scCO_2$ adsorption (cp. 3 and 5 in Figure 6-3), and new fractures appeared in the un-swelling calcite phase (cp. 1, 2 and 4 in Figure 6-3); see Zhang et al., (2016b) for the details of this in-situ microCT $scCO_2$ core flooding experiment.

Depth (m)	Graphic	Explanation	Thickness
		clay, mud, sand with gravel and calcrete	31
		Sandstone	161
		Sandstone	23
		clay, mud, silty sandstone	98
		Sand and mud interlayer	187
		mudstone	46
		Sand and mud interlayer	73
		Mudstone	16
		clay, mud, silty sandstone	33
		Coal	14
		Sand and mud interlayer	59
		clay, mud, silty sandstone	24
		Coal	10
		clay, mud, silty sandstone	75
		clay, mud, silty sandstone	80
		Coal	24
		Limestone	>50

Figure 6-1 The generalized stratigraphic column of the Pingdingshan coal mine from which the coal sample was obtained.

Table 6-1 Physical properties of the coal studied (Xu et al. 2016; Zhang et al. 2016d).

M (%)	V (%)	A (%)	C_f (%)	E (GPa)	υ	ρ (g/cm^3)
6.9	36.0	4.2	54.0	2.6	0.3	1.35

Note: M is the moisture content; V is the volatile matter; A is the ash yield; C_f is the fixed carbon content; E is Young's Modulus; υ is Poission's ratio; and ρ is the bulk density.
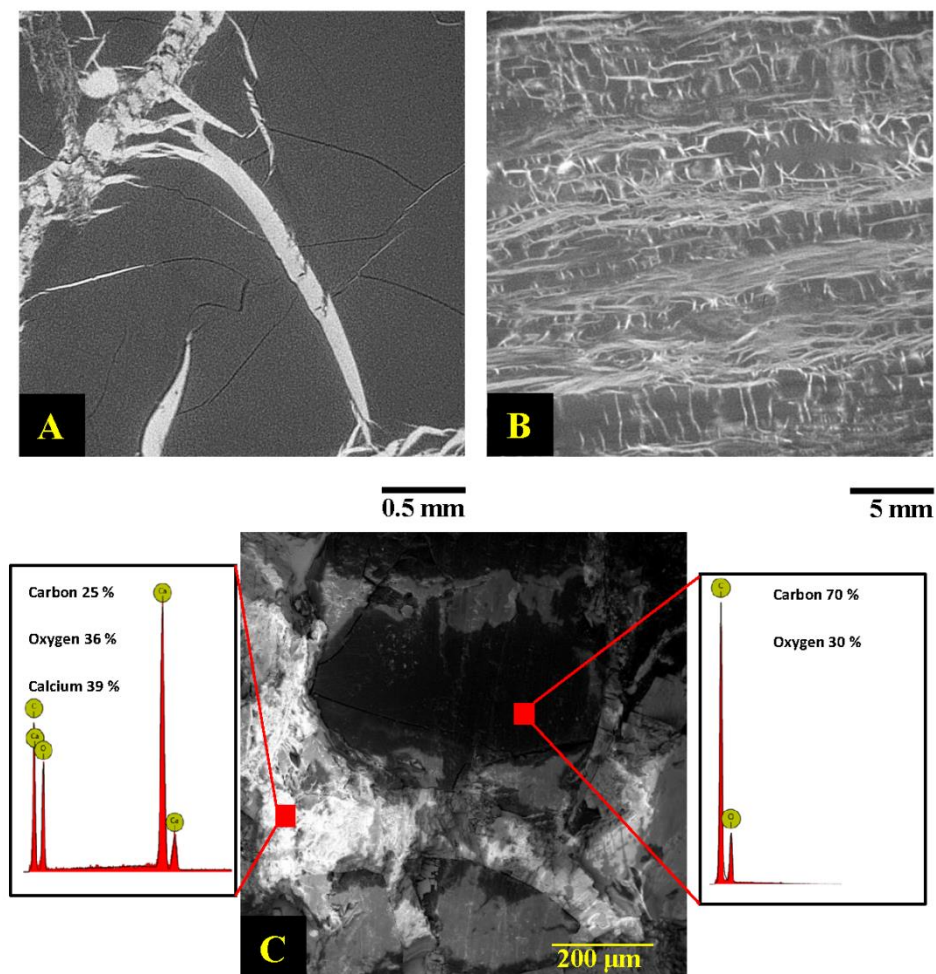
Figure 6-2 The micro structure of the unflooded coal sample; (A), (B): 2D microCT slices through the greyscale image; (A) 3.43 µm voxel size; (B) 33.7 µm voxel size, grey is coal matrix, black is void space, and white is calcite; (C) SEM image of the coal and associated EDS spectra; calcite is white and coal matrix is black/dark grey.
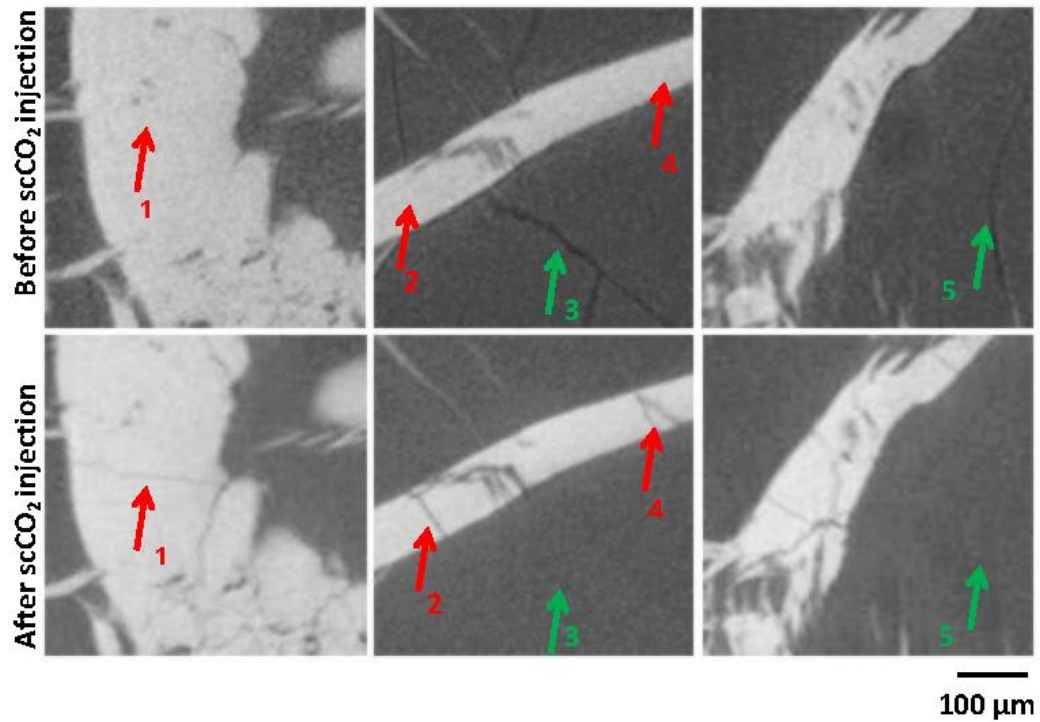
Figure 6-3 2D microCT slices through the coal sample before and after $scCO_2$ injection (3.43 μm resolution); new fractures appeared in the calcite after flooding: 1, 2 and 4; the original micro cleats in the coal matrix closed after flooding: 3 and 5.

6.3 The stress-strain method

Initially we estimated the swelling stress via the traditional stress-strain method using the volume fractions measured (i.e. strains measured) on the microCT images, Table 6-2 (note that the volume strain ε = (the volume difference before and after CO_2 flooding) / (original volume). Negative values represent compression, while positive values represent expansion.

What is more, in an elastic 3D coordinate system, ε has following relation with Young's modulus (E), stress (σ), and Poisson's ratio (v), e.g. Fjar et al., 2008; Ahmed and Meehan (2016):

$$\begin{cases} \varepsilon_x = \frac{1}{E}\left[\sigma_x - \upsilon\left(\sigma_y + \sigma_z\right)\right] \\ \varepsilon_y = \frac{1}{E}\left[\sigma_y - \upsilon\left(\sigma_x + \sigma_z\right)\right] \\ \varepsilon_z = \frac{1}{E}\left[\sigma_z - \upsilon\left(\sigma_x + \sigma_y\right)\right] \end{cases}$$ 7-1

Based on the former stress-strain studies on coal (cp. Seidle et al., 1992; Sheorey, 1994; Tajduś, 2009; Liu and Rutqvist, 2010; Espinoza et al., 2013), we assumed that the coal was under isotropic elastic and hydrostatic conditions, thus

$$\sigma_x = \sigma_y = \sigma_z$$ 7-2

It follows for the volume matrix strain (ε_v):

$$\varepsilon_v = 3\varepsilon_x = 3\frac{1}{E}\left[\sigma_x - \upsilon 2\sigma_x\right]$$ 7-3

As the strain (ε) is equal to the volume matrix strain (ε_v) / 3, thus

$$\varepsilon = \frac{1}{E}\sigma(1 - 2\upsilon)$$ 7-4

So,

$$\sigma = \frac{E\varepsilon}{1-2\upsilon}$$ 7-5

Furthermore, the effective stress (σ_e) can be described as a function of internal swelling stress (σ_s), Liu and Rutqvist (2010):

$$\sigma_e = \sigma_t - \alpha P + \sigma_s$$ 7-6

Thus before scCO$_2$ injection (without swelling effect), the effective stress for the material can be described as

$$\sigma_{e1} = \sigma_{t1} - \alpha P_1$$ 7-7

After scCO$_2$ injection (with swelling effect)

$$\sigma_{e2} = \sigma_{t2} - \alpha P_2 + \sigma_s \qquad\qquad 7\text{-}8$$

and the differential effective stress (before and after CO_2 adsorption) σ (generated by the strain change) is thus:

$$\sigma = \sigma_{e2} - \sigma_{e1} = \sigma_{t2} - \alpha P_2 + \sigma_s - \sigma_{t1} + \alpha P_1 = \frac{E\varepsilon}{1-2v} \qquad\qquad 7\text{-}9$$

Thus the internal swelling stress (σ_s) can be obtained by

$$\sigma_s = \frac{E\varepsilon}{1-2v} - \sigma_{t2} + \alpha P_2 + \sigma_{t1} - \alpha P_1 \qquad\qquad 7\text{-}10$$

Where σ_{t2} is the overburden (confining) pressure (15 MPa), P_2 is the pore pressure (10 MPa) for the second microCT scan, σ_{t1} is 5 MPa, P_1 is 0 MPa for the first microCT scan, and α is Biot's coefficient. Based on previous studies (e.g. Gray, 1987; Liu and Rutqvist, 2010), we set Biot's coefficient $\alpha = 1$. For the coal matrix, we set a Young's modulus (E) of 2 GPa and a Poisson's ratio (v) of 0.15 (an estimated value from an ultrasonic test on a sister coal plug, measured with a RIGOL DS4022 instrument at 1 MHz frequency). After inputting the data into equation (10), we obtained an internal swelling stress value of 20.52 MPa. However, the shortcoming of this stress-strain prediction was significant; the result cannot reflect the swelling progress which is dynamic (different swelling degrees induce different internal swelling stresses), and the assumption of isotropic elasticity is a strong simplification when modelling highly heterogeneous coal. Most importantly, this method cannot answer the questions about the failure mechanisms occurring in the mineral phase. Thus, further numerical modelling is required (see DEM simulations below).

Table 6-2 Volumetric and strain data for each phase before and after CO_2 flooding.

Phases	The volume before scCO$_2$ injection [$10^6 \mu m^3$]	The volume after scCO$_2$ injection [$10^6 \mu m^3$]	Volume matrix Strain (ε_v)	Strain (ε)
Void (Micro cleats/fractures)	26.17	0	-1	-1
Coal matrix	5500.08	5618.61	0.022	0.007
Calcite mineral	2171.02	2078.66	-0.043	-0.014
Total	7697.270	7697.27	0	0

6.4 Discrete Element Method (DEM) simulation

The Discrete Element Method (DEM) has become a powerful numerical tool for analyzing the dynamic mechanical behavior of complex objects (Cundall and Strack, 1979; Scholtès and Donzé, 2012). Precisely, DEM models objects as an assembly of interacting particles, and the key advantage of DEM is that specific attributes (features, bonds, contacts, frictions and boundary conditions) can be assigned to each particle (and thus each material) simultaneously. We used the popular DEM built-in software – Particle Flow Code (PFC2D) in this study. In PFC2D, the DEM simulations are based on Newton's second law and the force-displacement law at particle contacts. While the force-displacement law determines the contact force exerted on each particle (these forces arise from the relative motion of the particles to each other); Newton's second law determines the motion for each particle (which arise from the contact and body forces acting upon the particle), Cundall and Strack

(1999). The constitutive behavior of the material is simulated by stiffness model, slip model and bonding model. The stiffness model provides the elastic relationship between the displacement and contact force, and the slip model describes the relationship between normal and shear contact force when the contacted particles slip in relation to each other; and the bonding model limits the total shear and normal forces in the contact areas (Cundall and Strack, 1999; Sarmadivaleh, 2012; Hashemi et al., 2014; Bewick et al., 2014; Zhang et al., 2016g; Zhou et al., 2016; Jiang et al., 2016). Here we used a small particle size (less than 6 µm) to simulate the coal matrix and calcite mineral at micro-scale; and the effective stress applied in the true experiment has been added via a boundary condition set, see below. Furthermore, the contact bond model (see Potyondy and Cundall, 2004) was used in our simulation; and most importantly, the coal swelling effect was modelled by continuously increasing the volume of the coal matrix particles.

Six simulations were performed (A – E), Figure 6-4. Each simulation used a high resolution 2D microCT slice acquired experimentally (thus different micro-morphologies were tested, Figures 4 and 5) to provide realistic geometrical input data. The simulations covered different areal sizes: A and B were 0.4 mm × 0.4 mm, C was 0.85 mm × 0.85 mm, D and E were 1.37 mm × 1.37 mm. The number of particles in examples A, C and D were set to ~7000, in example B to ~20000 and in example E both particle numbers were tested (i.e. both, ~7000 in E2, and ~20000 in E1). The volume of each particle in the coal matrix was increased until a total volume (of each particle) increase of 1% was realized (which simulated the coal matrix swelling during $scCO_2$ injection). A servo-control mode boundary condition with 5 MPa effective stress was used to mimic the experimental conditions (where 5 MPa effective stress was applied, see above). Other input parameters are summarized

in Table 6-3. To obtain reasonable shear/normal bond strengths in the DEM simulations, calibration simulations were run on example E for different bond strengths (ranging from 1 MPa to 110MPa), see Figure 6-6.

These calibration simulations used model E and a 1 % total coal particle volume swelling factor. Thus after comparing the computed fracture morphologies with the experimental microCT tomography results, we chose 50 ± 5 MPa (normally distributed) for the shear/normal bond strengths in all DEM simulations. Note that the bond strength input did not affect the final internal swelling stress output, and the maximal von Mises stresses predicted for all cases (at 1 % particle swelling rate) were similar, around 20 MPa.

Table 6-3 Particle properties used in the DEM simulations.

Input property	Value
Particle density (coal matrix)	1052 kg/m^3
Particle density (calcite mineral)	2000 kg/m^3
Particle radius	6 µm to 9µm (evenly distributed)
Friction coefficient	0.5
Shear Bond strength[*]	50 ± 5 MPa (normally distributed)
Normal Bond strength[*]	50 ± 5 MPa (normally distributed)
Young's modulus (coal matrix)[#]	1 GPa and 8 GPa (normally distributed)
Young's modulus (calcite mineral)[#]	18 GPa

[*]The Bond strength was chosen after conducting calibration simulations, see text for details.

#The Young's moduli were obtained from the nanoindentation tests, see text for details.
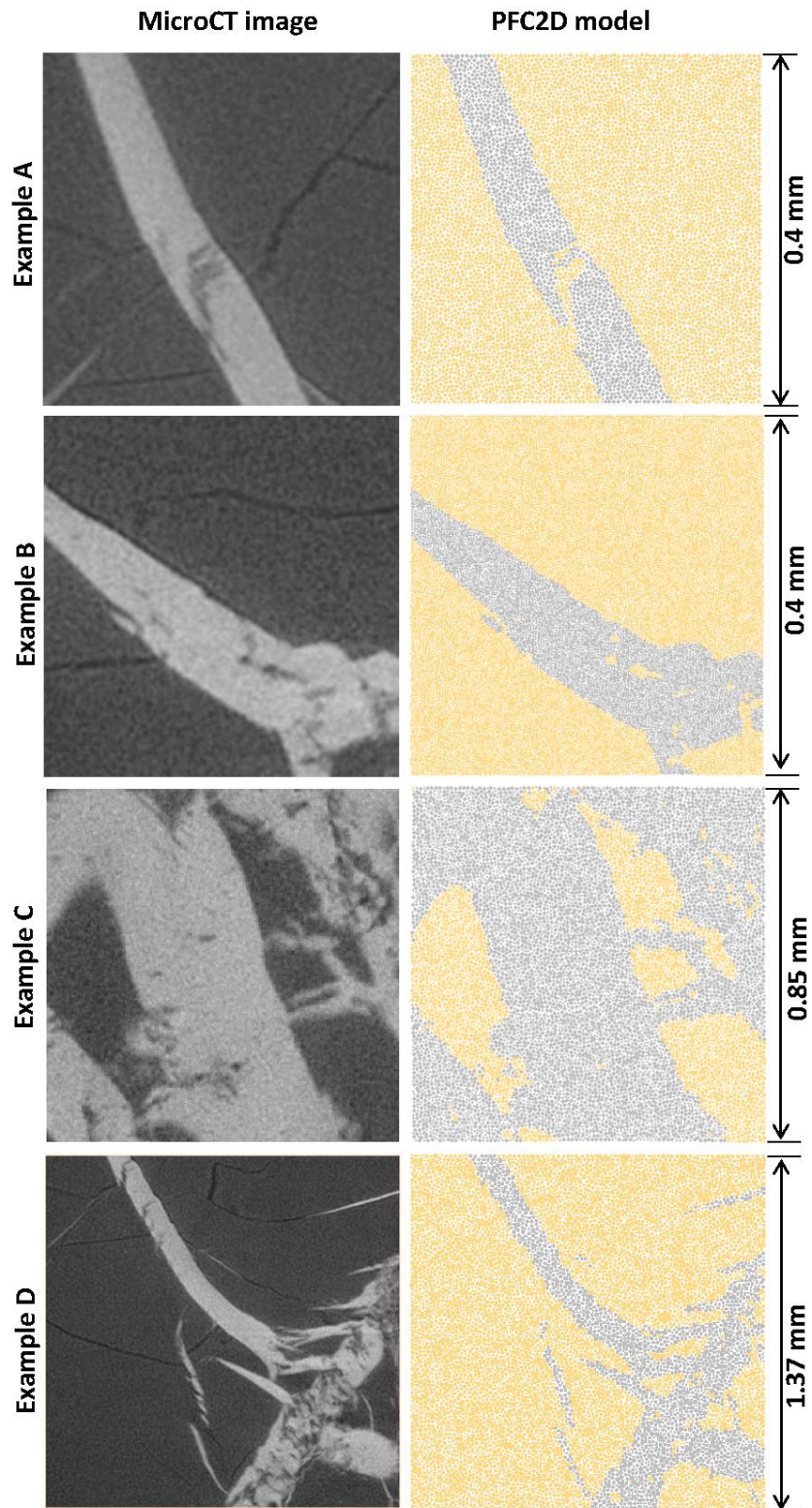
Figure 6-4 PFC2D models and associated microCT images, examples A – D; A, C and D used ~7000 particles, and B ~20000 particles.
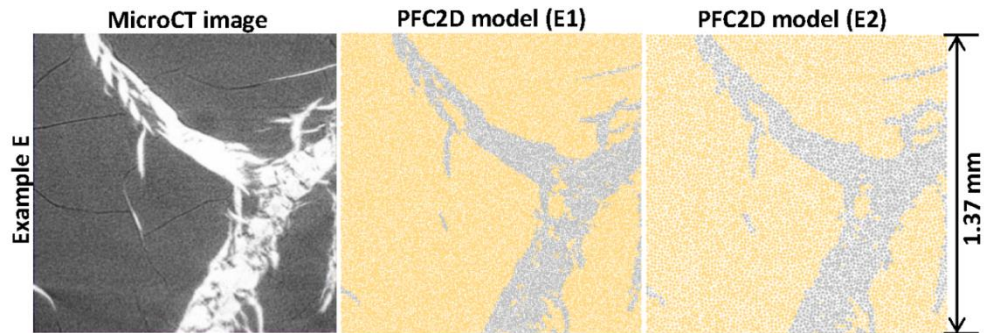
Figure 6-5 The PFC2D models with the associated microCT image, example E: E1 used ~20000 particles; and E2 ~7000 particles.
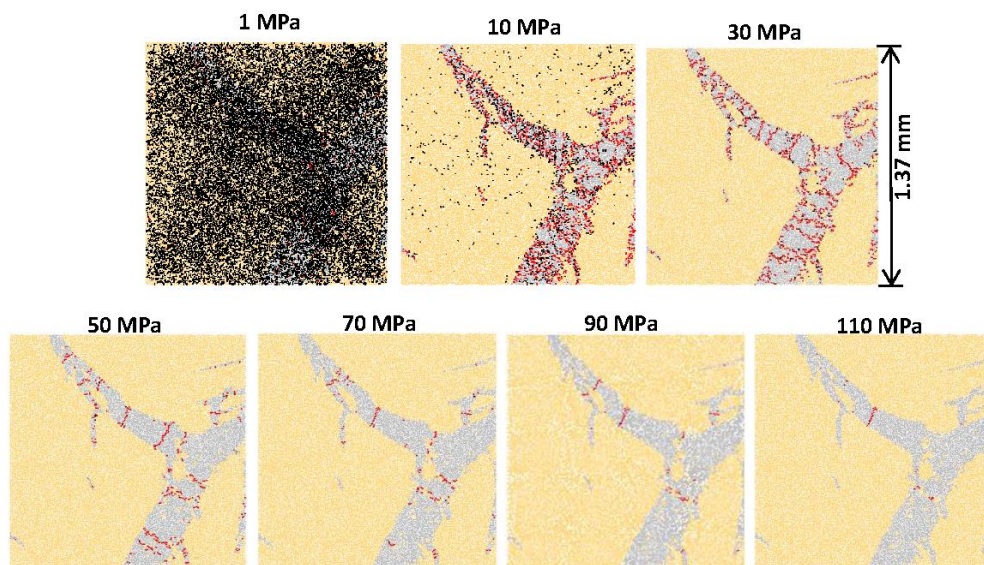
Figure 6-6 Calibration simulations for setting the bond strength. Simulations for 1 MPa to 110 MPa bond strength are shown, for a 1 % coal matrix swelling factor.

6.5 Nanoindentation testing

The IBIS nanoindentation system and Berkovich nano-indenter were chosen for the nanoindentation tests, Figure 6-7. A cuboid coal sample ($l \times w \times h$ = 5 mm $\times$ 5 mm $\times$ 2 mm) was cut and carefully polished, and mounted on the objective stage. Subsequently the penetration depth (h) – loading/unloading force (P) curves were measured for each test point. Specifically 625 data points on a symmetric 25×25 grid (240 µm $\times$ 240 µm spacing) were measured. The maxim loading force was set to 4 mN (which is smaller than the one used in former studies on other natural rocks, Lebedev et al., 2014; Vialle and Lebedev, 2015; Zhang et al., 2016a) due to the brittle and soft nature of the coal sample. Finally, the indentation modulus (M) was obtained from the measured P-h curves, equation 8 (Fischer-Cripps, 2004):

$$M = \frac{1}{2} \frac{\sqrt{\pi}}{\sqrt{A}} \frac{dP}{dh} \qquad\qquad 7\text{-}11$$

where A is the contact area, and dP / dh was measured from several unloading curves at maximum applied force P_{max} and maximum penetration depth h_{max}. For an isotropic material Young's modulus E and Poisson's ratio v can then be related to M as:

$$M = \frac{E}{1-v^2} \qquad\qquad 7\text{-}12$$

Furthermore, E can be approximated via (Fischer-Cripps, 2004; Lebedev et al., 2014):

$$0.75\,M \leq E \leq M \qquad\qquad 7\text{-}13$$

when the material's Poisson's ratio ranges from 0 to 0.5 (the Poisson's ratio is less than 0.5 for most natural materials, we estimated $v = 0.15$ from the bulk volume ultrasonic test and $v \approx 0.3$ for coal was reported by Wang et al., 2014),

The nanoindentation results are presented in Figure 6-7. It is clear from this data that the indentation modulus of the mineral phase (always larger than 15 GPa) was significantly higher than that of the coal matrix. Thus, for the DEM input, the E for the coal matrix was set to 1 GPa to 8 GPa (normally distributed) recall that coal is highly heterogeneous, and 18 GPa for the calcite phase.
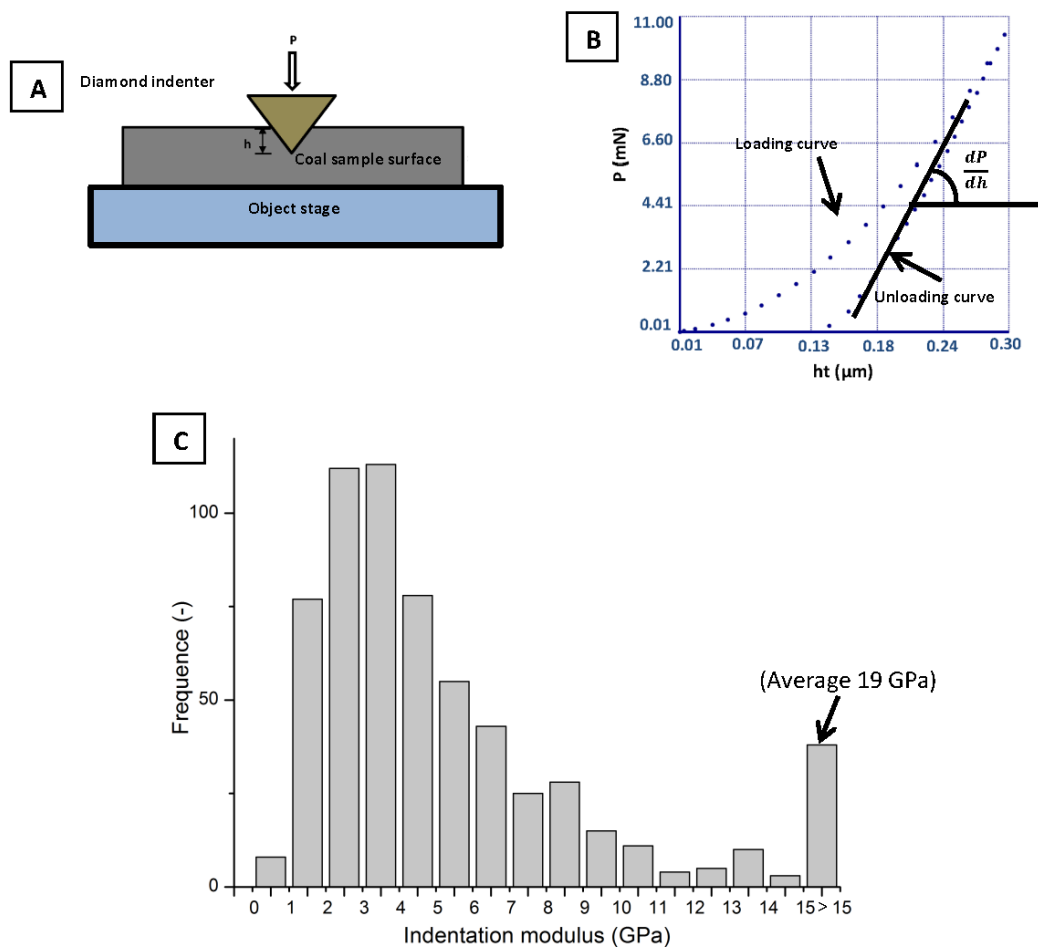
Figure 6-7 (A) Schematic of the nanoindentation experiment, the indenter penetrates into the sample during loading; (B) a typical loading - unloading curve for the quartz calibration sample (A Young's modulus of 72.5 GPa, a Poisson's ration of 0.17, and an indentation modulus of 74.5 GPa were measured) where the h (μm) is the

indentation depth and P (mN) is the indentation force; (C) indentation moduli (GPa) measured on the coal sample.

6.6   Results and discussion

The DEM simulations successfully predicted the change in coal microstructure caused by coal matrix swelling, which again was induced by scCO$_2$ injection (see Figures 6-8 and 6-9). Clearly cracks appeared in the mineral phase when the coal matrix volume increased by 1 %, consistent with the experimental microCT observations (cp. Figure 6-3). Most failures in the calcite mineral phase were identified as tensile failures (red colored cracks in Figures 6-8 and 6-9) these appeared during the coal matrix swelling. We were furthermore able to compute the in-situ stresses, c.p. the von Mises stress map in Figure 6-8 and Figure 6-9). Note that the von Mises stress K is defined by

$$\sigma_1^2 - \sigma_1\sigma_2 + \sigma_2^2 = 3K^2 \qquad\qquad 7\text{-}14$$

and a K map can describe the in-situ stress exerted on each particle in the model. Clearly these stress fields were highly anisotropic, and maximum effective stresses concentrated on the mineral surface in most cases (Example A, B, D and E). The von Mises stresses continuously increased with increasing coal matrix swelling until failure (i.e. until the mineral was fractured). During failure, the swelling stresses generated were released, and the von Mises stress decreased again.

Furthermore, the number of particles in the simulation had no significant influence on the in-situ stresses (compare simulations E1 and E2 in Figure 6-9), although a larger particle number predicted a more realistic fracture morphology. Moreover, the volume fraction and morphology of the mineral was identified as the main factor determining the highest in-situ stresses; see example C (where the coal matrix

volume fraction was only 20 %) in Figure 6-8; note that in this example, the highest in-situ effective stresses were located in the coal matrix, but not on the mineral surface, contrary to the behavior of the other examples. This can be explained by a morphological feature; the coal matrix was fully enclosed and trapped by the mineral phase, thus the generated stresses could not be released until all surrounding minerals failed. However, the mineral was less likely to fail as it had a much higher volume fraction than the coal matrix, and its Young's modulus was significantly higher than that of the coal matrix; thus abnormally high stresses appeared inside the coal.

Finally the relationship between maximum von Mises stress (MPa), in in-situ von Mises stress map, and swelling percentage could be calculated, cp. Figure 6-10. Thus, the dynamic swelling stress (in-situ effective stress minus the original effective stress) could be obtained: the swelling stress in the normal areas (with an approximately 70 % coal matrix volume fraction) reached up to 20 MPa, while they reached more than 35 MPa in some areas where the coal matrix was enclosed by the mineral phase. In a field scale CO_2-ECBM project, such abnormally high swelling stresses (caused by CO_2 injection) can result in a series of problems such as well borehole instabilities and/or fault re-activation (Karacan et al., 2011; Tu et al., 2016; Zhai et al., 2016). These effects should be analyzed further as they pose a significant geohazard.
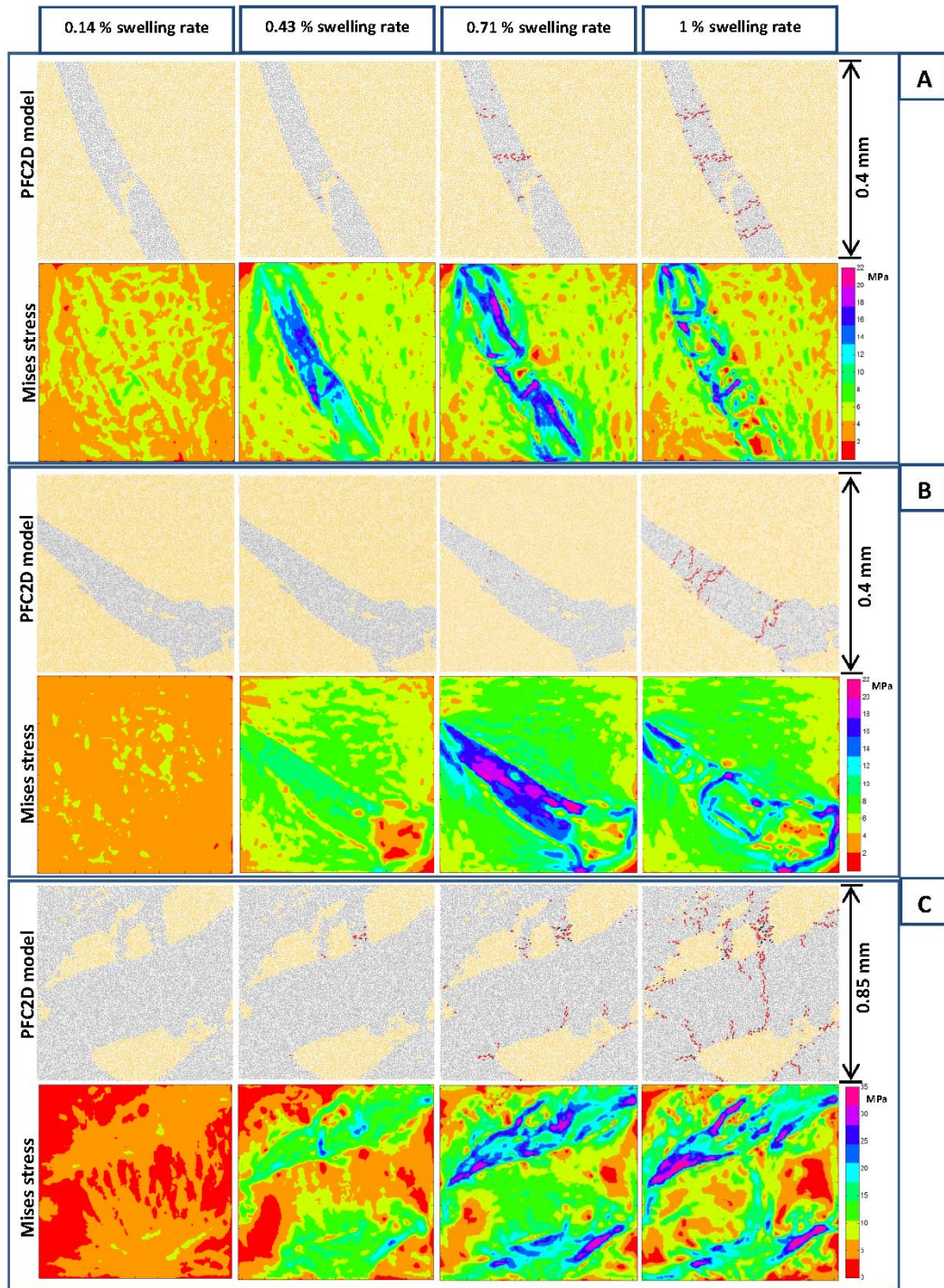
Figure 6-8 Fractures development due to scCO$_2$ injection predicted via DEM. The in-situ mises stress maps are shown in color below the PFC models; (A) example A; (B) example B; and (C) is example C. Note: the red colored cracks indicate tensile failures and the black colored shear failures.
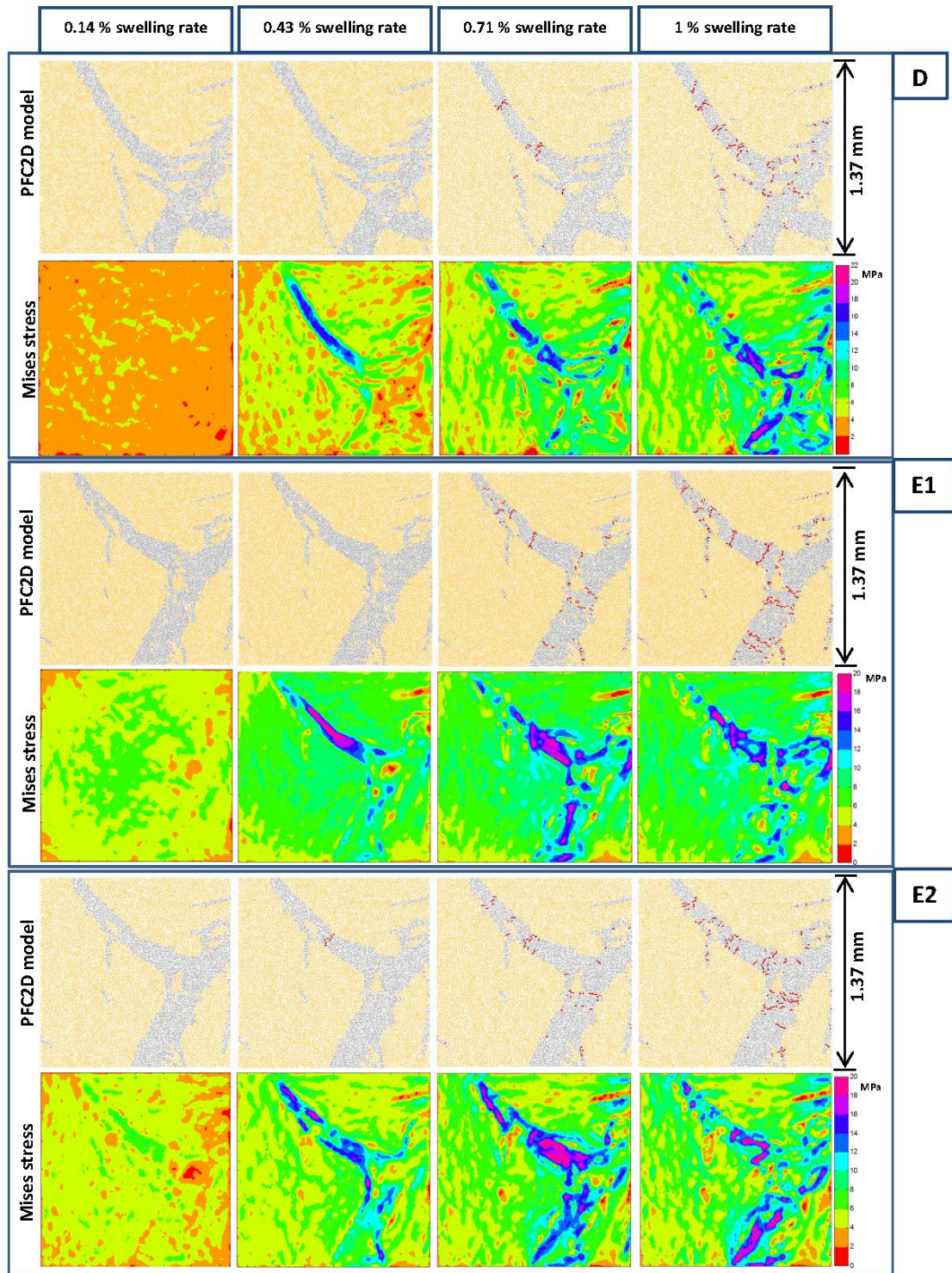
Figure 6-9 Fractures development due to scCO$_2$ injection predicted via DEM. The in-situ mises stress maps are shown in color below the PFC models; (D) example D;

(E1) example E1; and (E2) is example E2. Note: the red colored cracks indicate tensile failures and the black colored shear failures.
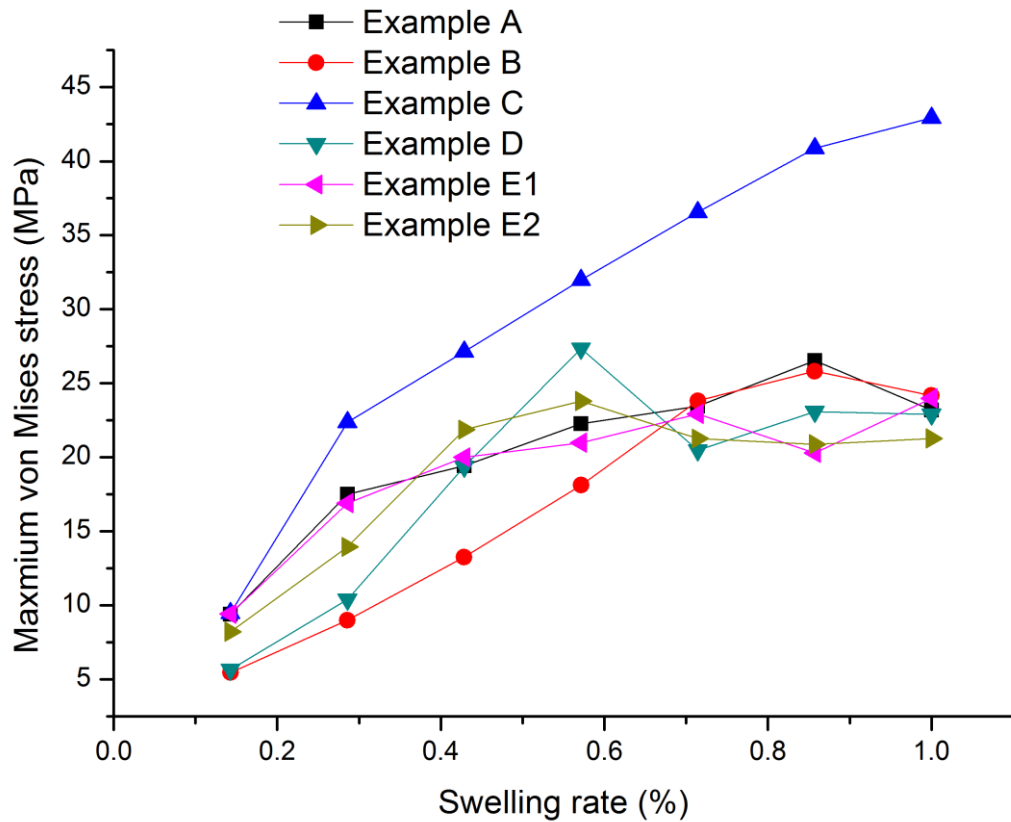
Figure 6-10 The relationship between maximum von Mises stress (from in-situ von Mises stress map, Figures 8 and 9) and swelling rate (%).

6.7   Conclusion

CO_2 can be injected into coal seams to enhance methane producti on (White et al., 2005; Saghafi 2010); however, the resulting coal matrix swelling effect leads to coal cleat closure and a dramatic permeability reduction (Karacan 2003; Zhang et al., 2016f); furthermore, it has been recently observed that the unswelling phase fractured due to the induced swelling stresses (Zhang et al., 2016b). However, how precisely such swelling stresses are generated and the associated failure mechanisms

in the unswelling phase are not fully understood. Thus, in this chapter, it developed a novel microscale discrete element method (DEM) which combines x-ray microCT tomography imaging and nanoindentation measurements to predict such microscale rock mechanical performance.

These DEM simulations were run on five test samples where different geometrical morphologies were examined (the microCT images provided this input). The DEM models successfully simulated the swelling process and predicted failure morphologies in the mineral phase consistent with the microCT observations. Based on the simulation results, it concludes that the mineral phase shows tensile failure due to compression caused by coal matrix swelling. The von Mises stresses were quantified, and the maximum coal swelling stresses reached more than 35 MPa in areas which were fully enclosed by (unswelling) mineral. Such abnormally high stresses pose a geohazard risk in CO_2-ECBM projects. However, this chapter only covered the 2D simulation, I strongly recommend conduct the 3D simulation in the future to better understand the CO_2 induced swelling effect.

Chapter 7   Conclusion

7.1   The findings and highlights

In this thesis, at first, the coal microstructure and nanoscale rockmechanical properties for different rank of coal have been investigated. It concludes that the low rank coal had the most abundant pore system (including large pores and tiny pores) and high rank coal has the more mature fracture (cleat) system. Thus, the safety issues (geohazard) for low rank coal seam should be always in priority consideration than high rank coal seam during the coalfield exploration, CBM / ECBM, and CCS projects.

Then, imaged coal plugs at high resolution (33.7 um and 3.43 μm voxel size) with an x-ray micro-computed tomograph in 3D as a function of effective stress (0 MPa, 5 MPa, 10 MPa) to measure the coal micro − structure morphological change. We conclude that effective stress causes closure of micro cleats in the coal, which leads to a drastic drop in permeability, but only a moderate drop in porosity as most void space is located in the coal matrix as nanopores.

The dry and swollen (due to brine adsorption) coal plugs with 3D microCT at a high voxel resolution $(3.4 \ \mu m)^3$ are also imaged. Micro cleats were visible in the coal matrix and the mineral phase, consistent with SEM imaging. However, after brine injected into a dry coal plug, more than 80% of these cleats were closed due to swelling, which caused a dramatic reduction in porosity and particularly permeability. However, the cleats in the mineral phase were still open after the coal matrix swelling; this could be explained by the lower internal stress in the mineral and the lower compressibility of the mineral. It thus concludes that water adsorption into dry

coal causes significant swelling effects. This swelling drastically alters the microstructure of the coal; which again drastically reduces coal permeability.

Using in-situ reservoir condition x-ray micro-computed tomography imaging, it was observed for the first time how the micro cleat structure inside the coal matrix closed induced by supercritical CO_2 flooding in-situ, and associated fracturing of the mineral phase (embedded in the coal). It concludes that coal matrix swelling due to CO_2 adsorption dramatically changes the morphology of the micro cleat network and thereby drastically reduces coal permeability, and such swelling induces fracturing of the mineral phase in the coal seam.

The DEM model was also successfully simulating the swelling process and predicted failure morphologies in the mineral phase consistent with the microCT observations. Based on the simulation results, it concludes that the mineral phase shows tensile failure due to compression caused by coal matrix swelling. The von Mises stresses were also quantified, and the maximum coal swelling stresses reached more than 35 MPa in the areas which were fully enclosed by (unswelling) mineral. Such abnormally high stresses pose a geohazard risk in CO_2-ECBM projects.

7.2 Outlook for future work

The multiscale coal structures and the related rockmechanical properties are extremely important for the enhanced coal bed methane and carbon dioxide geosequestration. The future work in this area can be conduct on the morphology change of different rank coal during CO_2 injection; the different rank coal has different composition, thus how the morphology change may be different and need to be understood.

Also, the cleats morphology change during CO_2-ECBM is a "competition" process - the swelling effect close the cleats, the effective stress increasing due to methane production close cleats, and the methane production also results the matrix shrinkage with opening the cleats), and a comprehensive model is still missing for describe this phenomena.

References

Ahmed, U., Meehan, D.N., 2016. Unconventional oil and gas resources: exploitation and development. CRC Press.

Al-Yaseri, A.Z., Roshan, H., Xu, X., Zhang, Y., Sarmadivaleh, M., Lebedev, M., Barifcani, A. and Iglauer, S., 2017a. Coal Wettability After CO_2 Injection. *Energy & Fuels, 31*(11), pp.12376-12382.

Al-Yaseri, A.Z., Roshan, H., Zhang, Y., Rahman, T., Lebedev, M., Barifcani, A. and Iglauer, S., 2017b. Effect of the Temperature on CO2/Brine/Dolomite Wettability: Hydrophilic versus Hydrophobic Surfaces. *Energy & Fuels*, *31*(6), pp.6329-6333.

Anggara, F., Sasaki, K. and Sugai, Y., 2016. The correlation between coal swelling and permeability during CO 2 sequestration: A case study using Kushiro low rank coals. *International Journal of Coal Geology 166*. Pp. 62-70.Bai, Q.-S., Tu, S.-H., Zhang, C., Zhu, D., 2016. Discrete element modeling of progressive failure in a wide coal roadway from water-rich roofs. *International Journal of Coal Geology 167*, 215-229.

Bachu, S., Bonijoly, D., Bradshaw, J., Burruss, R., Holloway, S., Christensen, N.P. and Mathiassen, O.M., 2007. CO 2 storage capacity estimation: methodology and gaps. *International Journal of Greenhouse Gas Control*, *1*(4), pp.430-443.

Baud, P., Vinciguerra, S., David, C., Cavallo, A., Walker E., and Reuschlé T., 2009. Compaction and failure in high porosity carbonates: Mechanical data and microstructural observations, in *Rock Physics and Natural Hazards*, edited, pp. 869-898, Springer.

Bewick, R., Kaiser, P., Bawden, W., Bahrani, N., 2014. DEM simulation of direct shear: 1. Rupture under constant normal stress boundary conditions. *Rock Mechanics and Rock Engineering 47*, pp.1647-1671.

Blunt, M. J., Bijeljic, B., Dong, H., Gharbi, O., Iglauer, S., Mostaghimi, P., Paluszny, A. and Pentland, C., 2013. Pore-scale imaging and modelling. *Advances in Water Resources, 51*, pp. 197-216.

Bobko, C. P., Gathier, B., Ortega, J. A., Ulm, F. J., Borges, L. and Abousleiman, Y. N., 2011. The nanogranular origin of friction and cohesion in shale—a strength homogenization approach to interpretation of nanoindentation results. *International Journal for Numerical and Analytical Methods in Geomechanics, 35*(17), pp. 1854-1876.

Bradshaw, J., Bachu, S., Bonijoly, D., Burruss, R., Holloway, S., Christensen, N.P. and Mathiassen, O.M., 2007. CO_2 storage capacity estimation: issues and development of standards. *International journal of greenhouse gas control*, *1*(1), pp.62-68.

Buades, A., Coll, B. and Morel, J.-M., 2005. A non-local algorithm for image denoising. in *Computer Vision and Pattern Recognition, 2005. CVPR 2005. IEEE Computer Society Conference on*: IEEE. pp. 60-65.

Cai, Y., Liu, D., Mathews, J.P., Pan, Z., Elsworth, D., Yao, Y., Li, J., Guo, X., 2014. Permeability evolution in fractured coal—Combining triaxial confinement with X-ray computed tomography, acoustic emission and ultrasonic techniques. *International Journal of Coal Geology 122*, pp. 91-104.

Carroll, J.J., Slupsky, J.D. and Mather, A.E., 1991. The solubility of carbon dioxide in water at low pressure. *Journal of Physical and Chemical Reference Data*, *20*(6), pp.1201-1209.

Charrière, D. and Behra, P., 2010. Water sorption on coals. *Journal of colloid and interface science, 344*(2), pp. 460-467.

Chen, Z., Pan, Z., Liu, J., Connell, L.D., Elsworth, D., 2011. Effect of the effective stress coefficient and sorption-induced strain on the evolution of coal permeability: experimental observations. *International Journal of Greenhouse Gas Control 5*, pp. 1284-1293.

Clarkson, C., Bustin, R., 1999. The effect of pore structure and gas pressure upon the transport properties of coal: a laboratory and modeling study. 1. Isotherms and pore volume distributions. *Fuel 78*, pp. 1333-1344.

Cnudde, V. and Boone, M. N., 2013. High-resolution X-ray computed tomography in geosciences: A review of the current technology and applications. *Earth-Science Reviews, 123*, pp. 1-17.

Cnudde, V., Masschaele, B., Dierick, M., Vlassenbroeck, J., Van Hoorebeke, L. and Jacobs, P., 2006. Recent progress in X-ray CT as a geosciences tool. *Applied Geochemistry, 21*(5), pp. 826-832.

Connell, L.D., Lu, M., Pan, Z., 2010. An analytical coal permeability model for tri-axial strain and stress conditions. *International Journal of Coal Geology 84*, 103-114.

Connell, L.D., Sander, R., Pan, Z., Camilleri, M. and Heryanto, D., 2011. History matching of enhanced coal bed methane laboratory core flood tests. *International Journal of Coal Geology 87*(2), pp. 128-138.

Constantinides, G., Chandran, K. R., Ulm, F.-J. and Van Vliet, K., 2006. Grid indentation analysis of composite microstructure and mechanics: Principles and validation. *Materials Science and Engineering: A, 430*(1), pp. 189-202.

Creech, M. and McConachie, B., 2014. Reserve estimation and the influence of coal seams on coal seam gas productivity. in: Australasian Institute of Mining and Metallurgy.

Cui, X., Bustin, R. M., and Dipple, G., 2004. Selective transport of CO_2, CH_4, and N_2 in coals: insights from modeling of experimental gas adsorption data, *Fuel*, *83*(3), pp.293-303.

Cundall, P.A., Strack, O.D., 1979. A discrete numerical model for granular assemblies. *Geotechnique 2*9, pp. 47-65.

Cundall, P., Strack, O., 1999. Particle flow code in 2.

Dai, Z., Stauffer, P.H., Carey, J.W., Middleton, R.S., Lu, Z., Jacobs, J.F., Hnottavange-Telleen, K. and Spangler, L.H., 2014. Pre-site characterization risk analysis for commercial-scale carbon sequestration. *Environmental science & technology*, *48*(7), pp.3908-3915.

Day, S., Fry, R. and Sakurovs, R., 2008. Swelling of Australian coals in supercritical CO_2. *International Journal of Coal Geology, 74*(1), pp. 41-52.

Dryden, I. G. C., 1963. In Chemistry of Coal Utilization; Lowry, H. H., Ed.; Wiley: New York; pp 232-295.

Elliott, M. A.,1981. Chemistry of coal utilization. Second supplementary volume.

Enever, J., Casey, D., Bocking, M., 1999. The role of in-situ stress in coalbed methane exploration, Coalbed Methane: Scientific, Environmental and Economic Evaluation. Springer, pp. 297-303.

Espinoza, D., Vandamme, M., Dangla, P., Pereira, J.M., Vidal‑Gilbert, S., 2013. A transverse isotropic model for microporous solids: Application to coal matrix adsorption and swelling. *Journal of Geophysical Research: Solid Earth 118*, pp. 6113-6123.

Espinoza, D.N., Vandamme, M., Pereira, J.M., Dangla, P. and Vidal-Gilbert, S., 2014. Measurement and modeling of adsorptive–poromechanical properties of bituminous coal cores exposed to CO_2: Adsorption, swelling strains, swelling stresses and impact on fracture permeability. *International Journal of Coal Geology, 134*, pp. 80-95.

Fenghour, A., Wakeham, W. A., and Vesovic V., 1998. The viscosity of carbon dioxide, *Journal of Physical and Chemical Reference Data, 27*(1), pp. 31-44.

Finley M., 2013. BP statistical review of world energy. BP technical report.

Fischer-Cripps, A., 2004. Nanoindentation Springer. New York.

Fischer-Cripps, A. C., 2011 Nanoindentation. Springer. New York.

Fischer-Cripps, A. C., 2006. Critical review of analysis and interpretation of nanoindentation test data. *Surface and coatings technology, 200*(14), pp. 4153-4165.

Fjar, E., Holt, R.M., Raaen, A.M., Risnes, R. and Horsrud, P., 2008. Petroleum related rock mechanics (Vol. 53). Elsevier.

Flores, R.M., 2013. Coal and coalbed gas: fueling the future. Newnes.

Friedlingstein, P., Houghton, R.A., Marland, G., Hackler, J., Boden, T.A., Conway, T.J., Canadell, J.G., Raupach, M.R., Ciais, P. and Le Quere, C., 2010. Update on CO2 emissions. *Nature Geoscience*, *3*(12), pp.811-812.

Gale, J. and Freund, P., 2001. Coal-Bed Methane Enhancement with CO2 Sequestration Worldwide Potential. *Environmental Geosciences, 8*(3), pp. 210-217.

George, J.S. and Barakat, M.A., 2001. The change in effective stress associated with shrinkage from gas desorption in coal. *International Journal of Coal Geology*, *45*(2), pp. 105-113.

Gilfillan, S.M., Lollar, B.S., Holland, G., Blagburn, D., Stevens, S., Schoell, M., Cassidy, M., Ding, Z., Zhou, Z., Lacrampe-Couloume, G. and Ballentine, C.J., 2009. Solubility trapping in formation water as dominant CO_2 sink in natural gas fields. *Nature*, *458*(7238), pp. 614.

Golab, A., Ward, C.R., Permana, A., Lennox, P., Botha, P., 2013. High-resolution three-dimensional imaging of coal using microfocus X-ray computed tomography, with special reference to modes of mineral occurrence. *International Journal of Coal Geology 113*, pp. 97-108.

Golding, S.D., Uysal, I.T., Boreham, C.J., Kirste, D., Baublys, K.A. and Esterle, J.S., 2011. Adsorption and mineral trapping dominate CO2 storage in coal systems. *Energy Procedia*, *4*, pp. 3131-3138.

Gray, I., 1987. Reservoir engineering in coal seams: Part 1-The physical process of gas storage and movement in coal seams. *SPE Reservoir Engineering 2*, pp. 28-34.

Green, M.S., Flanegan, K.C. and Gilcrease, P.C., 2008. Characterization of a methanogenic consortium enriched from a coalbed methane well in the Powder River Basin, USA. *International Journal of Coal Geology*, *76*(1), pp. 34-45.

Gu, S., Gao, B., Teng, L., Li, Y., Fan, C., Iglauer, S., Zhang, D. and Ye, X., 2017. Monte Carlo simulation of supercritical carbon dioxide adsorption in carbon slit pores. *Energy & Fuels*.

Hamawand, I., Yusaf, T. and Hamawand, S.G., 2013. Coal seam gas and associated water: a review paper. *Renewable and Sustainable Energy Reviews 22*, pp. 550-560.

Hamilton, S.K., Golding, S.D., Baublys, K.A. and Esterle, J.S., 2015. Conceptual exploration targeting for microbially enhanced coal bed methane (MECoM) in the Walloon Subgroup, eastern Surat Basin, Australia. *International Journal of Coal Geology 138*, 68-82.

Harpalani, S., Chen, G., 1992. Effect of gas production on porosity and permeability of coal, Proceedings of the Symposium of Coalbed Methane R and D in Australia, pp. 67-73.

Harpalani, S., Chen, G., 1997. Influence of gas production induced volumetric strain on permeability of coal. *Geotechnical & Geological Engineering 15*, pp. 303-325.

Hashemi, S., Momeni, A., Melkoumian, N., 2014. Investigation of borehole stability in poorly cemented granular formations by discrete element method. *Journal of Petroleum Science and Engineering 113*, pp. 23-35.

Holditch, S., Ely, J., Semmelbeck, M., Carter, R., Hinkel, J. and Jeffrey Jr, R., 1988. Enhanced recovery of coalbed methane through hydraulic fracturing. in SPE Annual Technical Conference and Exhibition: Society of Petroleum Engineers.

Huggins, F., Kosmack, D., Huffman, G., Lee, R., 1980. Coal mineralogies by SEM automatic image analysis. Scanning Electron Microsc.;(United States) 1980.

Iglauer, S., 2011. Dissolution trapping of carbon dioxide in reservoir formation brine–a carbon storage mechanism. In *Mass Transfer-Advanced Aspects*. InTech.

Iglauer, S., Paluszny, A., Pentland, C.H., Blunt, M.J., 2011. Residual CO2 imaged with X-ray micro-tomography. *Geophysical Research Letters 38*.

Iglauer, S., Fernø, M.A., Shearing, P. and Blunt, M.J., 2012. Comparison of residual oil cluster size distribution, morphology and saturation in oil-wet and water-wet sandstone. *Journal of colloid and interface science*, *375*(1), pp. 187-192.

Iglauer, S., Paluszny, A. and Blunt, M., 2013. Simultaneous oil recovery and residual gas storage: A pore-level analysis using in situ X-ray micro-tomography. *Fuel, 103*, pp. 905-914.

Iglauer, S., Al-Yaseri, A.Z., Rezaee, R. and Lebedev, M., 2015. CO_2 wettability of caprocks: Implications for structural storage capacity and containment security. *Geophysical Research Letters*, *42*(21), pp. 9279-9284.

Iglauer, S., Rahman, T., Sarmadivaleh, M., Al-Hinai, A., Fernø, M. A. and Lebedev, M., 2016. Influence of wettability on residual gas trapping and enhanced oil recovery in three-phase flow: a pore-scale analysis by use of microcomputed tomography. *SPE Journal, 21*(06), pp. 1,916-1,929.

Iglauer, S., 2017. CO_2–Water–Rock Wettability: Variability, Influencing Factors, and Implications for CO_2 Geostorage. *Accounts of Chemical Research*, *50*(5), pp.1134-1142.

Izadi, G., Wang, S., Elsworth, D., Liu, J., Wu Y., and Pone D., 2011. Permeability evolution of fluid-infiltrated coal containing discrete fractures, *International Journal of Coal Geology*, *85*(2), pp. 202-211

Jasinge, D., Ranjith, P., Choi, S.-K., 2011. Effects of effective stress changes on permeability of latrobe valley brown coal. *Fuel 90*, pp. 1292-1300.

Jiang, M., Fu, C., Cui, L., Shen, Z., Zhu, F., 2016. DEM simulations of methane hydrate exploitation by thermal recovery and depressurization methods. Computers and Geotechnics.

Jing, Y., Armstrong, R.T., Ramandi, H.L., Mostaghimi, P., 2016. Coal cleat reconstruction using micro-computed tomography imaging. *Fuel 181*, pp. 286-299.

Jing, Y., Armstrong, R. T. and Mostaghimi, P.. 2017. Digital coal: Generation of fractured cores with microscale features. *Fuel, 207*, pp. 93-101.

Jouzel, J., Masson-Delmotte, V., Cattani, O., Dreyfus, G., Falourd, S., Hoffmann, G., Minster, B., Nouet, J., Barnola, J.M., Chappellaz, J. and Fischer, H., 2007. Orbital and millennial Antarctic climate variability over the past 800,000 years. *Science*, *317*(5839), pp.793-796.

Karacan, C. Ö. and Okandan, E., 2000. Fracture/cleat analysis of coals from Zonguldak Basin (northwestern Turkey) relative to the potential of coalbed methane production. *International Journal of Coal Geology, 44*(2), pp. 109-125.

Karacan, C.Ö., Ruiz, F.A., Cotè, M. and Phipps, S., 2011. Coal mine methane: a review of capture and utilization practices with benefits to mining safety and to greenhouse gas reduction. *International Journal of Coal Geology 86*(2), pp. 121-156.

Karacan, C.Ö., 2003. Heterogeneous sorption and swelling in a confined and stressed coal during CO_2 injection. *Energy & Fuels 17*(6), 1595-1608.

Kaveh, S., Rudolph, J., Wolf, A., and Ashrafizadeh, N., 2011. Wettability determination by contact angle measurements: hvBb coal–water system with injection of synthetic flue gas and CO_2, *Journal of Colloid and Interface science,* 364(1), pp. 237-247.

King, R., 1987. Elastic analysis of some punch problems for a layered medium. *International Journal of Solids and Structures, 23*(12), pp. 1657-1664.

Krevor, S., Blunt, M.J., Benson, S.M., Pentland, C.H., Reynolds, C., Al-Menhali, A. and Niu, B., 2015. Capillary trapping for geologic carbon dioxide storage–From pore scale physics to field scale implications. *International Journal of Greenhouse Gas Control*, *40*, pp.221-237.

Krooss, B., Van Bergen, F., Gensterblum, Y., Siemons, N., Pagnier, H. and David, P., 2002. High-pressure methane and carbon dioxide adsorption on dry and moisture-equilibrated Pennsylvanian coals. *International Journal of Coal Geology, 51*(2), pp. 69-92.

Kumar, V., Curtis, M. E., Gupta, N., Sondergeld, C. H. and Rai, C. S., 2012. Estimation of elastic properties of organic matter in Woodford Shale through nanoindentation measurements. in *SPE Canadian Unconventional Resources Conference*: Society of Petroleum Engineers.

Kutchko, B.G., Goodman, A.L., Rosenbaum, E., Natesakhawat, S., Wagner, K., 2013. Characterization of coal before and after supercritical CO_2 exposure via feature relocation using field-emission scanning electron microscopy. *Fuel 107*, 777-786.

Larsen, J.W., 2004. The effects of dissolved CO_2 on coal structure and properties. *International Journal of Coal Geology 57*, 63-70.

Laubach, S.E., Marrett, R.A., Olson, J.E. and Scott, A.R., 1998. Characteristics and origins of coal cleat: a review. *International Journal of Coal Geology*, *35*(1), pp.175-207.

Lebedev, M., Wilson, M. E. and Mikhaltsevitch, V., 2014. An experimental study of solid matrix weakening in water‐saturated Savonnières limestone. *Geophysical Prospecting, 62*(6), pp. 1253-1265.

Lebedev, M., Zhang, Y., Mikhaltsevitch, V., Inglauer, S. and Rahman, T., 2017a. Residual trapping of supercritical CO2: direct pore-scale observation using a low cost pressure cell for micro computer tomography. *Energy Procedia*, *114*, pp.4967-4974.

Lebedev, M., Zhang, Y., Sarmadivaleh, M., Barifcani, A., Al-Khdheeawi, E. and Iglauer, S., 2017b. Carbon geosequestration in limestone: Pore-scale dissolution and geomechanical weakening. *International Journal of Greenhouse Gas Control*, *66*, pp.106-119.

Li, C., Dong, L., Xu, X., Hu, P., Tian, J., Zhang, Y. and Yang, L., 2017. Theoretical and experimental evaluation of effective stress-induced sorption capacity change and its influence on coal permeability. *Journal of Geophysics and Engineering, 14*(3), pp. 654.

Li, H., Lin, B., Yang, W., Zheng, C., Hong, Y., Gao, Y., Liu, T. and Wu, S., 2016. Experimental study on the petrophysical variation of different rank coals with microwave treatment. *International Journal of Coal Geology, 154*, pp. 82-91

Li, Q. and Liu, G., 2016. Risk Assessment of the Geological Storage of CO_2: A Review. In *Geologic Carbon Sequestration* (pp. 249-284). Springer International Publishing.

Li, W. and Sakhaee-Pour, A., 2016. Macroscale Young's Moduli of Shale Based on Nanoindentations. *Petrophysics, 57*(06), pp. 597-603.

Li, Y., Tang, D., Xu, H., Meng, Y., Li, J., 2014. Experimental research on coal permeability: The roles of effective stress and gas slippage. *Journal of Natural Gas Science and Engineering 21*, pp. 481-488.

Liang, Z., Ioannidis, M. and Chatzis, I., 2000. Geometric and topological analysis of three-dimensional porous media: pore space partitioning based on morphological skeletonization. *Journal of colloid and interface science, 221*(1), pp. 13-24.

Lior, N., 2008. Energy resources and use: the present situation and possible paths to the future. *Energy 33*(6), pp. 842-857.

Liu, H.-H., Rutqvist, J., 2010. A new coal-permeability model: internal swelling stress and fracture–matrix interaction. *Transport in Porous Media 82*, 157-171.

Liu, J., Chen, Z., Elsworth, D., Qu, H. and Chen, D., 2011. Interactions of multiple processes during CBM extraction: a critical review. *International Journal of Coal Geology, 87*(3), pp. 175-189.

Liu, K., Ostadhassan, M. and Bubach, B., 2016. Applications of nano-indentation methods to estimate nanoscale mechanical properties of shale reservoir rocks. *Journal of Natural Gas Science and Engineering, 35*, pp. 1310-1319.

Liu, K. and Ostadhassan, M., 2017. Microstructural and geomechanical analysis of Bakken shale at nanoscale. *Journal of Petroleum Science and Engineering, 153*, pp. 133-144.

Liu, P., Yuan, Z. and Li, K., 2016. An improved capillary pressure model using fractal geometry for coal rock. *Journal of Petroleum Science and Engineering, 145*, pp. 473-481.

Lüthi, D., Le Floch, M., Bereiter, B., Blunier, T., Barnola, J.M., Siegenthaler, U., Raynaud, D., Jouzel, J., Fischer, H., Kawamura, K. and Stocker, T.F., 2008. High-resolution carbon dioxide concentration record 650,000-800,000 years before present. *Nature*, *453*(7193), p.379.

Mangan, A. P. and Whitaker, R. T., 1999. Partitioning 3D surface meshes using watershed segmentation. *IEEE Transactions on Visualization and Computer Graphics, 5*(4), pp. 308-321.

Manjunath, G. and Nair, R. R., 2015 Implications of the 3D micro scale coal characteristics along with Raman stress mapping of the scratch tracks. *International Journal of Coal Geology, 141*, pp. 13-22.

Mathews, J. P., Campbell, Q. P., Xu, H. and Halleck, P., 2017. A review of the application of X-ray computed tomography to the study of coal. *Fuel, 209*, pp. 10-24.

Matter, J.M. and Kelemen, P.B., 2009. Permanent storage of carbon dioxide in geological reservoirs by mineral carbonation. *Nature Geoscience*, *2*(12), p.837.

Mathews, J. P., Pone, J. D. N., Mitchell, G. D. and Halleck, P., 2011. High-resolution X-ray computed tomography observations of the thermal drying of lump-sized subbituminous coal. *Fuel processing technology, 92*(1), pp. 58-64.

Mazumder, S., Karnik, A. A. and Wolf, K.-H. A., 2006. Swelling of coal in response to CO_2 sequestration for ECBM and its effect on fracture permeability. *SPE Journal, 11*(03), pp. 390-398.

Mazumder, S., Wolf, K.-H., Elewaut, K. and Ephraim, R., 2006. Application of X-ray computed tomography for analyzing cleat spacing and cleat aperture in coal samples. *International Journal of Coal Geology, 68*(3), pp. 205-222.

Mazumder, S. and Wolf, K.H., 2008. Differential swelling and permeability change of coal in response to CO_2 injection for ECBM. *International Journal of Coal Geology*, *74*(2), pp.123-138.

McCabe, P. J., 1984. *Depositional environments of coal and coal‐bearing strata,* Wiley Online Library.

McKee, C.R., Bumb, A.C., Koenig, R.A., 1987. Stress-dependent permeability and porosity of coal, International Coalbed Methane Symposium, University of Alabama, Tuscaloosa, Alabama, pp. 183-193.

Metz, B., Davidson, O., De Coninck, H., Loos, M. and Meyer, L., 2005. *IPCC special report on carbon dioxide capture and storage*. Intergovernmental Panel on Climate Change, Geneva (Switzerland). Working Group III.

Montemagno, C. D. and Pyrak-Nolte, L. J., 1995. Porosity of natural fracture networks. *Geophysical Research Letters, 22*(11), pp. 1397-1400.

Moore, T.A., 2012. Coalbed methane: a review. *International Journal of Coal Geology*, *101*, pp.36-81.

Mostaghimi, P., Armstrong, R. T., Gerami, A., Hu, Y., Jing, Y., Kamali, F., Liu, M., Liu, Z., Lu, X. and Ramandi, H. L., 2017. Cleat-scale characterisation of coal: an overview. *Journal of Natural Gas Science and Engineering, 39*, pp. 143-160.

Naylor, M., Wilkinson, M. and Haszeldine, R.S., 2011. Calculation of CO_2 column heights in depleted gas fields from known pre-production gas column heights. *Marine and Petroleum Geology*, *28*(5), pp.1083-1093.

Ozdemir, E. and Schroeder, K., 2009. Effect of moisture on adsorption isotherms and adsorption capacities of CO2 on coals. *Energy & Fuels*, *23*(5), pp.2821-2831.

Palmer, I., Mansoori, J., 1996. How permeability depends on stress and pore pressure in coalbeds: a new model, SPE Annual Technical Conference and Exhibition. Society of Petroleum Engineers.

Pan, Z. and Connell, L. D., 2007. A theoretical model for gas adsorption-induced coal swelling. *International Journal of Coal Geology, 69*(4), pp. 243-252.

Pant, L. M., Huang, H., Secanell, M., Larter, S. and Mitra, S. K., 2015. Multi scale characterization of coal structure for mass transport. *Fuel, 159*, pp. 315-323.

Pekot, L., Reeves, S., 2002. Modeling coal matrix shrinkage and differential swelling with CO_2 injection for enhanced coalbed methane recovery and carbon sequestration applications. Topical report, US Department of Energy.

Pekot, L. and Reeves, S., 2003. Modeling the effects of matrix shrinkage and differential swelling on coalbed methane recovery and carbon sequestration. in *Paper 0328, proc. 2003 International Coalbed Methane Symposium. University of Alabama*: Citeseer.

Peng, Y., Liu, J., Wei, M., Pan, Z. and Connell, L. D., 2014. Why coal permeability changes under free swellings: New insights. *International Journal of Coal Geology, 133*, pp. 35-46.

Pentland, C.H., El-Maghraby, R., Iglauer, S. and Blunt, M.J., 2011. Measurements of the capillary trapping of super-critical carbon dioxide in Berea sandstone. *Geophysical Research Letters*, *38*(6).

Pillalamarry, M., Harpalani, S. and Liu, S., 2011. Gas diffusion behavior of coal and its impact on production from coalbed methane reservoirs. *International Journal of Coal Geology 86*(4), pp. 342-348.

Pini, R., Krevor, S.C. and Benson, S.M., 2012. Capillary pressure and heterogeneity for the CO_2/water system in sandstone rocks at reservoir conditions. *Advances in Water Resources*, *38*, pp.48-59.

Potyondy, D.O. and Cundall, P.A., 2004. A bonded-particle model for rock. *International journal of rock mechanics and mining sciences, 41*(8), 1329-1364.

Predeanu, G., Popescu, L. G., Abagiu, T. A., Panaitescu, C., Valentim, B. and Guedes, A., 2016. Characterization of bottom ash of Pliocene lignite as ceramic composites raw material by petrographic, SEM/EDS and Raman microspectroscopical methods. *International Journal of Coal Geology,* 168, pp. 131-145.

Rahman, T., Lebedev, M., Barifcani, A., Iglauer, S., 2016. Residual trapping of supercritical CO_2 in oil-wet sandstone. *Journal of colloid and interface science 469*, 63-68.

Ramandi, H. L., Mostaghimi, P., Armstrong, R. T., Saadatfar, M. and Pinczewski, W. V., 2016. Porosity and permeability characterization of coal: a micro-computed tomography study. *International Journal of Coal Geology, 154*, pp. 57-68.

Ranathunga, A.S., Perera, M.S.A., Ranjith, P.G. and Wei, C.H., 2017. An experimental investigation of applicability of CO_2 enhanced coal bed methane recovery to low rank coal. *Fuel*, *189*, pp.391-399.

Reeves, S., Davis, D. and Oudinot, A., 2004. A technical and economic sensitivity study of enhanced coalbed methane recovery and carbon sequestration in coal. *DOE topical report*.

Reeves, R., 2004. The Coal-Seq project: Key results from field, laboratory and modeling studies, paper presented at Proceedings of the 7th International Conference on Greenhouse Gas Control Technologies (GHGT-7), Citeseer.

Reeves, S. R., 2001. Geological Sequestration of CO_2 in Deep, Unmineable Coalbeds: An Integrated Research and Commerical-Scale Field Demonstration Project. in SPE annual technical conference and exhibition: Society of Petroleum Engineers.

Reeves, S.R., 2004. The Coal-Seq project: Key results from field, laboratory and modeling studies, Proceedings of the 7th International Conference on Greenhouse Gas Control Technologies (GHGT-7). Citeseer, pp. 1399-1406.

Reucroft, P., and Patel H., 1986. Gas-induced swelling in coal, *Fuel,* 65(6), pp. 816-820.

Roerdink, J. B. and Meijster, A., 2000. The watershed transform: Definitions, algorithms and parallelization strategies. *Fundamenta informaticae, 41*(1, 2), pp. 187-228.

Saghafi, A., 2010. Potential for ECBM and CO_2 storage in mixed gas Australian coals. *International Journal of Coal Geology 82*(3), pp. 240-251.

Sarmadivaleh, M., 2012. Experimental and numerical study of interaction of a pre-existing natural interface and an induced hydraulic fracture. Curtin University.

Schlüter, S., Sheppard, A., Brown, K., Wildenschild, D., 2014. Image processing of multiphase images obtained via X-ray microtomography: a review. *Water Resources Research 50*, pp. 3615-3639.

Seidle, J., Jeansonne, M., Erickson, D., 1992. Application of matchstick geometry to stress dependent permeability in coals, SPE rocky mountain regional meeting. Society of Petroleum Engineers.

Sharma, H., Mazumder, S., Gilbert, T., Tovar, M. and Philpot, J. A., 2013. Novel Approach to EUR estimation in Coal Seam Gas Wells. in SPE Unconventional Resources Conference and Exhibition-Asia Pacific: Society of Petroleum Engineers.

Sheorey, P., 1994. A theory for in situ stresses in isotropic and transverseley isotropic rock, International journal of rock mechanics and mining sciences & geomechanics abstracts. Elsevier, 23-34.

Shi, J., and Durucan, S., 2005a. A model for changes in coalbed permeability during primary and enhanced methane recovery, SPE Reservoir Evaluation & Engineering, 8(04), pp. 291-299.

Shi, J., and Durucan, S., 2005b. CO_2 storage in deep unminable coal seams. *Oil & gas science and technology, 60*(3), pp. 547-558.

Shi, X., Pan, J., Hou, Q., Jin, Y., Wang, Z., Niu, Q. and Li, M., 2018. Micrometer-scale fractures in coal related to coal rank based on micro-CT scanning and fractal theory. *Fuel*, *212*, pp.162-172.

Siriwardane, H., Haljasmaa, I., McLendon, R., Irdi, G., Soong, Y., Bromhal, G., 2009. Influence of carbon dioxide on coal permeability determined by pressure transient methods. *International Journal of Coal Geology 77*, pp.109-118.

Solano-Acosta, W., Mastalerz, M. and Schimmelmann, A. (2007) Cleats and their relation to geologic lineaments and coalbed methane potential in Pennsylvanian coals in Indiana. *International Journal of Coal Geology, 72*(3), pp. 187-208.

Somerton, W.H., Söylemezoḡlu, I., Dudley, R., 1975. Effect of stress on permeability of coal, *International journal of rock mechanics and mining sciences & geomechanics abstracts*. Elsevier, pp. 129-145.

Stauffer, D., Scaling theory of percolation clusters, *Physics reports, 54*, 1-74, 1979.

Stevens, S.H., Spector, D., Riemer, P., Enhanced coalbed methane recovery using CO_2 injection: worldwide resource and CO_2 sequestration potential, in: SPE International Oil and Gas Conference and Exhibition in China, Society of Petroleum Engineers, 1998.

Strąpoć, D., Picardal, F.W., Turich, C., Schaperdoth, I., Macalady, J.L., Lipp, J.S., Lin, Y.S., Ertefai, T.F., Schubotz, F., Hinrichs, K.U. and Mastalerz, M., 2008. Methane-producing microbial community in a coal bed of the Illinois Basin. *Applied and environmental microbiology*, *74*(8), pp. 2424-2432.

Syed, A., Durucan, S., Shi, J., and Korre, A., 2013. Flue Gas Injection for CO_2 Storage and Enhanced Coalbed Methane Recovery: Mixed Gas Sorption and Swelling Characteristics of Coals, *Energy Procedia, 37*, pp. 6738-6745

Su, X., Feng, Y., Chen, J. and Pan, J., 2001. The characteristics and origins of cleat in coal from Western North China. *International Journal of Coal Geology, 47*(1), pp. 51-62.

Sun, X., Yao, Y., Liu, D., Elsworth, D. and Pan, Z., 2016. Interactions and exchange of CO_2 and H_2O in coals: an investigation by low-field NMR relaxation. *Scientific reports, 6*.

Syed, A., Durucan, S., Shi, J.-Q. and Korre, A., 2013. Flue Gas Injection for CO_2 Storage and Enhanced Coalbed Methane Recovery: Mixed Gas Sorption and Swelling Characteristics of Coals. *Energy Procedia, 37*, pp. 6738-6745.

Tajduś, K., 2009. New method for determining the elastic parameters of rock mass layers in the region of underground mining influence. *International Journal of Rock Mechanics and Mining Sciences 46*, pp. 1296-1305.

Tu, Q., Cheng, Y., Guo, P., Jiang, J., Wang, L. and Zhang, R., 2016. Experimental study of coal and gas outbursts related to gas-enriched areas. *Rock Mechanics and Rock Engineering 49*(9), pp.3769-3781.

Vandamme, M., Brochard, L., Lecampion, B. and Coussy, O., 2010. Adsorption and strain: the CO_2-induced swelling of coal. *Journal of the Mechanics and Physics of Solids, 58*(10), pp. 1489-1505.

Vargaftik, N.B., 1975. Handbook of physical properties of liquids and gases-pure substances and mixtures.

Vassilev, S. V., Kitano, K. and Vassileva, C. G., 1996. Some relationships between coal rank and chemical and mineral composition. *Fuel, 75*(13), pp. 1537-1542.

Vialle, S. and Lebedev, M., 2015. Heterogeneities in the elastic properties of microporous carbonate rocks at the microscale from nanoindentation tests. in *SEG Technical Program Expanded Abstracts 2015*: Society of Exploration Geophysicists. pp. 3279-3284.

Vishal, V., Singh, T.N. and Ranjith, P.G., 2015. Influence of sorption time in CO_2-ECBM process in Indian coals using coupled numerical simulation. *Fuel 139*, 51-58.

Walker, P. L., Verma, S. K., Rivera-Utrilla, J. and Davis, A., 1988. Densities, porosities and surface areas of coal macerals as measured by their interaction with gases, vapours and liquids. *Fuel, 67*(12), pp. 1615-1623.

Wang, G., Ren, T., Wang, K., Zhou, A., 2014. Improved apparent permeability models of gas flow in coal with Klinkenberg effect. *Fuel 128*, 53-61.

Wang, S., Elsworth D., and Liu J., 2011. Permeability evolution in fractured coal: the roles of fracture geometry and water-content, *International Journal of Coal Geology, 87*(1), pp.13-25.

Wang, T., Zhou, W., Chen, J., Xiao, X., Li, Y., Zhao, X., 2014. Simulation of hydraulic fracturing using particle flow method and application in a coal mine. *International Journal of Coal Geology 121*, 1-13.

White, C.M., Smith, D.H., Jones, K.L., Goodman, A.L., Jikich, S.A., LaCount, R.B., DuBose, S.B., Ozdemir, E., Morsi, B.I. and Schroeder, K.T., 2005. Sequestration of carbon dioxide in coal with enhanced coalbed methane recovery a review. *Energy & Fuels, 19*(3), pp.659-724.

Whiticar, M.J., Faber, E. and Schoell, M., 1986. Biogenic methane formation in marine and freshwater environments: CO2 reduction vs. acetate fermentation—isotope evidence. *Geochimica et Cosmochimica Acta*, *50*(5), pp.693-709.

Wildenschild, D. and Sheppard, A. P., 2013. X-ray imaging and analysis techniques for quantifying pore-scale structure and processes in subsurface porous medium systems. *Advances in Water Resources, 51*, pp. 217-246.

Wu, Y., Liu J., Elsworth D., Siriwardane H., and Miao X., 2011. Evolution of coal permeability: Contribution of heterogeneous swelling processes, *International Journal of Coal Geology,* 88(2), pp. 152-162.

Xu, T., Apps, J.A. and Pruess, K., 2003. Reactive geochemical transport simulation to study mineral trapping for CO2 disposal in deep arenaceous formations. *Journal of Geophysical Research: Solid Earth*, *108*(B2).

Xu, X., Sarmadivaleh, M., Li, C., Xie, B. and Iglauer, S., 2016. Experimental study on physical structure properties and anisotropic cleat permeability estimation on coal cores from China. *Journal of Natural Gas Science and Engineering, 35*, pp. 131-143

Yao, Y., Liu, D., Che, Y., Tang, D., Tang, S. and Huang, W., 2009. Non-destructive characterization of coal samples from China using microfocus X-ray computed tomography. *International Journal of Coal Geology, 80*(2), pp. 113-123.

Yao, Y., Liu, D. and Xie, S., 2014. Quantitative characterization of methane adsorption on coal using a low-field NMR relaxation method. *International Journal of Coal Geology, 131*, pp. 32-40.

Ye, R., Xiang, C., Lin, J., Peng, Z., Huang, K., Yan, Z., Cook, N.P., Samuel, E.L., Hwang, C.-C., Ruan, G., 2013. Coal as an abundant source of graphene quantum dots. *Nature communications 4*.

Yu, Y., Liang, W., Hu, Y. and Meng, Q., 2012. Study of micro-pores development in lean coal with temperature. *International Journal of Rock Mechanics and Mining Sciences, 51*, pp. 91-96.

Yu, H., Zhang, Y., Lebedev, M., Han, T., Verrall, M., Wang, Z., Al-Khdheeawi, E., Al-Yaseri, A. and Iglauer, S., 2017. Nanoscale geomechanical properties of Western Australian coal. *Journal of Petroleum Science and Engineering*. https://doi.org/10.1016/j.petrol.2017.11.001

Zeszotarski, J. C., Chromik, R. R., Vinci, R. P., Messmer, M. C., Michels, R. and Larsen, J. W., 2004. Imaging and mechanical property measurements of kerogen via nanoindentation. *Geochimica et cosmochimica acta, 68*(20), pp. 4113-4119.

Zhai, C., Xiang, X., Xu, J. and Wu, S., 2016. The characteristics and main influencing factors affecting coal and gas outbursts in Chinese Pingdingshan mining region. *Natural Hazards, 82*(1), pp. 507-530.

Zhang, E., Hill, R.J., Katz, B.J. and Tang, Y., 2008. Modeling of gas generation from the Cameo coal zone in the Piceance Basin, Colorado. *AAPG bulletin*, *92*(8), pp.1077-1106.

Zhang, D., Li S., Cui Y., Song W., and Lin W., 2011. Displacement behavior of methane adsorbed on coal by CO2 injection, *Industrial & Engineering Chemistry Research,* 50(14), pp. 8742-8749.

Zhang, Y., Lebedev, M., Sarmadivaleh, M., Barifcani, A. and Iglauer, S., 2016a. Change in Geomechanical Properties of Limestone Due to Supercritical CO_2 Injection. in *SPE Asia Pacific Oil & Gas Conference and Exhibition*: Society of Petroleum Engineers.

Zhang, Y., Lebedev, M., Sarmadivaleh, M., Barifcani, A. and Iglauer, S., 2016b. Swelling‐induced changes in coal microstructure due to supercritical CO2 injection. *Geophysical Research Letters, 43*(17), pp. 9077-9083.

Zhang, Y., Lebedev, M., Sarmadivaleh, M., Barifcani, A., Rahman, T. and Iglauer, S., 2016c. Swelling effect on coal micro structure and associated permeability reduction. *Fuel, 182*, pp. 568-576.

Zhang, Y., Sarmadivaleh, M., Barifcani, A., Lebedev, M. and Iglauer, S., 2016d. Coal microstructure changes due to water absorption and CO_2 injection. *The APPEA Journal, 56*(2), pp. 593-593.

Zhang, Y., Xu, X., Lebedev, M., Sarmadivaleh, M., Barifcani, A. and Iglauer, S., 2016e. Multi-scale x-ray computed tomography analysis of coal microstructure and permeability changes as a function of effective stress. *International Journal of Coal Geology, 165*, pp. 149-156.

Zhang, Y., Sarmadivaleh, M., Lebedev, M., Barifcani, A., Rezaee, R., Testamantia, N. and Iglauer, S., 2016f, March. Geo-Mechanical Weakening of Limestone Due to Supercritical CO_2 Injection. In Offshore Technology Conference Asia. Offshore Technology Conference.

Zhang, Y., Zhang, Z., Sarmadivaleh, M., Lebedev, M., Barifcani, A., Yu, H. and Iglauer, S., 2017. Micro-scale fracturing mechanisms in coal induced by adsorption of supercritical CO 2. *International Journal of Coal Geology, 175*, pp. 40-50.

Zhang, Z., Zhang, G., Li, S., Li, R., Dong, H., Ding, X., 2016g. Modified relationship between point loading strength and uniaxial compressive strength by DEM, 50th US Rock Mechanics/Geomechanics Symposium. American Rock Mechanics Association.

Zhao, J., Xu, H., Tang, D., Mathews, J. P., Li, S. and Tao, S., 2016. Coal seam porosity and fracture heterogeneity of macrolithotypes in the Hancheng Block, eastern margin, Ordos Basin, China. *International Journal of Coal Geology, 159*, pp. 18-29.

Zhou, S., Liu, D., Cai, Y., Yao, Y. and Li, Z., 2017. 3D characterization and quantitative evaluation of pore-fracture networks of two Chinese coals using FIB-SEM tomography. *International Journal of Coal Geology, 174*, pp. 41-54.

Zhou, S., Zhu, H., Yan, Z., Ju, J.W., Zhang, L., 2016. A micromechanical study of the breakage mechanism of microcapsules in concrete using PFC2D. *Construction and Building Materials 115*, pp. 452-463.

Zhu, W., Fonteyn, M., Hughes, J. and Pearce, C., 2009. Nanoindentation study of resin impregnated sandstone and early-age cement paste specimens. *Nanotechnology in Construction 3*, pp. 403-408.
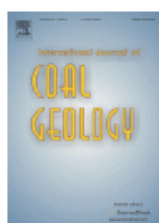
Appendix

Order Completed

Thank you for your order.

This Agreement between Yihuai Zhang ("You") and Elsevier ("Elsevier") consists of your license details and the terms and conditions provided by Elsevier and Copyright Clearance Center.

Your confirmation email will contain your order number for future reference.

Printable details.

License Number	4179440925003
License date	Aug 31, 2017
Licensed Content Publisher	Elsevier
Licensed Content Publication	International Journal of Coal Geology
Licensed Content Title	Coalbed methane: A review
Licensed Content Author	Tim A. Moore
Licensed Content Date	Nov 1, 2012
Licensed Content Volume	101
Licensed Content Issue	n/a
Licensed Content Pages	46
Type of Use	reuse in a thesis/dissertation
Portion	figures/tables/illustrations
Number of figures/tables/illustrations	2
Format	both print and electronic
Are you the author of this Elsevier article?	No
Will you be translating?	No
Original figure numbers	Fig.10, Fig.12
Title of your thesis/dissertation	Microstructure and nanoscale rock mechanical properties of coal: applications to CO2 storage
Expected completion date	Sep 2017
Estimated size (number of pages)	100
Requestor Location	Yihuai Zhang 19 Kardan cct
	Karawara, 6157 Australia Attn: Yihuai Zhang
Total	0.00 USD

144

Order Completed

Thank you for your order.

This Agreement between Yihuai Zhang ("You") and Elsevier ("Elsevier") consists of your license details and the terms and conditions provided by Elsevier and Copyright Clearance Center.

Your confirmation email will contain your order number for future reference.

Printable details.

License Number	4179440200418
License date	Aug 31, 2017
Licensed Content Publisher	Elsevier
Licensed Content Publication	Fuel
Licensed Content Title	An experimental investigation of applicability of CO2 enhanced coal bed methane recovery to low rank coal
Licensed Content Author	A.S. Ranathunga, M.S.A. Perera, P.G. Ranjith, C.H. Wei
Licensed Content Date	Feb 1, 2017
Licensed Content Volume	189
Licensed Content Issue	n/a
Licensed Content Pages	9
Type of Use	reuse in a thesis/dissertation
Portion	figures/tables/illustrations
Number of figures/tables/illustrations	1
Format	both print and electronic
Are you the author of this Elsevier article?	No
Will you be translating?	No
Original figure numbers	Fig.6
Title of your thesis/dissertation	Microstructure and nanoscale rock mechanical properties of coal: applications to CO2 storage
Expected completion date	Sep 2017
Estimated size (number of pages)	100
Requestor Location	Yihuai Zhang 19 Kardan cct
	Karawara, 6157 Australia Attn: Yihuai Zhang
Total	0.00 USD

Title:	Comparison of residual oil cluster size distribution, morphology and saturation in oil-wet and water-wet sandstone
Author:	S. Iglauer, M.A. Fernø, P. Shearing, M.J. Blunt
Publication:	Journal of Colloid and Interface Science
Publisher:	Elsevier
Date:	1 June 2012
	Copyright © 2012 Elsevier Inc.

Order Completed

Thank you for your order.

This Agreement between Yihuai Zhang ("You") and Elsevier ("Elsevier") consists of your license details and the terms and conditions provided by Elsevier and Copyright Clearance Center.

Your confirmation email will contain your order number for future reference.

Printable details.

License Number	4179440025034
License date	Aug 31, 2017
Licensed Content Publisher	Elsevier
Licensed Content Publication	Journal of Colloid and Interface Science
Licensed Content Title	Comparison of residual oil cluster size distribution, morphology and saturation in oil-wet and water-wet sandstone
Licensed Content Author	S. Iglauer, M.A. Fernø, P. Shearing, M.J. Blunt
Licensed Content Date	Jun 1, 2012
Licensed Content Volume	375
Licensed Content Issue	1
Licensed Content Pages	6
Type of Use	reuse in a thesis/dissertation
Portion	figures/tables/illustrations
Number of figures/tables/illustrations	1
Format	both print and electronic
Are you the author of this Elsevier article?	No
Will you be translating?	No
Original figure numbers	Fig.2
Title of your thesis/dissertation	Microstructure and nanoscale rock mechanical properties of coal: applications to CO2 storage
Expected completion date	Sep 2017
Estimated size (number of pages)	100
Requestor Location	Yihuai Zhang 19 Kardan cct

WILEY

Title:	Residual CO2 imaged with X-ray micro-tomography
Author:	Stefan Iglauer,Adriana Paluszny,Christopher H. Pentland,Martin J. Blunt
Publication:	Geophysical Research Letters
Publisher:	John Wiley and Sons
Date:	Nov 10, 2011
	Copyright 2011 by the American Geophysical Union.

Order Completed

Thank you for your order.

This Agreement between Yihuai Zhang ("You") and John Wiley and Sons ("John Wiley and Sons") consists of your license details and the terms and conditions provided by John Wiley and Sons and Copyright Clearance Center.

Your confirmation email will contain your order number for future reference.

Printable details.

License Number	4179431364010
License date	Aug 31, 2017
Licensed Content Publisher	John Wiley and Sons
Licensed Content Publication	Geophysical Research Letters
Licensed Content Title	Residual CO2 imaged with X-ray micro-tomography
Licensed Content Author	Stefan Iglauer,Adriana Paluszny,Christopher H. Pentland,Martin J. Blunt
Licensed Content Date	Nov 10, 2011
Licensed Content Pages	1
Type of use	Dissertation/Thesis
Requestor type	University/Academic
Format	Print and electronic
Portion	Figure/table
Number of figures/tables	1
Original Wiley figure/table number(s)	Figure 1
Will you be translating?	No
Title of your thesis / dissertation	Microstructure and nanoscale rock mechanical properties of coal: applications to CO2 storage
Expected completion date	Sep 2017
Expected size (number of pages)	100
Requestor Location	Yihuai Zhang 19 Kardan cct

Title: An experimental study of solid matrix weakening in water-saturated Savonnières limestone

Author: Maxim Lebedev, Moyra E.J. Wilson, Vassily Mikhaltsevitch

Publication: Geophysical Prospecting

Publisher: John Wiley and Sons

Date: Sep 16, 2014

© 2014 European Association of Geoscientists & Engineers

Logged in as:
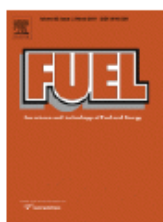Yihuai Zhang
Account #:
3001048947

LOGOUT

Order Completed

Thank you for your order.

This Agreement between Yihuai Zhang ("You") and John Wiley and Sons ("John Wiley and Sons") consists of your license details and the terms and conditions provided by John Wiley and Sons and Copyright Clearance Center.

Your confirmation email will contain your order number for future reference.

Printable details.

License Number	4179431042492
License date	Aug 31, 2017
Licensed Content Publisher	John Wiley and Sons
Licensed Content Publication	Geophysical Prospecting
Licensed Content Title	An experimental study of solid matrix weakening in water-saturated Savonnières limestone
Licensed Content Author	Maxim Lebedev, Moyra E.J. Wilson, Vassily Mikhaltsevitch
Licensed Content Date	Sep 16, 2014
Licensed Content Pages	13
Type of use	Dissertation/Thesis
Requestor type	University/Academic
Format	Print and electronic
Portion	Figure/table
Number of figures/tables	1
Original Wiley figure/table number(s)	Figure 2
Will you be translating?	No
Title of your thesis / dissertation	Microstructure and nanoscale rock mechanical properties of coal: applications to CO2 storage
Expected completion date	Sep 2017
Expected size (number of pages)	100
Requestor Location	Yihuai Zhang 19 Kardan cct

148

Title: Swelling effect on coal micro structure and associated permeability reduction

Author: Yihuai Zhang,Maxim Lebedev,Mohammad Sarmadivaleh,Ahmed Barifcani,Taufiq Rahman,Stefan Iglauer

Publication: Fuel

Publisher: Elsevier

Date: 15 October 2016

Order Completed

Thank you for your order.

This Agreement between Yihuai Zhang ("You") and Elsevier ("Elsevier") consists of your license details and the terms and conditions provided by Elsevier and Copyright Clearance Center.

Your confirmation email will contain your order number for future reference.

Printable details.

License Number	4157121452218
License date	Jul 27, 2017
Licensed Content Publisher	Elsevier
Licensed Content Publication	Fuel
Licensed Content Title	Swelling effect on coal micro structure and associated permeability reduction
Licensed Content Author	Yihuai Zhang,Maxim Lebedev,Mohammad Sarmadivaleh,Ahmed Barifcani,Taufiq Rahman,Stefan Iglauer
Licensed Content Date	Oct 15, 2016
Licensed Content Volume	182
Licensed Content Issue	n/a
Licensed Content Pages	9
Type of Use	reuse in a thesis/dissertation
Portion	full article
Format	both print and electronic
Are you the author of this Elsevier article?	Yes
Will you be translating?	No
Title of your thesis/dissertation	Microstructure and nanoscale rock mechanical properties of coal: applications to CO2 storage
Expected completion date	Sep 2017
Estimated size (number of pages)	100
Requestor Location	Yihuai Zhang 19 Kardan cct
	Karawara, 6157 Australia Attn: Yihuai Zhang
Total	0.00 USD

WILEY

Title:	Swelling-induced changes in coal microstructure due to supercritical CO2 injection
Author:	Yihuai Zhang,Maxim Lebedev,Mohammad Sarmadivaleh,Ahmed Barifcani,Stefan Iglauer
Publication:	Geophysical Research Letters
Publisher:	John Wiley and Sons
Date:	Sep 14, 2016

©2016. American Geophysical Union. All Rights Reserved.
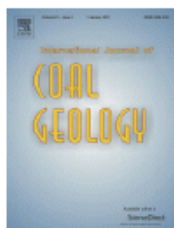
Order Completed

Thank you for your order.

This Agreement between Yihuai Zhang ("You") and John Wiley and Sons ("John Wiley and Sons") consists of your license details and the terms and conditions provided by John Wiley and Sons and Copyright Clearance Center.

Your confirmation email will contain your order number for future reference.

Printable details.

License Number	4175470160533
License date	Aug 24, 2017
Licensed Content Publisher	John Wiley and Sons
Licensed Content Publication	Geophysical Research Letters
Licensed Content Title	Swelling-induced changes in coal microstructure due to supercritical CO2 injection
Licensed Content Author	Yihuai Zhang,Maxim Lebedev,Mohammad Sarmadivaleh,Ahmed Barifcani,Stefan Iglauer
Licensed Content Date	Sep 14, 2016
Licensed Content Pages	7
Type of use	Dissertation/Thesis
Requestor type	Author of this Wiley article
Format	Print and electronic
Portion	Full article
Will you be translating?	No
Title of your thesis / dissertation	Microstructure and nanoscale rock mechanical properties of coal: applications to CO2 storage
Expected completion date	Sep 2017
Expected size (number of pages)	100
Requestor Location	Yihuai Zhang 19 Kardan cct

Title: Multi–scale x–ray computed tomography analysis of coal microstructure and permeability changes as a function of effective stress

Author: Yihuai Zhang,Xiaomeng Xu,Maxim Lebedev,Mohammad Sarmadivaleh,Ahmed Barifcani,Stefan Iglauer

Publication: International Journal of Coal Geology

Publisher: Elsevier

Date: 1 August 2016

© 2016 Elsevier B.V. All rights reserved.

Order Completed

Thank you for your order,

This Agreement between Yihuai Zhang ("You") and Elsevier ("Elsevier") consists of your license details and the terms and conditions provided by Elsevier and Copyright Clearance Center.

Your confirmation email will contain your order number for future reference,

Printable details.

License Number	4175461376479
License date	Aug 24, 2017
Licensed Content Publisher	Elsevier
Licensed Content Publication	International Journal of Coal Geology
Licensed Content Title	Multi–scale x-ray computed tomography analysis of coal microstructure and permeability changes as a function of effective stress
Licensed Content Author	Yihuai Zhang,Xiaomeng Xu,Maxim Lebedev,Mohammad Sarmadivaleh,Ahmed Barifcani,Stefan Iglauer
Licensed Content Date	Aug 1, 2016
Licensed Content Volume	165
Licensed Content Issue	n/a
Licensed Content Pages	8
Type of Use	reuse in a thesis/dissertation
Portion	full article
Format	both print and electronic
Are you the author of this Elsevier article?	Yes
Will you be translating?	No
Title of your thesis/dissertation	Microstructure and nanoscale rock mechanical properties of coal: applications to CO2 storage
Expected completion date	Sep 2017
Estimated size (number of pages)	100

Title: Micro-scale fracturing mechanisms in coal induced by adsorption of supercritical CO2

Author: Yihuai Zhang,Zike Zhang,Mohammad Sarmadivaleh,Maxim Lebedev,Ahmed Barifcani,Hongyan Yu,Stefan Iglauer

Publication: International Journal of Coal Geology

Publisher: Elsevier

Date: 15 April 2017

© 2017 Elsevier B.V. All rights reserved.

Order Completed

Thank you for your order.

This Agreement between Yihuai Zhang ("You") and Elsevier ("Elsevier") consists of your license details and the terms and conditions provided by Elsevier and Copyright Clearance Center.

Your confirmation email will contain your order number for future reference.

Printable details.

License Number	4175461190231
License date	Aug 24, 2017
Licensed Content Publisher	Elsevier
Licensed Content Publication	International Journal of Coal Geology
Licensed Content Title	Micro-scale fracturing mechanisms in coal induced by adsorption of supercritical CO2
Licensed Content Author	Yihuai Zhang,Zike Zhang,Mohammad Sarmadivaleh,Maxim Lebedev,Ahmed Barifcani,Hongyan Yu,Stefan Iglauer
Licensed Content Date	Apr 15, 2017
Licensed Content Volume	175
Licensed Content Issue	n/a
Licensed Content Pages	11
Type of Use	reuse in a thesis/dissertation
Portion	full article
Format	both print and electronic
Are you the author of this Elsevier article?	Yes
Will you be translating?	No
Title of your thesis/dissertation	Microstructure and nanoscale rock mechanical properties of coal: applications to CO2 storage
Expected completion date	Sep 2017
Estimated size (number of pages)	100
Requestor Location	Yihuai Zhang

152